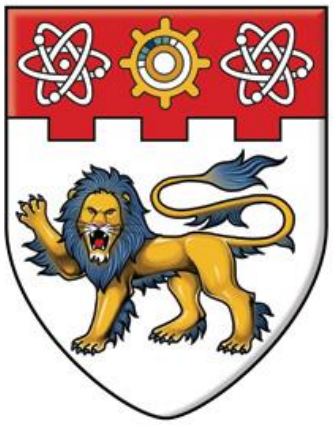

NANYANG TECHNOLOGICAL UNIVERSITY

OPTIMIZATION OF 3D PRINTABLE CELLULAR ARRAY STRUCTURES FOR CUSHIONING

SHUKRI BIN ABDUL JALIL

SINGAPORE CENTRE FOR 3D PRINTING

SCHOOL OF MECHANICAL AND AEROSPACE ENGINEERING

2018

OPTIMIZATION OF 3D PRINTABLE CELLULAR ARRAY STRUCTURES FOR CUSHIONING

SHUKRI BIN ABDUL JALIL

(G1401040J)

School of Mechanical and Aerospace Engineering

A thesis submitted to the Nanyang Technological University

in fulfilment of the requirement for the degree of

Doctor of Philosophy

2018

Statement of Originality

I hereby certify that the work embodied in this thesis is the result of original research, is free of plagiarised materials, and has not been submitted for a higher degree to any other University or Institution.

9 May 2019

. . . . . .

Date

. . . . . .

Shukri Bin Abdul Jalil

Supervisor Declaration Statement

I have reviewed the content and presentation style of this thesis and declare it is free of plagiarism and of sufficient grammatical clarity to be examined. To the best of my knowledge, the research and writing are those of the candidate except as acknowledged in the Author Attribution Statement. I confirm that the investigations were conducted in accord with the ethics policies and integrity standards of Nanyang Technological University and that the research data are presented honestly and without prejudice.

9 May 2019

. . . . . .

Date

. . . . . .

A/P Chou Siaw Meng

Authorship Attribution Statement

This thesis contains material from 1 paper accepted at conferences in which I am listed as an author.

Chapter 3.2.1 is published as S. Abdul Jalil, S.M. Chou, K. Tai, *Controlling Polymer Digital Material Composition With Layering*, International Conference on Progress in Additive Manufacturing, Pro-AM 2016, Singapore, 16 – 19 May 2016.

The contributions of the co-authors are as follows:

- I prepared the manuscript drafts. The manuscript was revised by A/Prof Chou and A/Prof Tai.
- I co-designed the study with A/Prof Chou and A/Prof Tai and performed all the laboratory work at the Singapore Centre for 3D Printing Future of Manufacturing Lab 1 and Mechanics of Machines and Materials Lab. I also analyzed the data.

9 May 2019

. . . . . .

Date

. . . . . .

Shukri Bin Abdul Jalil

ACKNOWLEDGEMENT

The author is truly thankful for the guidance from his supervisors, Associate Professor Chou Siaw Meng and Associate Professor Tai Kang. Their invaluable advice and patience throughout his candidature were truly appreciated. The author would also like to extend his appreciation to Professor Chua Chee Kai for opening the opportunity in pursuing his research in Singapore Centre for 3D Printing (SC3DP).

Secondly, the author would like to thank the undergraduate and master students he mentored for their Final Year Projects (FYP), Undergraduate Research Experience on Campus (URECA) and master's dissertation projects for their help in the experiments and analyses providing valuable information to the author.

The author is also grateful to fellow researcher in SC3DP, Ahmad Anwar for his companionship and support throughout the entire journey. The author also would like to thank other researchers who have helped along the way.

This research would not have been possible without the help of the laboratory technicians from the School of Mechanical and Aerospace Engineering, Nanyang Technological University.

Lastly, but definitely not the least, the author would like to thank his family and friends for their motivating words and actions. The author would also like to give thanks and praise God the Almighty for blessing his entire candidature journey.

ABSTRACT

Cushions are energy absorbing structures or materials used in various applications including packaging, footwear and protective gears. They often come in the form of polymeric cellular structures such as foams. The cushion selection process conventionally involves testing of available foams and selecting the foam which is best suited for the target application.

Optimized cushions would greatly improve the selection process and its effectiveness for a targeted task. Instead of selecting a cellular solid best suited for a particular application, the foam or the cellular structure itself is designed and optimized based on the requirements of the application. This requires understanding and control of the cellular structure's design parameters and additive manufacturing (AM) or three-dimensional (3D) printing offers great design freedom for the fabrication of complex porous parts.

Polyjet printing is a 3D printing process that is capable of producing complex polymer parts for various purposes (prototypes to functional parts). Polyjet printing is also capable of producing digital polymers which are polymers composing of up to three different polymer resins hence offering a range of physical and mechanical properties.

This research aims to develop an optimized 3D printed cellular structure for cushioning purposes. The effect of cellular microstructure and density on the cushioning properties of the final structure will first be investigated. This is followed by the formulation of an optimization problem to optimize the design parameters of a cellular structure for cushioning purposes.

To achieve the above, methods of evaluating cushioning properties were reviewed and a new cellular structure model was designed with the unit cells arranged in a regular

array. The design allows the tuning of the structure's stiffness and strength without affecting its weight i.e. maintaining its relative density. Theoretically, this new method of designing cellular structures allows for an exponential increase in stiffness by decreasing the cellular size. A mathematical model was then developed to accurately predict ($R^2 > 0.6$) the mechanical response of the honeycomb during compressive deformation.

A method which predicts the dynamic response of cellular structures using its static compressive data and the mathematical model were used to optimize the structure to meet various cushioning requirement. The optimized cushions were compared to conventional cushions for various applications. The optimized cushions are always lighter (50% ~ 90%) when compared to conventional cushions with similar thickness.

TABLE OF CONTENTS

LIST OF FIGURES

LIST OF TABLES

LIST OF SYMBOLS

$\mathbf{K_R}$	Adjustment factor for pre-buckling strain
$\mathbf{I_{m.i}}$	Area moment of inertia
$\boldsymbol{\sigma_p}$	Average plateau stress
R	Cell slenderness
$\mathbf{E^*}$	Cellular structure's modulus
l	Cell wall length (angled)
$\mathbf{l_2}$	Cell wall length for **n** = 2
$\mathbf{l_v}$	Cell wall length (vertical)
t	Cell wall thickness
K	Column effective length factor
A	Contact area
$\boldsymbol{\sigma_{cr}}$	Critical buckling stress
C	Cushioning capacity
$\boldsymbol{\varepsilon_d}$	Densification strain

ρ	Density
L_z	Depth of cushioning structure
G	Dimensionless acceleration or deceleration as a ratio of gravitational acceleration
H	Drop height
W_d	Energy absorbed by cellular structure up till ε_d
W_{pk}	Energy absorbed up till first peak stress
W	Energy absorption capacity
W_{eff}	Energy absorption efficiency
E_n	Average modulus from ε_0 to ε_n
P_{cr}	Euler's critical buckling load
σ_{pk}	First peak stress
g	Gravitational acceleration (9.81 m/s^2)
L_y	Height of foam/cellular structure
I	Ideality of a cushion
ΔE_n	Nominal difference in modulus when ε_n is assumed to be yield strain

$\mathbf{c}$	Number of structural units
$\boldsymbol{\varepsilon_p}$	Onset of plateau strain
$\boldsymbol{\sigma_y}$	Plastic yield strength
$\boldsymbol{\varepsilon_p'}$	Pre-buckling strain
$\boldsymbol{E_n'}$	Predicted modulus of LEPP model if yield strain is assumed at $\boldsymbol{\varepsilon_n}$
$\mathbf{n}$	Refinement factor
$\boldsymbol{\sigma_{static}}$	Static stress
$\mathbf{R^2}$	Statistical measure of closeness of curve fit
$\boldsymbol{\varepsilon}$	Strain
$\boldsymbol{\varepsilon_n}$	Strain at data point ‘n’
$\boldsymbol{\varepsilon_{pk}}$	Strain corresponding to first peak stress
$\boldsymbol{\sigma}$	Stress
$\boldsymbol{\sigma_n}$	Stress at data point ‘n’
$\boldsymbol{\sigma_n'}$	Stress value of the LEPP model if yield strain is assumed at $\boldsymbol{\varepsilon_n}$

L	Structures' total column height
δ	Vertical distance between apex of hexagon to highest point of vertical cell wall
X	Width of cushioning structure
ε_y	Yield strain
E	Young's modulus
Subscript "**e**"	Denotes experimental value
Subscript "**s**"	Denotes property of the solid material making up the cell walls

LIST OF ABBREVIATIONS

AM	Additive Manufacturing
ANOVA	Analysis of variance
CAD	Computer-aided design
DM	Digital material
FGS	Functionally-graded structure
LEPP	Linearly elastic – perfectly plastic stress-strain model
pcf	Pounds per cubic foot
SIMP	Solid Isotropic Microstructure with Penalization
3D	Three-dimensional
2D	Two-dimensional
UTS	Ultimate tensile strength

CHAPTER 1 – INTRODUCTION

This chapter presents the thesis background, motivations, objectives and scope. The background discusses the capabilities of additive manufacturing (AM) systems and its potential in customizing cushioning structures to meet the demands of various applications. The absence of design restrictions with AM technology allow for customization of various products. This design freedom motivates this work on 3D printing optimized cushioning structures. The main objective of this work is to characterize and relate cellular structures to various design parameters to develop a methodology to optimize these parameters for various cushioning applications. This is further elaborated in this chapter.

1.1 BACKGROUND

Additive manufacturing (AM) or 3D printing is a robust layer-by-layer manufacturing of 3D components directly from computer-aided design (CAD) models. This is unlike conventional manufacturing methods which are considered as subtractive manufacturing [1]. AM technologies have great potential to improve the design and applications in various fields such as aerospace [2, 3], biomedical [4-7], automotive [8] and electronics [9]. Additionally, AM offers greater design freedom hence allows customization of common goods such as jewellery [10, 11]. Customization with AM comes with no added costs hence products of the same type can be customized to meet the users' specifications. One such application that can greatly benefit from the design freedom of AM is cushioning. The cellular microstructure and relative density of foams are some of the parameters that define its cushioning properties [12]. With AM, the structure can be customized to meet various cushioning applications.

Cushioning materials are any material that are utilized for energy absorption [13]. Cushions commonly exist as porous or cellular structures due to their distinctive and desirable mechanical properties which are ideal for cushioning purposes [14]. Cushions are used in many applications which require shock attenuation and energy absorption to prevent significant damage to the user and/or equipment that is being protected. Applications involving cushioning materials include product packaging [15], footwear [16] and personal protective gears [17].

Cushion selection is done with the aid of cushioning curves which represent a material's ability to reduce shock transmission to a product [18]. The process of generating a cushioning curve involves a large set of tests which is costly and time consuming. This is further amplified when a set of cushioning curves of various thicknesses are required for a cushion selection process. A cushion is selected for an application by comparing these cushioning curves to determine which cushion can meet the required shock absorption capacity for an object of a particular weight dropped from a certain height [15]. To summarize the current selection process, a cushion is selected from a range of available tested cushions. A cushion is not produced specifically for an application but is part of a general bulk production process based on a selection of fixed sizes and characteristics.

Conventionally, porous cushioning materials are manufactured chemically (foams) or by expansion/corrugation of sheet material (honeycombs) [19]. The relative density and properties can be altered by mixing polymer solution with other substances [20]. As seen in Figure 1-1a and 1-1b, the resulting pore microstructures are normally disordered. This simple manufacturing process, however, does not provide any control over the pore microstructure. This translates to a lack of control over the resulting material's properties.

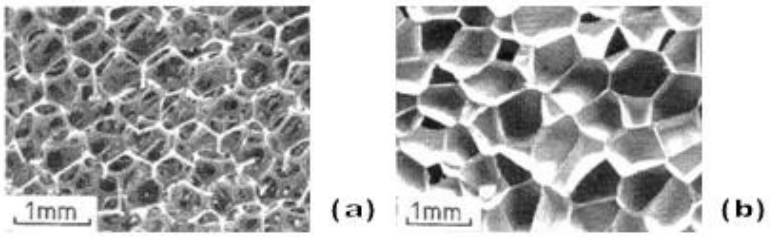

Figure 1-1: Cellular microstructure; (a) open cell foam; (b) closed cell foam [21]

Understanding the design parameters \of cushioning structures and the design freedom of AM technologies, optimized cushioning structures can be directly manufactured to meet the cushioning requirements of an application. The optimized cushion will be operating within its optimal design point and the tedious cushion selection process can be skipped entirely. Cushioning structures for various cushioning applications can be printed simultaneously with no added cost. This print on demand process would eliminate the need for extended storage of cushions and hence, the risk of material degradation. These can be realised with Polyjet printing process, developed by Objet (now Stratasys), which is capable of printing complex, porous polymeric structures with varying compositions of different resin types [22].

Polyjet is classified as a liquid based AM process, or specifically, a droplet based deposition process [23]. The droplets are deposited from a cartridge to a build tray through a nozzle head. The nozzle deposits the droplets onto the build tray according to the sliced computer aided design (CAD) data. Ultraviolet light simultaneously floods the build tray to cure the liquid droplets and the process is repeated layer by layer [24]. The use of water-soluble supports enables the printing of complex cellular structures with no added post processing as the support material can be removed easily. Figure 1-2 shows the schematic of the Polyjet process.

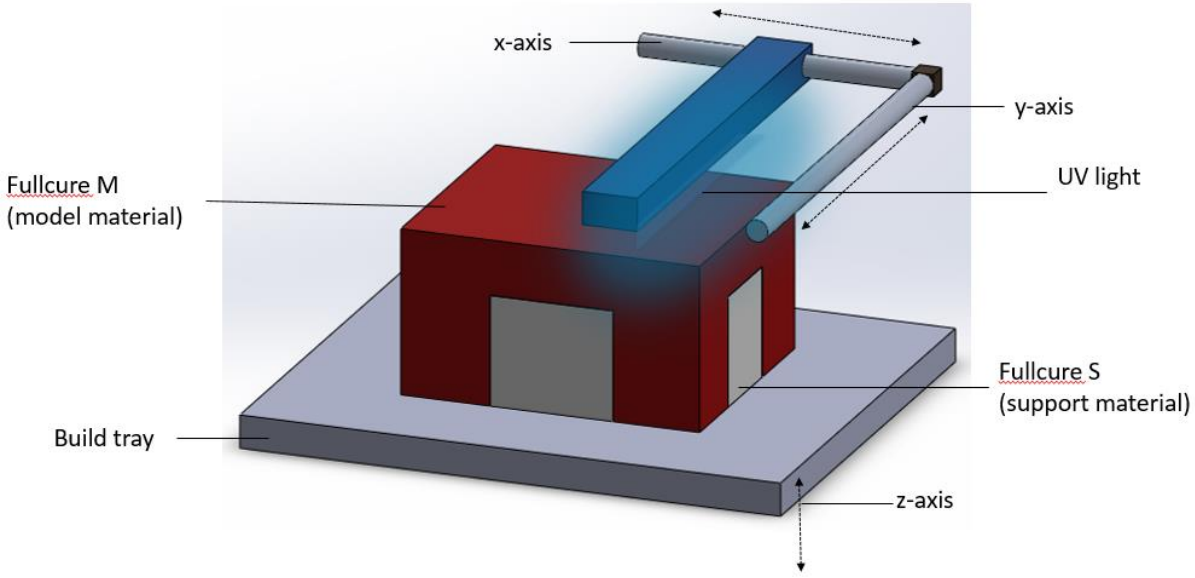

Figure 1-2: Polyjet process

1.2 MOTIVATIONS

As discussed in the previous section, current cushioning selection process is tedious and time consuming and may lead to underutilization of its cushioning capacity. Furthermore, for conventional foams, there is a reliance on its relative density when it comes to adjusting its mechanical properties. Therefore, there is much scope for improvement in efficiency and cost effectiveness in the cushioning selection process. In addition, with design freedom, new cellular structures can be explored which offers a range of adjustable design parameters and potentially offers a higher strength to weight ratio from current available cellular structures.

Conventionally, for high impact absorption applications, cushions are made thicker or denser which will result in heaver and bulkier products. For packaging purposes, heavier and bulkier cushion would lead to increase in transportation and handling costs. One solution is to optimize the cushion such that the weight is minimized. Additionally, with design freedom offered by AM technologies, a cellular structure can be design where the mechanical properties can be adjusted without any mass change. Prior to performing any optimization, an understanding of how design parameters affect the resulting mechanical properties and subsequently, cushioning properties, are required.

Polyjet is a good choice to start with as it offers the capability to print thin wall structures and digital materials (DM) with elastomeric properties ranging from soft to hard (low to high stiffness) by varying the polymeric composition. Also, as mentioned earlier, the support material used in the Polyjet printing process is water soluble which further amplifies the design freedom offered by allowing the printing of open-cell structures of any degree of complexity.

1.3 OBJECTIVES

The main objective of the research is to develop an optimizable cellular structure, to be 3D printed for various cushioning applications. Through this research, the understanding of the energy absorption in cellular solids will improve the efficiency and cost effectiveness of cushion selection process. Potentially, a cellular structure with higher strength to weight ratio may also be developed. In particular, the objectives of this research are:

1. To develop a novel cellular structure with variable mechanical strength whilst maintaining its weight.
2. To develop a mathematical model based on the design variables to predict the impact absorption capability of the cellular structure.
3. To formulate a design optimization problem that can be solved to create cellular structures that meet various cushioning requirements.

1.4 SCOPE

The scope of this research is as follows:

1. Review methods on evaluating cushioning properties.
2. Review the deformation mechanisms of cellular structures (honeycombs and foams).
3. Review of honeycomb and foam models, and cushioning properties.
4. Design and modelling of a novel honeycomb structure.
5. Mechanical testing of 3D printed novel honeycombs.
6. Establish relationship between design parameters with resulting cushioning properties of honeycombs.
7. Design an optimization algorithm for the novel honeycomb structure.

CHAPTER 2 – LITERATURE REVIEW

This chapter introduces cellular structures and cushioning materials. The conventional cushioning selection process will also be elaborated in detail. AM or 3D printing technology is then presented with a general review of the technology as well as an in-depth review on the Polyjet 3D printing process.

2.1 CELLULAR STRUCTURE

2.1.1 Introduction

Cellular structures are light weight structures made up of a network of interconnected unit cells [14, 25]. Cellular structures made up of two-dimensional cells or polygons are called honeycombs, those made up of three-dimensional cells or polyhedrons are called foams(Figure 2-1). Foams can further be classified into closed-cell and open-cell foams. A closed-cell foam has voids or air spaces separating each unit cell by cell walls while an open-cell foam has none [14] (Figure 1-1).

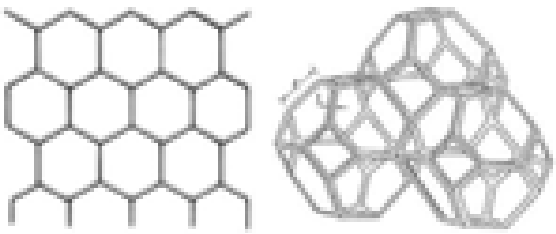

Figure 2-1: Honeycomb vs Foam [14]

The properties of cellular structures are dependent on the solid material properties, relative density of the structure and cell geometry. The cell shape determines the degree of anisotropy of the structure [14]. The microstructure of cellular structures is such that

it is packed to fill a plane for honeycomb, or space for foams, as seen in Figure 3 [14, 26].

2.1.2 Manufacturing of cellular structures

Almost any material can be used to manufacture cellular structures. Polymers are the most common material of choice when it comes to manufacturing cellular structures [14]. There are various ways of making a cellular structure and the required process depends on the type of cellular structure desired.

For honeycombs alone, there are four or more ways to make them [14]. One of the methods involves bonding corrugated sheet materials together [14, 27-29]. The sheet materials are corrugated by pressing it onto a half-hexagonal die. Bonding of the sheets may be achieved with either adhesives, welding, brazing, diffusion bonding, or thermal fusion [28] (Figure 2-2).

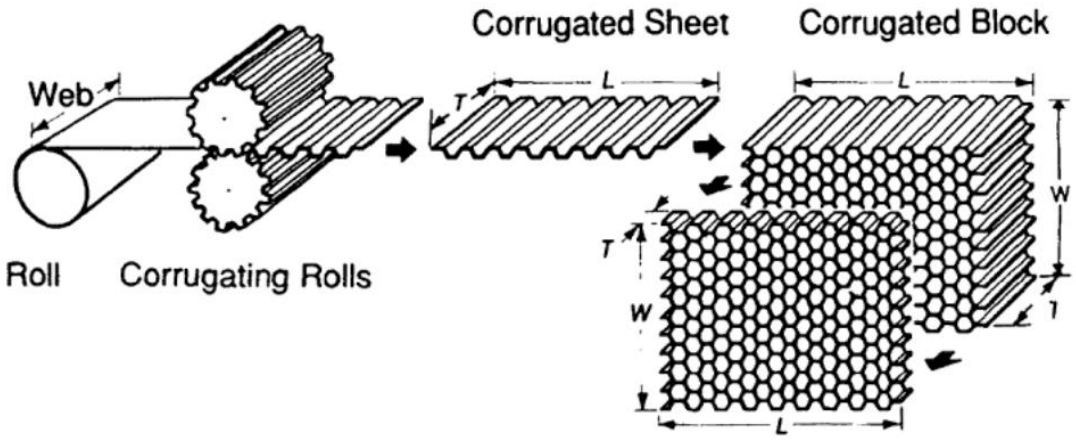

Figure 2-2: Corrugation of sheet materials and bonding of corrugated sheets to make a honeycomb core [28]

Another commonly used method is a combination of bonding and expansion [14, 28, 30]. This is considered to be a more efficient method compared to the corrugation and bonding process. The first step of this method is to bond or glue the sheet materials at specific, marked strips on the flat sheet. Multiple sheets are glued and stacked together

such that they are bonded at the specific strips. The stack is then pulled apart or expanded to result in a honeycomb structure. Similarly, bonding between the sheet materials can be achieved via adhesives, brazing, diffusion bonding, or thermal fusion [28] (Figure 2-3). Other methods include cast moulding and extrusion [14]. Both methods require a pre-made die with the desired geometry of the honeycombs.

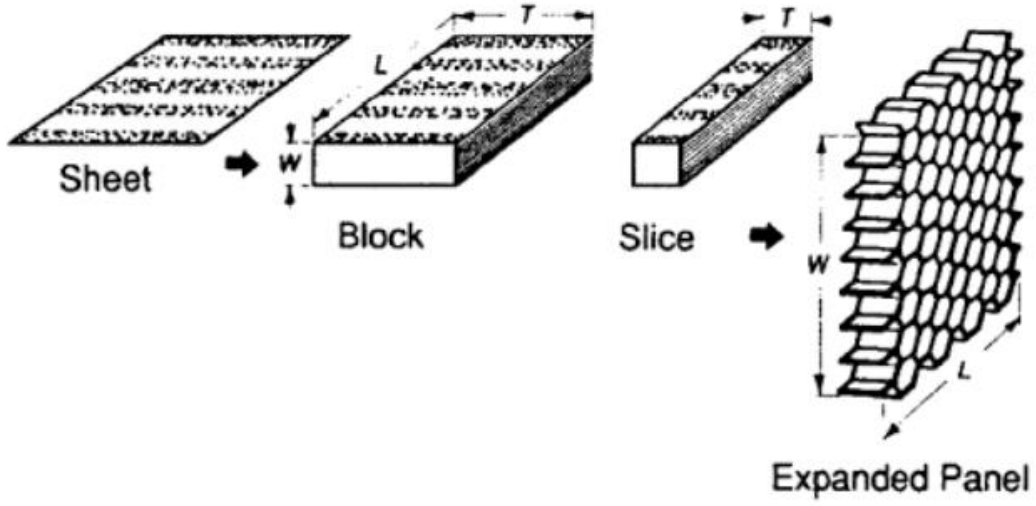

Figure 2-3: Bonding and expansion of sheet material to make a honeycomb core [28]

For foams, the manufacturing method depends on the material being foamed. Polymers are foamed by introducing gas bubbles into the liquid monomer or molten polymer. The cells nucleate as the bubbles grow in the liquid and solidify via polymerisation or cooling [31]. Introduction of the gas is done either via mechanical stirring or mixing with blowing agent. Blowing agents are introduced into the liquid in the form of inert gases at high pressure. The pressure is then reduced to cause the gas to expand forming bubbles [32]. Alternative methods include volatilizing molten polymers with low melting point to form vapour bubbles. The process to create open- or closed-cell foams is dependent on the fluid properties of the liquid monomer or molten polymer [14]. Microcellular polymer foams with very low relative densities (≈ 0.002) and small cell size (≈ 0.1 microns) are made by using one of the many phase separation methods. One

example is to deposit the polymer as a low-density gel in a fluid which is then evaporated away [33]. Generally, most polymer foaming process involves the introduction of gas bubbles into a liquid polymer or monomer (Figure 2-4).

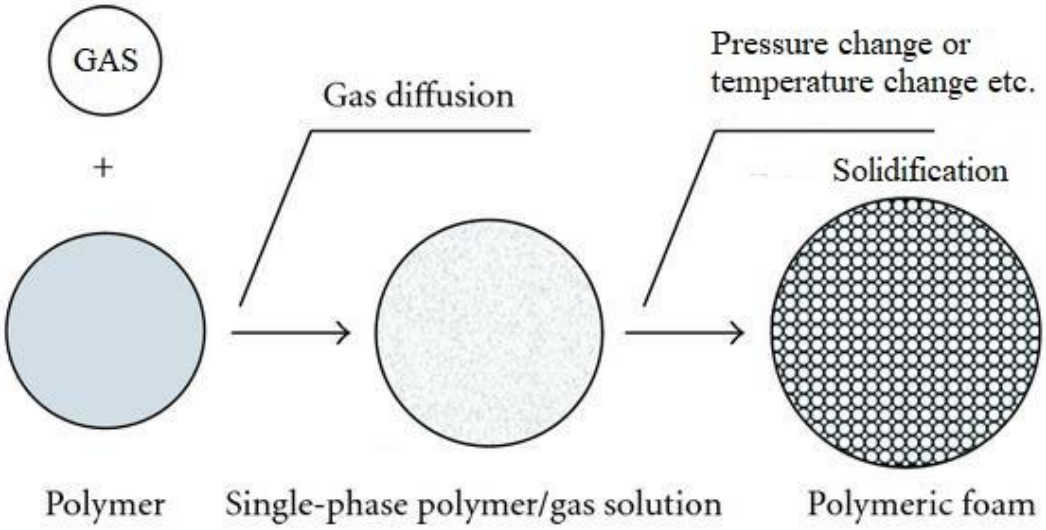

Figure 2-4: General polymer foaming process [34]

For metal foaming, there are several methods currently available. These methods can be classified into four categories, with each category indicating the starting state of the metal. Metal foaming can start with metal vapour, liquid metal, powdered metal and metal ions [35]. Alternatively, metal foaming processes can be categorized into liquid or solid state processing [36, 37]. The categorizations are similar, the only difference is that the latter does not include methods starting with metal vapour and ions. Metals can be foamed in a similar method to polymer foaming by introducing gas bubbles into liquid metal. This is known as direct foaming of metals [35]. Another method which involves liquid metal is the solid-gas eutectic solidification [38]. This method takes advantage of the fact that certain molten metal forms a eutectic mixture with hydrogen gas. Lowering the temperature of the mixture will transform the homogenous mixture into a heterogeneous one. The hydrogen gas will form the pores of the metallic foam

(Figure 2-5). Other metal foaming methods includes vapour deposition [39], electro-deposition [40], powder compact melting [41], casting methods [42], etc..

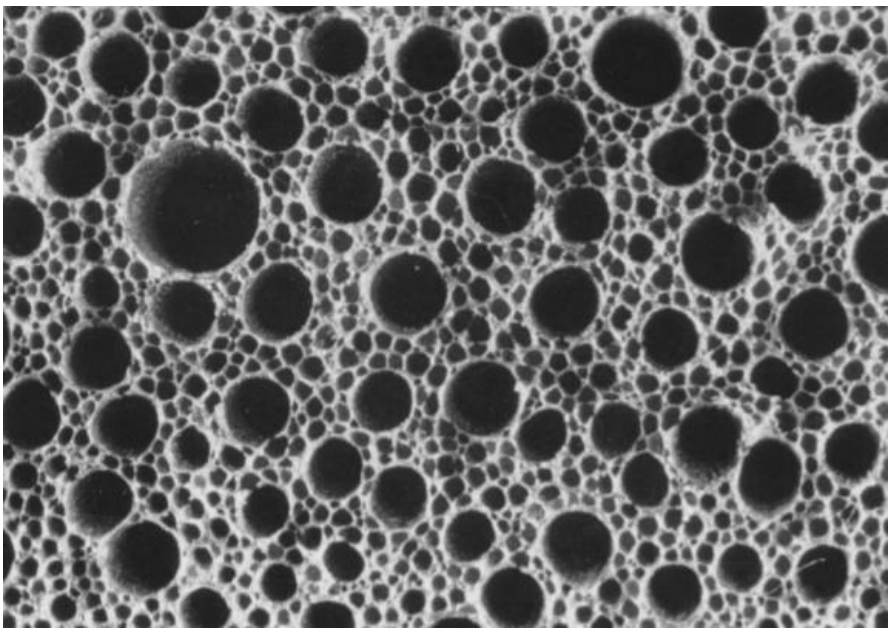

Figure 2-5: Metal foam produced by solid-gas eutectic solidification method

Glass foams are produced with methods similar to those used to foam polymers [14]. Carbon foams can be made via a moulding process with gel-like carbon fibers (or mesophase pitch) as the starting material [43]. The carbon fibers are melted in the mould and further heated to cause gas bubbles to evolve and hence foaming the melted pitch. Ceramic foams can be made by the chemical vapour deposition method [14].

There are various other methods available for the foaming of different materials. However, the outcome is a cellular material of three-dimensional network of interconnected cells which are randomly distributed within the structure. Unlike foaming processes, honeycomb manufacturing methods result in planned and uniformly distributed unit cells. However, for both types of cellular structures, applying conventional manufacturing methods limit the design freedom of the microstructures.

For honeycombs, the unit cell shape is limited to shapes which can be tessellated i.e. triangle, square and honeycomb. Furthermore, the manufacturing methods make

customization very costly. Every small adjustment in the honeycomb design parameters will add substantial costs to the manufacturing process. For foams, none of the current methods allow for control over the cell microstructure which includes the cell shape. Adjacent unit cells are not of the exact same geometry and are not uniformly arranged. Unlike honeycombs, where customization is costly, customization is not possible for foams due to the lack of control over the microstructural design. Present manufacturing methods allow for two ways of controlling the resulting foam properties by empirically adjusting the solid material properties and the average cell size, affecting the weight of the structure. The solid material properties can be adjusted by altering the chemical composition of the material while the cell size can be adjusted by controlling the growth of gas bubbles in the liquid material during the pore nucleation process (for processes with liquid as the starting material).

2.1.3 Mechanics of cellular structures

The properties of cellular structures are defined by two categories of parameters. One set of parameters is used to define the geometric structure of the cells [14]. This includes cellular size and shape which also defines the relative density of the structure. Relative density is deemed to be the most important property of any cellular structure and is defined as the ratio of the actual volume of solid material to the whole volume of the structure (or apparent volume) [14, 44] (Equation 1). The second set of parameters describes the properties of the material that make up the cell walls [14]. This includes the material density ($\boldsymbol{\rho_s}$), Young's modulus ($\boldsymbol{E_s}$), plastic yield strength ($\boldsymbol{\sigma_y}$), etc.

$$Relative\ density = \frac{Volume\ of\ Material}{Apparent\ Volume} = \frac{\rho}{\rho_s} \qquad (1)$$

where $\boldsymbol{\rho}$ and $\boldsymbol{\rho_s}$ are the density of the cellular structure and solid material respectively.

For any cellular structure, the relative density is a function of the ratio of cell wall thickness (***t***) to cell wall length (***l***) (Equation 2) [44]. Depending on the type of cellular structure (honeycomb, open-cell or closed-cell foams), the function takes a different form. The cell wall thickness and length are as shown in Figure 2-6.

$$Relative\ density = \frac{\rho}{\rho_s} = f\left(\frac{t}{l}\right) \quad (2)$$

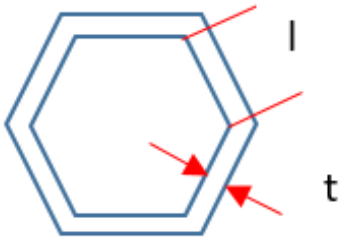

Figure 2-6: Cell wall thickness and length

When a cellular structure is compressed, the stress-strain curve has three distinct phases; linear phase, plateau phase and densification phase [14, 44, 45] (Figure 2-7). At low strains, the deformation is linearly-elastic. After which, the stress value remains relatively constant for a large strain range during the plateau phase. Lastly, the stress increases exponentially in the densification phase.

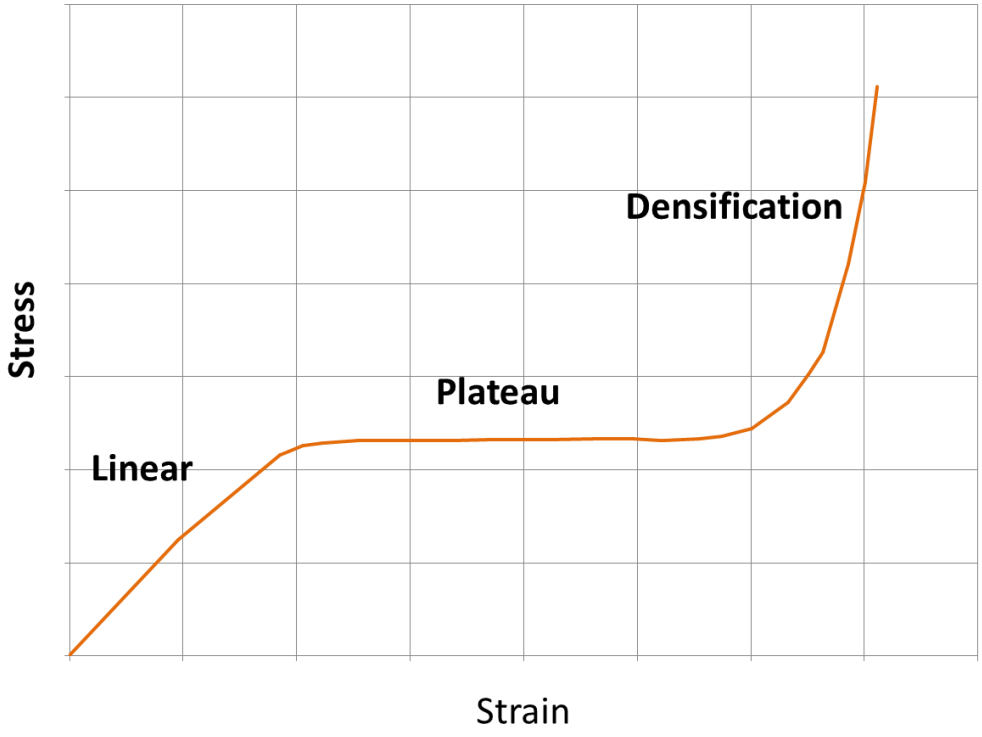

Figure 2-7: Three deformation phases during the compression of cellular structures

During the linear phase, the cell walls undergoes bending [44, 46-48]. Figure 2-8 shows the bending of cell walls in two-dimensional cellular structures (honeycombs) which also occurs for three-dimensional cellular structures (foams). The bending deflection of the cell wall is proportional to the applied load which collectively determines the vertical displacement (normal deflection) of the whole structure. Therefore, like any linear-elastic deformation, the normal strain experienced by the structure is linearly proportional to the applied stress. The structural modulus, $\boldsymbol{E^*}$, can be calculated based on the geometrical and material parameters of the structure. For regular hexagonal honeycombs, (Figure 3), $\boldsymbol{E^*}$ can be predicted with Equation 3 [46].

$$E^* = \frac{4}{\sqrt{3}}\left(\frac{t}{l}\right)^3 E_s \qquad (3)$$

where $\boldsymbol{t}$ and $\boldsymbol{l}$ are the cell wall thickness and length respectively as shown in Figure 2-8.

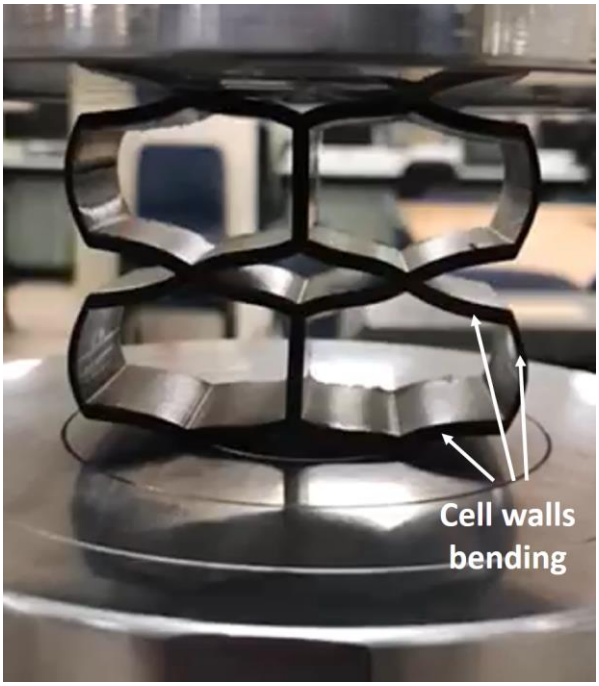

Figure 2-8: Cell walls bending during the linear-elastic deformation of a cellular structure

For open cell foams, E^* is proportional to t, l and E_s as described in Equation 4 [44].

$$E^* \propto \left(\frac{t}{l}\right)^4 E_s \tag{4}$$

Since relative density is a function of (t/l), the modulus of the structure is also proportional to the relative density, ρ/ρ_s. Therefore, a cellular structure with higher relative density will have a higher structural stiffness.

During the plateau phase, the cell walls either experience elastic buckling [14, 44, 46, 49], plastic yielding [14, 44, 46, 49] or brittle fracture [14, 44, 46, 50]. The type of deformation during this phase depends on the type of the materials making up the cellular structure. Elastomeric materials will go through elastic buckling, metals and other polymers will go through plastic yielding and ceramics will go through brittle fracture. Therefore, the onset of plateau is dependent on the type of material. For example, for elastic materials, the onset of plateau corresponds to the critical load at which buckling occurs [51]. The stress during the plateau phase remain relatively

constant or oscillates about an average value. For plastic-type materials (metals and most polymers), a series of fracture events occur during this phase.

In the densification phase, the rapid increase in stress is due to the opposing cell walls coming into contact with each other. This result in the cell walls being compressed. In other words, the increase in relative density of the structure up to the onset of densification results in the structure behaving as though it is a fully dense solid material. It seems obvious to deduce that the densification strain, $\boldsymbol{\varepsilon_d}$, is equal to the porosity of the structure as at this strain value, the pore spaces would have been fully compressed. However, the reality is that cell walls decreases at an earlier strain value. For foams, the onset of densification corresponds to an instantaneous relative density of approximately 0.5 while there are no conclusive data available for honeycombs [14]. Theoretically, the higher the structures original relative density, the earlier densification will occur [14].

For honeycombs, they are often used in sandwich panels [14, 52-54] with loads in the x_2-x_3 plane (Figure 2-9). For out-of-plane compression, the stress-strain response follows as similar fashion as seen in Figure 2-7 with the same three phases. During linear deformation, the core modulus $\boldsymbol{E_3}$ (defined by Equation 5) is actually the $\boldsymbol{E_s}$ scaled by the projected area of the network of cells which is equals to the relative density [53]. The onset of plateau phase is either due to the elastic buckling, plastic bending or brittle fracture of the cell walls [53]. However, unlike in-plane compression, densification is due to the bottoming out of the structure.

$$E_3 = \frac{\rho}{\rho_s} E_s \tag{5}$$

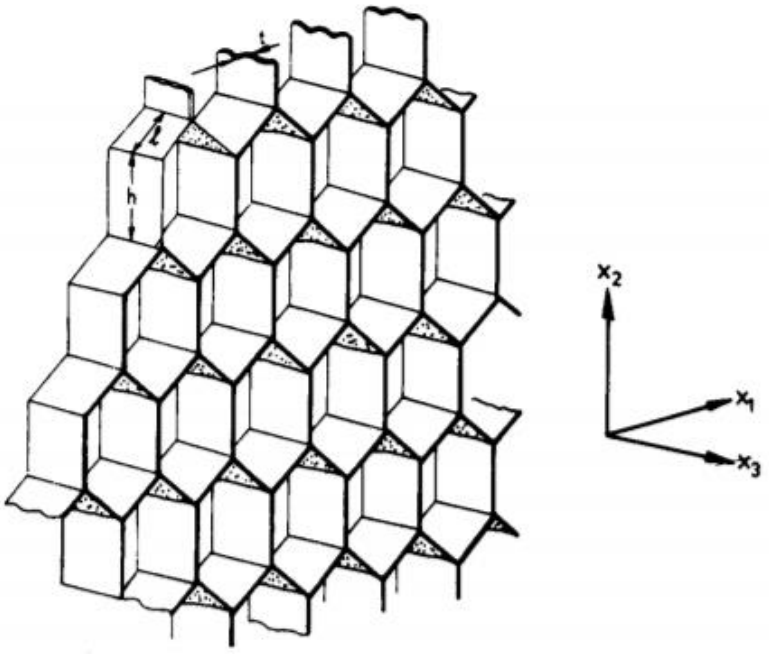

Figure 2-9: Honeycomb structure - in-plane properties refer to x_1-x_2 plane; out-of-plane properties refers to x_2-x_3 plane [46].

2.1.4 Identification of static compressive stress-strain properties

For polymeric cellular structures, there are no standard methods or specific methods suggested for obtaining the linear modulus. Literatures involving experiments on cellular polymers did not clearly state the method of obtaining the linear modulus and plateau stress presented in their data [55-57]. The ISO 13314 (Mechanical testing of metals – Ductility testing – Compression test for porous and cellular metals) [58] defines the linear modulus as the gradient of the unloading slope between 20% and 70% plateau stress (Figure 2-10). The plateau stress is obtained by calculating the arithmetic mean of the stress values between 20% to 30% or 40% strain (Figure 2-10). The densification point is the point on the curve where the stress is 130% of the plateau stress (Figure 2-10). Despite being an established method for cellular metals, the identified plateau stress may not be fully representative of the whole plateau phase. A method defining the average plateau stress (σ_p) was suggested by Li et al. [50] (Equation 6). This method is more representative of the whole plateau phase as it considers the amount of energy

absorbed during that phase. However, the densification strain ($\boldsymbol{\varepsilon_d}$) and onset of plateau strain ($\boldsymbol{\varepsilon_p}$) needs defining.

$$\sigma_p = \frac{\int_{\varepsilon_p}^{\varepsilon_d} \sigma(\varepsilon) d\varepsilon}{\varepsilon_d - \varepsilon_p} \tag{6}$$

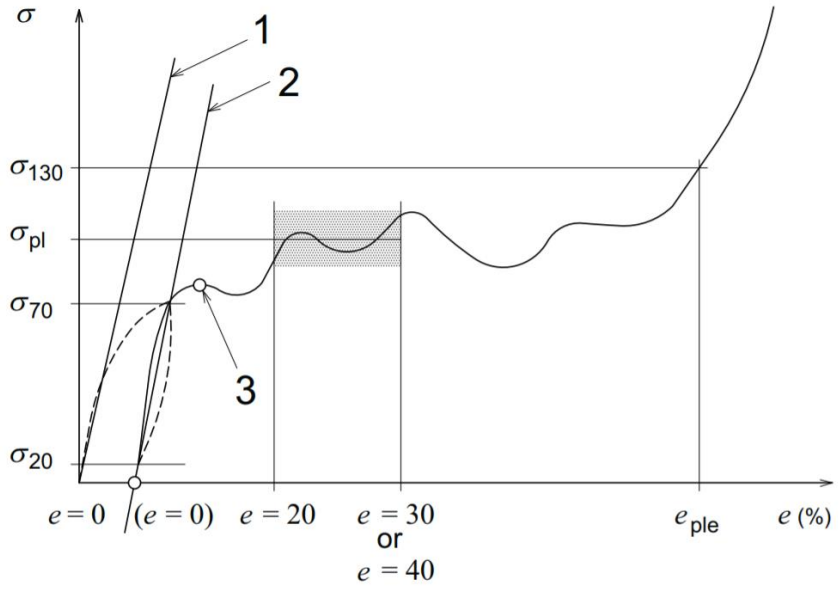

Figure 2-10: Identification of linear modulus, plateau stress and densification point based on ISO 13314 [58]

For the identification of densification strain, there are several additional methods available (refer to Figures 2-11 and 2-12):

Method 1: The strain value corresponding to the point of intersection of the plateau phase tangent and the densification phase tangent [59-61].

Method 2: The strain value corresponding to the point where the last local minimum just before the stress rises exponentially [62].

Method 3: The strain value corresponding to the point where its tangent's gradient is equal to the linear modulus [61].

Method 4: The strain value corresponding to the maximum energy to stress ratio [50].

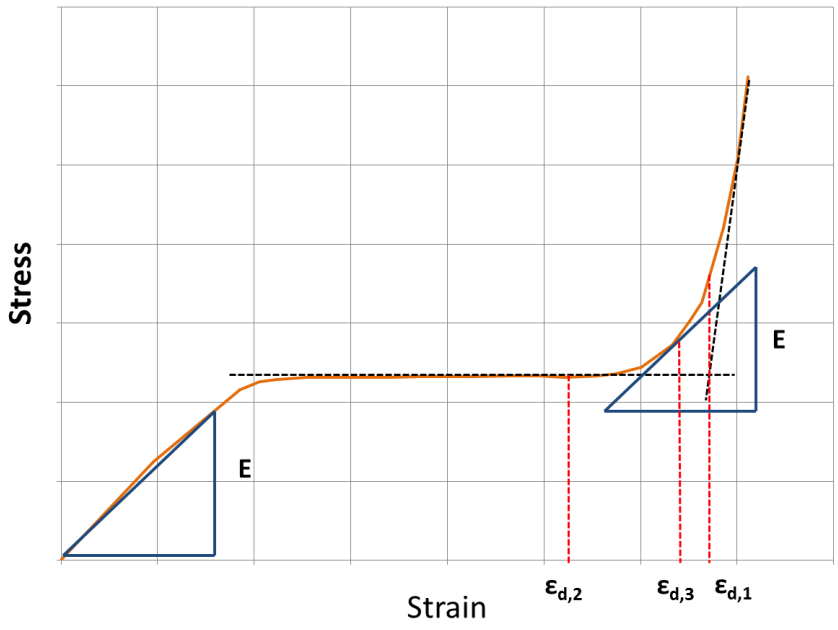

Figure 2-11: Densification strain obtained by methods 1, 2 and 3 reflected as $\varepsilon_{d,1}$, $\varepsilon_{d,2}$, $\varepsilon_{d,3}$ respectively.

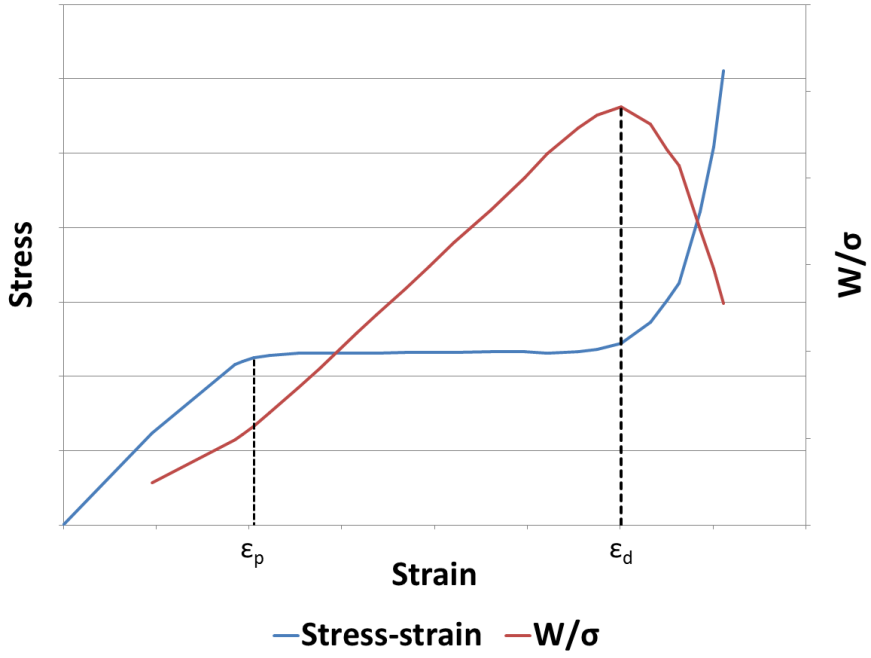

Figure 2-12: Densification strain determination based on method 4.

Methods 1 to 3 presents many uncertainties and increases the errors associated to the measured values of densification strain [50]. Method 4 on the other hand provides a unique and distinct strain value as the densification strain. It is not prone to any errors during the identification process.

The strain value at the onset of the plateau phase can be defined as the first peak stress as observed in Figure 2-13 [63]. However, for some cases, there is no visible peak stress between the linear and plateau phase (Figure 2-7). Alternatively, the 0.2% offset method can be applied to determine ε_p [58]. However, the initial gradient is used in the offset method, hence identified ε_p may still be within the linear phase.

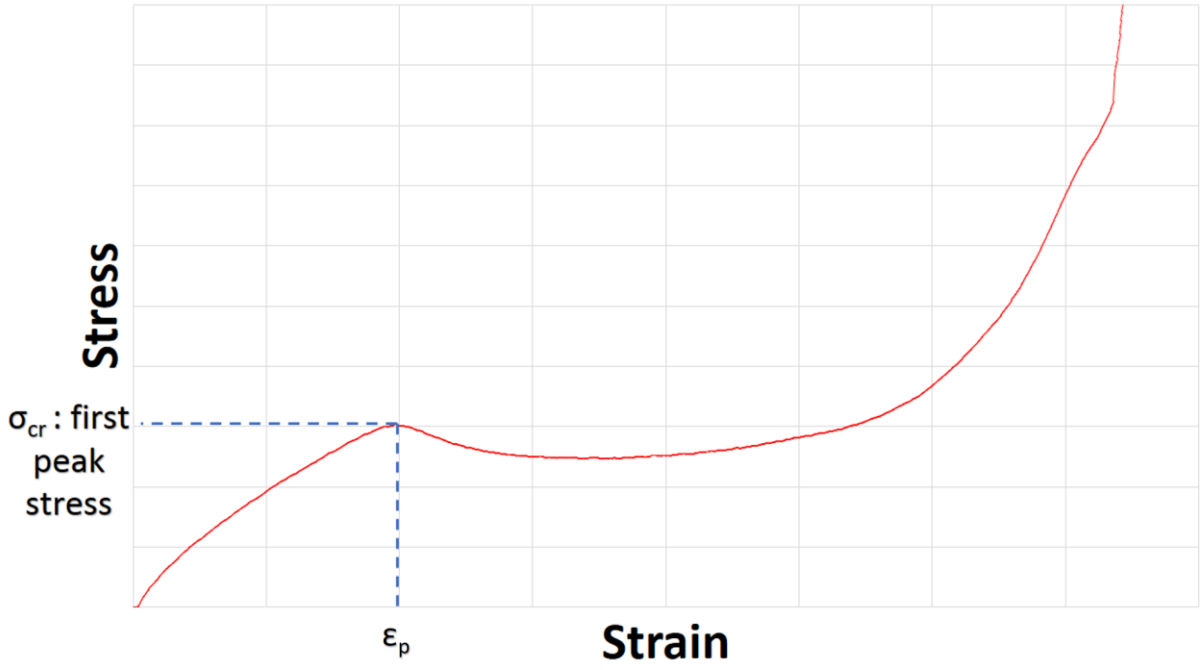

Figure 2-13: Definition of ε_p - strain value corresponding to first peak stress

2.1.5 Applications of cellular structures

Cellular structures offer an extension to properties already provided by dense solid materials [14]. The porosity offers superior thermal insulation as compared to solid materials [64]. The strength and stiffness of cellular structures are generally inferior to solid materials but due to their low relative densities, the resulting strength to weight ratios are better [14]. These extensions in properties make cellular structures ideal for various applications which will be discussed in this sub-section.

One such application is thermal insulation [64]. Foams are often used in disposable cups, ice boxes, etc. simply because they insulate well due to their porosity. Another

application where cellular solids plays a big role in is packaging [65-67]. As mentioned in Section 2.2.2, cellular structures offer a unique three phase stress response when compressed. The plateau phase is ideal for absorbing large amount of energy while keeping the stress relatively constant. Furthermore, due to their low strength, this stress value will also be low hence preventing any damage to the packaged item.

Cellular structures are also employed as structural parts in planes [68, 69], space vehicles [70], sports equipment [71], etc. This is due to their superior strength to weight ratio which offers the required structural strength and stiffness while at the same time being lightweight. Also, due to their high porosity (air trapped in the pores) , cellular structures are also used to provide buoyancy [72]. Polymeric foams are widely use in boats and floating structures due to their high buoyancy. Apart from the marine industry, buoyancy of cellular structures are also proving to be useful in the biomedical industry as floating drug delivery system in the stomach [73].

A common method of designing cellular structures is by way of topology optimization [74]. This method basically optimizes the material distribution throughout a design space for a certain load bearing application to result in a lattice or cellular structure instead of a fully dense solid structure. Recent advances in cellular structure design includes structures with negative Poisson's ratio [75] and utilizing re-entrant inclusions to improve the structure's stiffness [76]. Re-entrants are deviations of the cell shape and/or design from the regular design. These deviations act as reinforcements to the structure and thus stiffening it.

2.2 CUSHIONING MATERIALS

2.2.1 Introduction

Cushioning materials are widely used in various applications which include packaging [77], automotive safety features [78] and therapeutic footwear [20]. Cushioning materials are also utilized in the sports industry, in the soles of running shoes [79], gym mats [80], helmets [81], etc. For all applications, the main function of cushioning materials is to absorb kinetic energy to prevent damage to the protected item which in certain applications can be a human being or a human body part. For example, the cushions found in helmets or running shoes is to absorb the impact energy due to a blunt force to the head or the landing of the foot respectively. The mode of energy absorption of cushioning structures is through the deformation (elastic and/or plastic) of its structure or micro-structure [78].

Various forms of materials are being used for the purpose of cushioning. Earlier cushioning methods were variations of polymer foam peanuts (Figure 2-14) [66], corrugated fibreboard [67], bubble wraps [82], etc. which are mainly used in the packaging industry to protect the item during transportation. Currently, these cushions are less widely used as compared to polymeric foams. Polymeric foams are increasingly being used for various cushioning purposes due to their low apparent densities and they can easily be made into complex geometries [78].

Figure 2-14: Polymer foam peanuts

Apart from foams and other cushions mentioned earlier, shock absorbers are technically cushions as well due to their function of energy absorption [83]. These normally require the interaction with viscous fluids to produce the cushioning. Shock absorbers are commonly used for heavy duty applications such as vehicles suspension system and vibration control.

2.2.2 General cushioning principles

For a cushion to perform its task effectively, there are six general principles that should be adhered to. These are [13]:

1. Irreversible energy conversion: convert most of the impact energy into inelastic energy by plastic deformation or other dissipation processes.
2. Restricted and constant reactive force: peak reaction force of a cushion should be kept below a threshold and ideally the reaction force should remain constant during the large deformation process of the cushion.

3. Long stroke: energy absorbed is force times displacement, hence the displacement i.e. stroke of the cushion should be sufficiently long.
4. Stable and repeatable deformation mode.
5. Lightweight and high specific energy absorption capacity.
6. Low cost and easy installation.

From the general principles of cushioning material, the ideal cushion's stress-strain curve can be demonstrated. An ideal cushion undergoes purely plastic deformation hence irreversible energy conversion, the maximum stress is constant hence constant reaction force and it is fully compressible hence for thick cushions, long stroke can easily be achieved [13, 21]. The stress-strain curve of an ideal cushion is hence rectangular as seen in Figure 2-15.

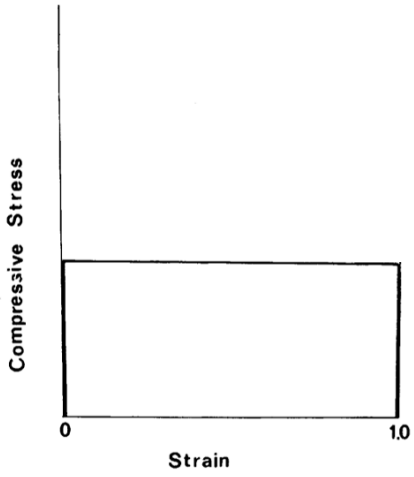

Figure 2-15: Stress-strain curve of an Ideal Foam [21]

2.2.3 Cushioning properties

Several cushioning properties can be extracted from the stress-strain curve in a compression test of a cushioning material. The energy absorbed by the cushion is known

as the energy absorption capacity (**W**) which is basically the area under the stress-strain curve as given by Equation 7.

$$W = \int_0^{\varepsilon} \sigma d\varepsilon \tag{7}$$

Equation 8 is the energy absorption efficiency which is the ratio of the energy absorbed by a cushion to that by an ideal cushion with both having the same maximum stress. As seen in Figure 17, the energy absorbed by an ideal cushion is equivalent to the maximum stress multiplied by a strain of 1. An ideal cushion undergoes plastic deformation from a strain of 0 to 1 hence resulting in a rectangular stress-strain curve. Another parameter, the cushioning capacity is the inverse of the energy absorption efficiency as given in Equation 9. Cushioning capacity is the measure of the cushion's performance [65].

$$W_{eff} = \frac{W}{\sigma} \tag{8}$$

$$C = \frac{1}{W_{eff}} \tag{9}$$

The ideality of the foam is the energy absorption ratio between a real cushion to that of an ideal one which is compressed to the same strain and maximum stress as defined in Equation 10.

$$I = \frac{W}{\sigma\varepsilon} \tag{10}$$

This information will allow us to measure the cushioning capacity of the material. However, when it comes to selecting a material for cushioning applications, cushioning curves are required.

2.2.4 Methods of evaluating and selection of cushioning materials

Equations 7 to 10 are used to evaluate the cushioning performances of a certain material and/or structure. However, based on this evaluation alone, it is inaccurate to conclude if one cushion is better than the other. Some cushions are better suited for a low impact function while others are better suited for high impact functions. For example, the cushions used in chairs are suited for low impact functions whereas that found in the soles of running shoes are for high impact. Therefore, it is important to couple cushioning evaluation with cushioning selection methods to identify which cushions are better suited for which type of working conditions.

Four methods of cushion selection are discussed:

Method A:

In Method A, cushions are selected by first identifying what is the specific amount of energy required to be absorbed for a certain application. Subsequently, the stress due on the cushions for it to absorb the required energy are compared [78]. This is done by identifying the stress where the area under each foam's stress-strain curve would be equal to the identified required amount of energy to be absorbed. The result of this process is shown in Figure 2-16. The foam with the lowest stress value will be selected (ρ_2 in this case). Density here refers to the density of the different foams.

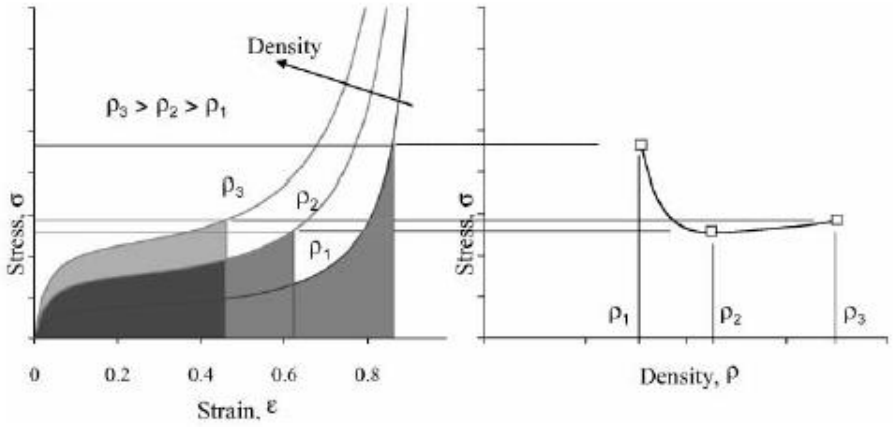

Figure 2-16: Foam selection based on specific amount of energy absorbed [78]

Method B:

The stress on the cushion is translated to the force on the cushioned object hence the deceleration on the object. To prevent damage to the object, the stress should not exceed a certain value. In this situation, Method B is employed where the cushion that absorbs the most energy at a particular stress limit will be selected [78]. Unlike Method A, an absorbed energy vs stress graph is used instead (Figure 2-13). As such, the foam which absorbed the highest amount of energy at any pre-determined stress value can be easily identified (Figure 2-17). The pre-determined stress value is normally dependent on the application. For example, when selecting a packaging cushion to be used to contain glassware for transportation, the maximum stress value must not exceed the value at which brittle fracture of the glassware starts to occur. Density here refers to the density of the different foams.

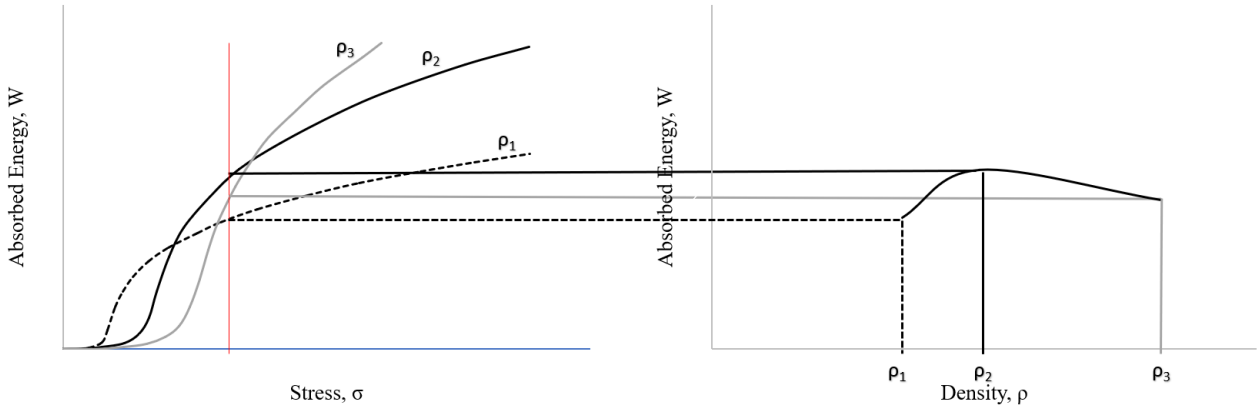

Figure 2-17: Foam selection based on energy absorbed at a certain stress limit [78]

Method C:

Using energy absorption diagrams for cushion selection is however an estimation method. It does not take into account the optimum strain condition when the cushion experience optimum energy to force ratio [84]. Method C therefore selects a cushion based on its optimum design point which can be found at the maximum point of the absorbed energy to applied stress ratio (Figure 2-18 in blue – W/σ curve).

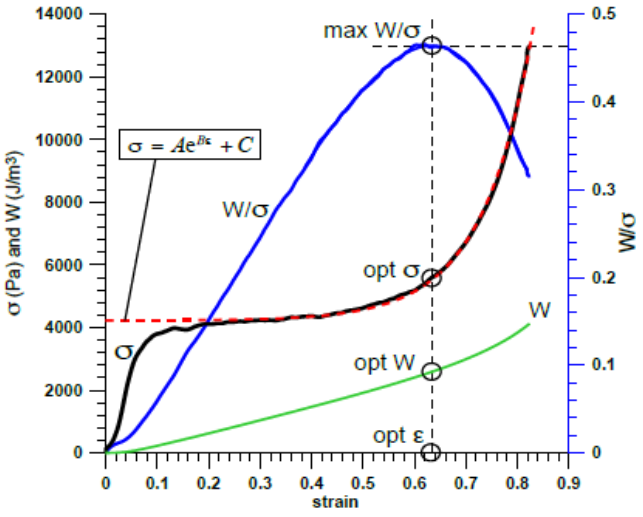

Figure 2-18: Obtaining optimal design point [84]

Method D:

Cushion curves are however the method of choice for the packaging industry [15]. The method of cushion selection with cushioning curves and the generation of cushioning curves are reviewed in the following section.

2.3 CUSHIONING CURVES

Cushioning curves represents a material's ability to reduce shock transmission to a product [18]. Shock is measured in terms of ***G***, which is the deceleration experienced by the product. Figure 2-19 is an example of a cushioning curve which is obtained from testing a 3D printed cellular solid. As observed, the ***G*** is plotted against the static stress (σ_{static}) which is the weight divided by the contact area. Each material will have its own unique cushioning curve for a particular drop height (***H***) and particular foam height (L_y).

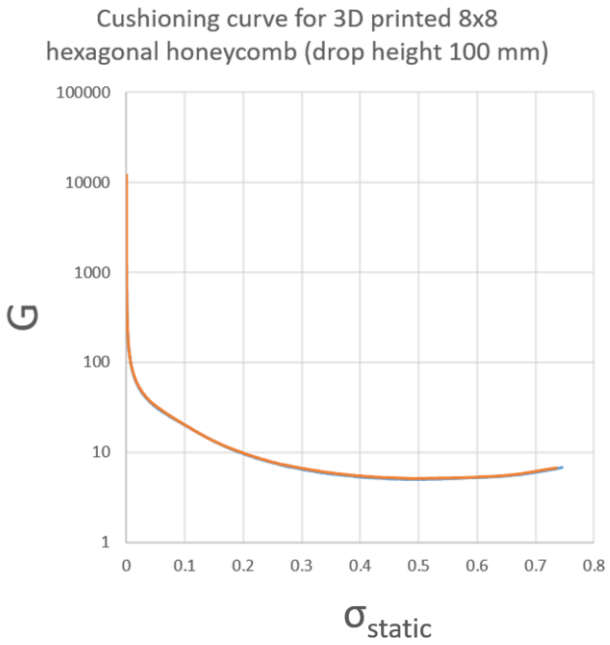

Figure 2-19: Cushioning curve for 3D printed honeycomb (L_y = 100 mm)

In the packaging industry, foam selection is a systematic process where packaging engineers or designers first need to consider the maximum ***H*** the package will experience. A set of cushioning curves, for a pre-defined ***H***, representing various cushioning materials with varying L_y (thickness) are compared. The packaging designer or engineer then identifies the item's fragility and σ_{static} [15]. Fragility is basically the maximum allowable deceleration or absolute acceleration an object can experience

before being damaged. It is measured as a ratio to gravitational acceleration (9.81 m/s^2) in terms of $\boldsymbol{G}$ (i.e. 1 G = 9.81 m/s^2).

Cushioning curves which are below the item's fragility value at the required $\boldsymbol{\sigma_{static}}$ can be selected for the cushioning application. For example, in Figure 2-20, the 3", 4" and 5" foams can be selected.

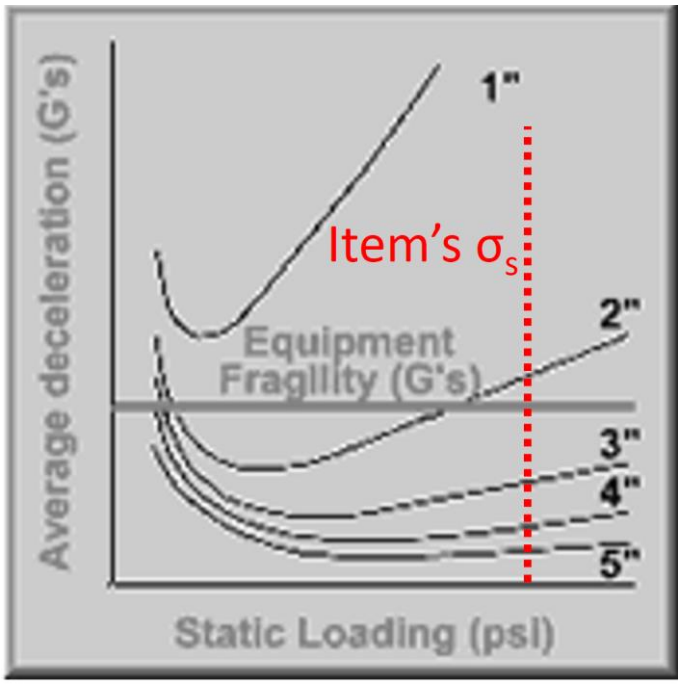

Figure 2-20: Set of cushioning curves for a foam of various $\boldsymbol{L_y}$ in inches [85]

The cushioning curve is obtained by performing a set of experiments. Each point of the cushioning curve is obtained by performing a drop-test of a weight corresponding to a $\boldsymbol{\sigma_{static}}$ value on the curve. The resulting $\boldsymbol{G}$ measured by an accelerometer is then plotted. Performing various drop-tests of different weights will result in a set of plotted points which are then fitted with a best fit curve to obtain the final cushioning curve [86]. More drop-tests are required if a higher accuracy is desired. For a comprehensive set of curves for a certain material, large number of tests and hence test specimens are required which is very costly and time consuming.

Alternative methods of obtaining cushioning curves have been suggested. These methods are less time consuming and more cost effective but have varying degree of accuracy when compared to the conventional method [18, 86, 87].

2.3.1 Cushioning curves from static compression data

Gruenbaum and Miltz [87] proposed the use of static compressive stress-strain data to predict the cushioning curve for a range of drop-height (***H***) and foam height ($\boldsymbol{L_y}$). This method is the least time consuming and most cost-effective method as only a simple static compression test is required. However, the accuracy of the cushioning curves decreases with increasing ***H*** and decreasing $\boldsymbol{L_y}$. This method assumes that for any ***H***, the amount of energy absorbed during a drop-test is the same during static compression. This is illustrated in Figure 2-21 and Equation 11.

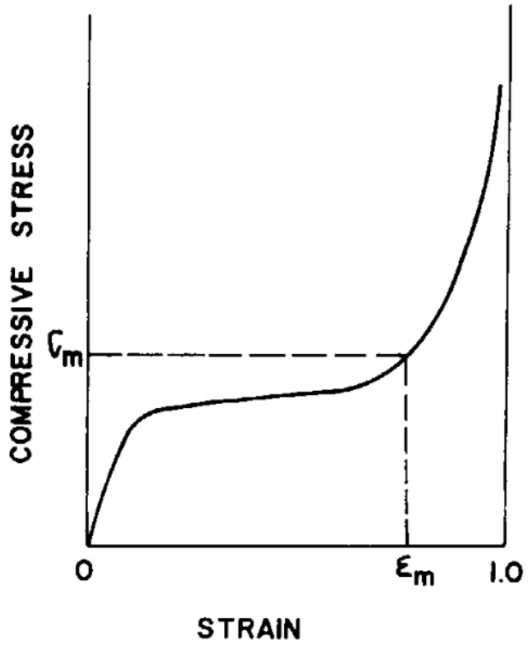

Figure 2-21: Energy absorbed during static compression equals to the energy absorbed during drop test [87]. ε_m is the compressive strain experience during drop-test, σ_m is the corresponding stress value.

$$P.E = mgH = AL_y \int_0^{\varepsilon} \sigma d\varepsilon \tag{11}$$

where $\boldsymbol{L_y}$ is the height of the foam, $\boldsymbol{A}$ is the contact area of the foam, $\boldsymbol{\sigma}$ is the static stress value which is a function of strain, $\boldsymbol{m}$ is the mass of the impactor, $\boldsymbol{H}$ is the drop height and $\boldsymbol{g}$ is the gravitational acceleration.

From Equation 11 and knowing that $\boldsymbol{\sigma_{static}}$ is weight ($\boldsymbol{mg}$) divided by $\boldsymbol{A}$, Equation 12 is obtained.

$$\sigma_{static} = \frac{mg}{A} = \frac{L_y}{H} \int_0^{\varepsilon} \sigma d\varepsilon \tag{12}$$

As mentioned earlier, $\boldsymbol{G}$ (a dimensionless unit to represent fragility) is basically the deceleration magnitude as a ratio of gravitational acceleration (Equation 13).

$$G = \frac{a_{deceleration}}{g} = \left(\frac{F_{reaction}}{m}\right)\frac{1}{g} = \frac{\sigma_{reaction} A}{mg} = \frac{\sigma_{reaction}}{\sigma_{static}} \tag{13}$$

where $\boldsymbol{\sigma_{reaction}}$ is the static reaction stress value when the foam is compressed up to a certain strain.

From Equations 11 to 13, $\boldsymbol{G}$ vs $\boldsymbol{\sigma_{static}}$ can be plotted which is, in fact, the cushioning curve. Foam height ($\boldsymbol{L_y}$) and drop-height ($\boldsymbol{H}$) are considered constants. Therefore, adjusting these values provides a range of cushioning curves.

2.3.2 Stress-energy cushioning curves

Daum [18] suggested an empirical method involving the relationship between dynamic stress and dynamic energy to obtain cushioning curves. Dynamic stress and dynamic energy are defined by Equations 14 and 15.

$$Y = Dynamic\ stress = G\sigma_{static} \tag{14}$$

$$X = Dynamic\ energy = \frac{\sigma_{static} H}{L_y} \quad (15)$$

He described the relationship between Y and X as an exponential one as shown in Equation 16 [18].

$$Y = Ae^{BX} \quad (16)$$

where A and B are constants which are empirically determined.

This method requires some amount of experimental work to obtain drop-test data for various combination of $\boldsymbol{H}$, $\boldsymbol{\sigma_{static}}$, $\boldsymbol{L_y}$ and the corresponding $\boldsymbol{G}$. Dynamic stresses and energies are then calculated from these data and are subsequently plotted. Curve fitting is performed to identify the constants A and B. With the constants determined, cushioning curves for various $\boldsymbol{H}$ and $\boldsymbol{L_y}$ can be generated by using Equation 16. To obtain accurate values of constants A and B, sufficient drop-tests should be performed for a desirable curve fit.

2.3.3 Dynamic factor

Sek and Kirkpatrick [86] proposed introducing a dynamic factor, $\boldsymbol{c(\dot{x}, x)}$, to the calculated $\boldsymbol{G}$ values. The dynamic factor is a function of speed (strain rate) and displacement (strain) of the deformation on the foam which can be directly translated to strain and strain rate. Strain rate is proportional to drop-height. The higher the drop-height, the higher the potential energy and therefore, higher strain rate during impact. The strain is related to the thickness of the foam, lower thickness will result in higher strain value.

The derivation of the dynamic factor starts with the force balance equation as shown in Equation 17.

$$m\ddot{x} = F(x) + F_{dynamic}(\dot{x}, x) \tag{17}$$

where $\boldsymbol{F(x)}$ is the static load (a function of displacement) and $\boldsymbol{F_{dynamic}(\dot{x}, x)}$ is the dynamic load (a function of displacement and velocity).

Combining Equation 12 and 17 and dividing by A produces Equation 18 and 19.

$$\sigma_{static}/_{g}\,\ddot{x} - \left[1 + \frac{\sigma_{dynamic}(\dot{x}, x)}{\sigma(x)}\right]\sigma(x) = 0 \tag{18}$$

$$\sigma_{static}/_{g}\,\ddot{x} - c(\dot{x}, x)\sigma(x) = 0 \tag{19}$$

where $\boldsymbol{c(\dot{x}, x)}$ is the dynamic factor.

The significance of the dynamic factor allows the generation of cushioning curves with a modified Equation 13 (now Equation 20):

$$G = c(x; x)\frac{\sigma_{reaction}}{\sigma_{static}} \tag{20}$$

With the added factor to static compressive stress values ($\boldsymbol{\sigma_{reaction}}$ and $\boldsymbol{\sigma_{static}}$) to account the dynamic effects such as drop-height and foam height. Similar to the stress-energy method, sufficient drop-tests at various drop-heights and foam height should be performed to accurately determine the function which governs $\boldsymbol{c(\dot{x}, x)}$.

2.4 OPTIMIZATION OF CELLULAR STRUCTURES

Cellular structures are desirable due to their high specific strength and stiffness. However, there are many different types of cellular structures made of different cellular shapes, sizes and topology. Each type has its own unique set of mechanical properties. To determine an exact type of cellular structure for a certain application would require mechanical data from all the different types of structure which is very challenging. Topology optimization, as mentioned in Section 2.1.5, in laymen terms, is a process which determines the most optimum material distribution in a design space for a set of loading and boundary conditions [74]. This results in a matrix of voids and solid material which can be considered as a cellular structure (or lattice structure).

More specifically, topology optimization is a mathematical method which discretize a design space into finite elements. Depending on the loading and boundary conditions, each element is either a void or solid material [88-90]. The raw optimized structure is normally illustrated visually in grayscale with black being the material phase and white the void phase. However, there are instances where the optimization returns an intermediate result for some elements i.e. a mixture of void and solid material. Figure 2-22 depicts an example of an optimized design space in greyscale for a simple loading condition.

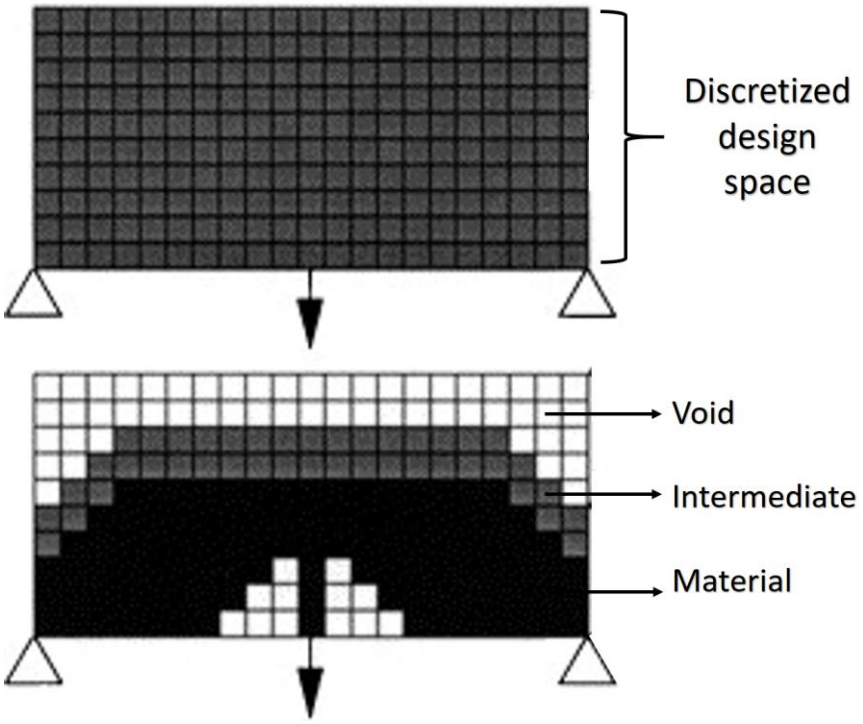

Figure 2-22: Optimized structure (lower figure) for a simple loading and boundary condition in greyscale depicting the void, material and intermediate phase [91]

A common method to further optimized the design space without any intermediate phases is the Solid Isotropic Microstructure with Penalization (SIMP) method [92]. The SIMP method basically penalizes the densities of the finite elements such that the chances of having intermediate phases in the optimized solution is greatly reduced. Alternatively, the elements with intermediate phases or densities can be filled with cellular structures which satisfy the density of the intermediate phases as shown in Figure 2-23 [93]. In other words, the final structure is a network of cellular structures within a cellular structure which can be considered as a Functionally Graded Structure (FGS).

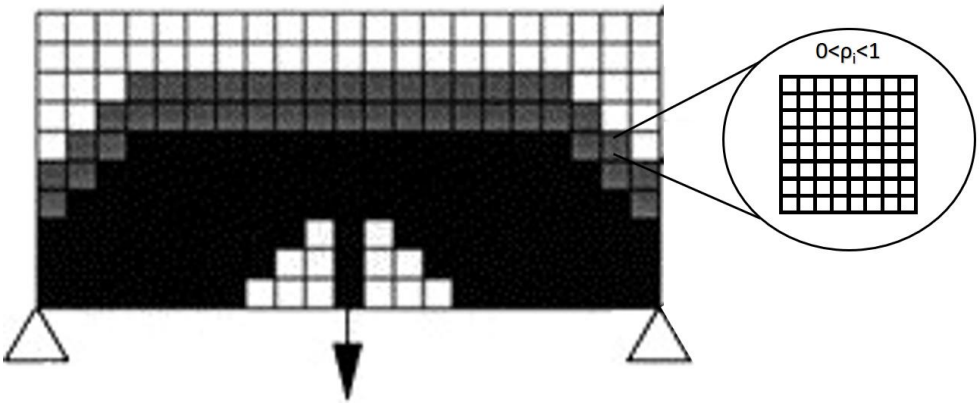

Figure 2-23: Grey elements (intermediate densities) replaced with micro-cellular structures with densities matching those of the elements which were obtained during the initial topology optimization process

It was earlier pointed out in Section 2.1.3 that the relative density of a cellular structure is one of the most important parameters which determines its properties. However, Tantikom et al [94] and Burgeuno et al [95] observed that for cellular structures with similar relative densities and structure, scaling the unit cells will result in varying mechanical properties (Figure 2-24). Burgeuno et al termed this phenomenon as the scale effect. Bauer et al concludes that scaling down the unit cells size would strengthen and stiffen the cellular structure due to mechanical size effect [96]. Additionally, for any cellular structure, the outer cell walls do not bear any load and are therefore deemed to be free from stress [97]. Therefore, decreasing the unit cell size will increase the number of cells across the width of the structure thus increasing the ratio of load bearing cell walls to total number of cell walls. As such, the scale effect can be integrated with topology optimization whereby the intermediate phases are filled up with cellular structures of similar relative densities but varying unit cell size.

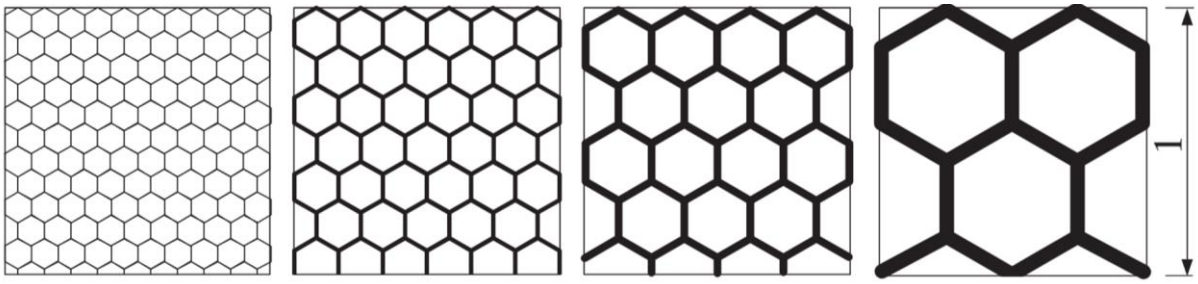

Figure 2-24: Hexagonal honeycombs with similar relative density and structure but different unit cell sizes [93].

2.5 3D PRINTING

As mentioned in Section 1.1, additive manufacturing (AM) or 3D printing is a group of manufacturing techniques which directly generates a part from a 3D Computer Aided-Design (CAD) file. The CAD files are sliced into horizontal layers which are printed in a sequential manner to produce the physical part [1]. AM provides greater control over the manufacturing processes as compared to conventional manufacturing techniques such as subtractive manufacturing and formative manufacturing processes [98]. Over the years, the improvement and further refinement of AM technology have resulted in the commercialization of AM in various applications which include direct and indirect tooling [99, 100], aerospace [2, 3], jewellery [101], medical implants and many more. As per Table 2-1, AM processes are usually classified according to the original form of material; powder, liquid and solid [102].

Table 2-1: Different types of AM processes categorized based on the raw state of material

Liquid	Powder	Solid (Laminates)
Stereolithography **(SLA)**	Electron beam melting **(EBM)**	Laminated object manufacturing **(LOM)**
Digital light projection **(DLP)**	Selective laser sintering **(SLS)**	Fused deposition modelling **(FDM)**
Multi-jet modelling **(MJM)**	Direct metal laser sintering **(DMLS)**	
	Selective laser melting **(SLM)**	
	Binder jetting **(BJ)**	
	Laser metal deposition **(LMD)**	

For the purpose of manufacturing cellular structures, 3D printing offers customized structures at no added costs due to the design freedom offered by its processes. 3D printing of honeycombs and foams with superior properties are becoming more common. Structures with properties such as negative stiffness [103-105], negative Poisson's ratio [106] and planned stiffness [107] can be easily 3D printed. All these structures have complex geometries, as shown in Figure 2-25, which makes it complicated to be manufactured conventionally.

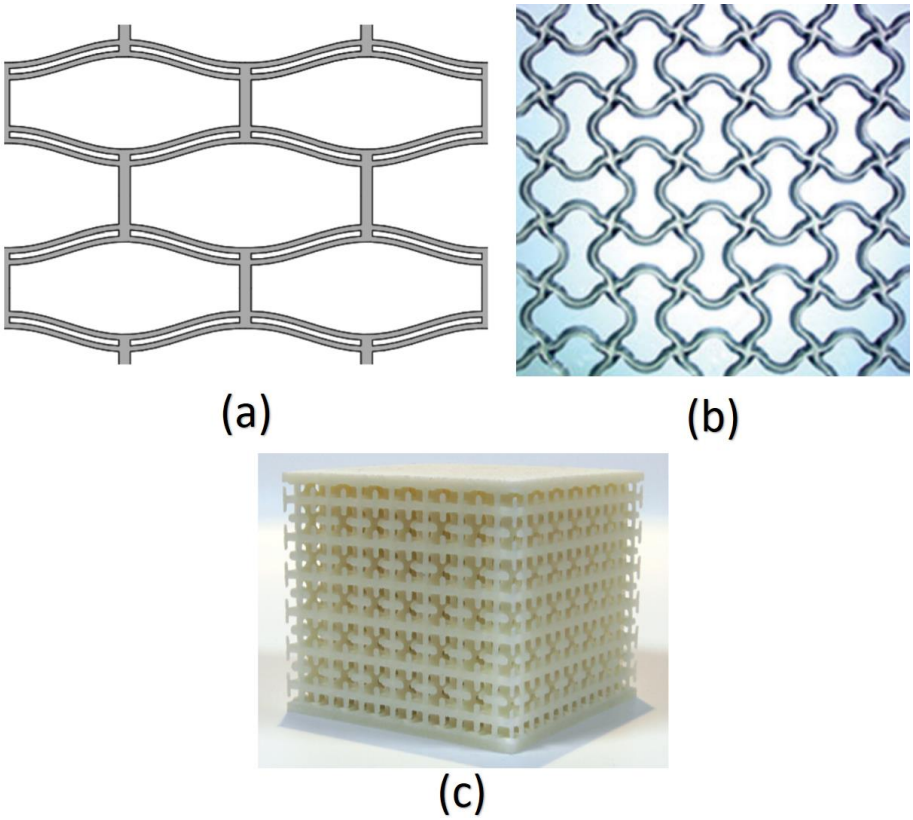

Figure 2-25(a): Honeycomb structure which exhibits negative stiffness [103]. (b): Complex cellular geometry to achieve negative Poisson's ratio. (c): Optimized foam with planned stiffness.

Despite offering design freedom, 3D printing technologies have their own limitations as well. The relative densities of 3D printed cellular structures are not able to match those manufactured conventionally due to the minimum feature size limits each printer has [103]. Another possible issue with 3D printed structures is its degradation with time [108]. However, for FDM printed parts at least, their long-term performance are superior [108]. Also, printing of closed-cell structures is limited to certain printers due to the need of support materials for most overhanging structures.

2.6 POLYJET

In this project, the AM technique in focus is Polyjet 3D printing. Polyjet is an AM technique which uses a liquid photopolymer as the building material. As shown in Figure 2, the polyjet print head dispenses liquid photopolymer according to the CAD file sliced layer dimensions and shape. Ultraviolet radiation then floods the build chamber to cure the photopolymer and thus solidifying it. The process is then repeated layer by layer until the part is completed [24]. There are various polyjet 3D printers available in the market and most of these printers are capable of multi-material printing. For example, the Connex printer series developed by Objet (now Stratasys), is capable of mixing photopolymer resins to produce a DM with new mechanical properties [109]. There are a wide variety of resins available ranging from rigid plastic type (Vero Series) to rubbery elastomer type (Tango Series) to high temperature polymers and biocompatible polymers [110].

The mechanical properties of polyjet printed parts can be affected by various process parameters which includes build orientation [109, 111, 112] and distance between parts on the build tray [111]. Due to the anisotropy of polyjet printed parts, it is recommended that the parts critical load direction should be aligned with the x-axis of the build tray [112]. Parts with minimal distance between them are also stronger as compared to those which are further apart, as shown in Figure 2-26 [111].

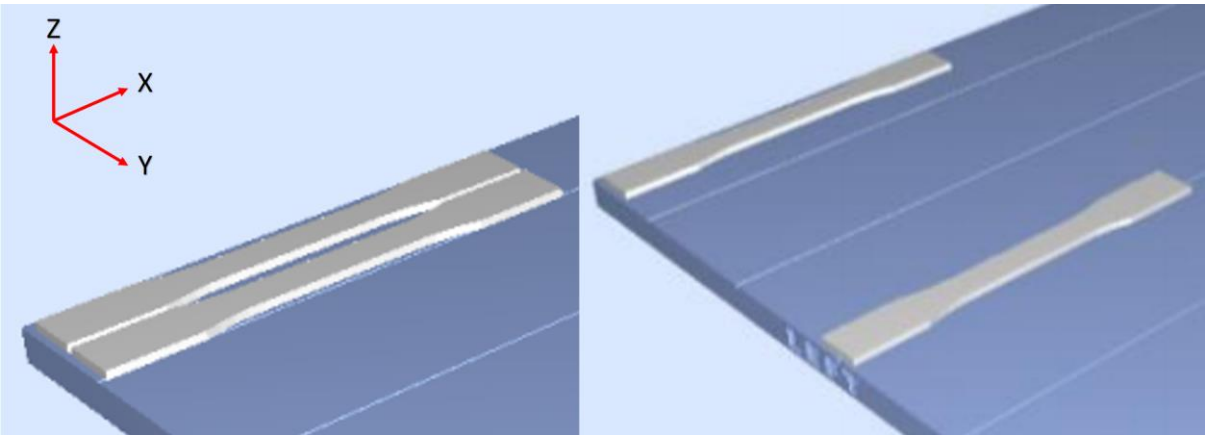

Figure 2-26: Tight spacing vs far spacing [111]. Parts will perform better if their critical load direction is aligned with the x-axis of the build tray.

Polyjet printed parts are also known to be time dependent i.e. their mechanical properties changes with time [113, 114]. Under constant loading conditions, significant stress relaxation was observed [113]. Parts however becomes stronger and stiffer when left in a dark and dry environment longer [114]. Polyjet printed parts are also observed to experienced shrinkage as it goes through photopolymerization [115]. The degree of shrinkage is known to be affected by the intensity of the light source and the geometry of the part [116].

In the field of dentistry, the geometry of the photopolymerized part is quantified by the configuration factor or c-factor [116]. With the aid of Figure 2-27, c-factor is obtained by calculating the ratio of the bonded (green face) to the non-bonded area (grey faces). Generally, a lower c-factor means more free area which allows the resin to remain gel-like, with low elastic modulus (pre-gel), longer thus allowing the polymer molecules to adjust accordingly hence relieving residual stress [116] and therefore, less part distortion.

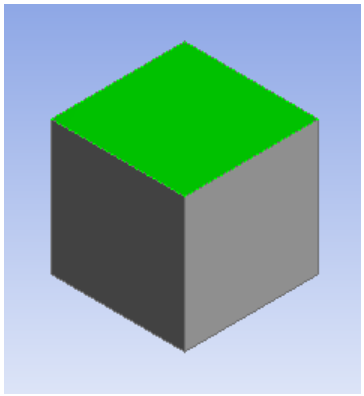

Figure 2-27: C-factor calculation for a unit cube

To produce a polymeric cellular structure with 3D printing, polyjet printing is one of the more suitable processes. Polyjet offers multi-material printing which allows the mixing of polymer resins of various type to produce digital polymers [109, 114]. One polyjet printer can therefore print cellular structures with polymers of various composition in the same print with no added cost. The water-soluble support material used is easily removed without damaging any thin struts or cellular walls [117].

2.7 SUMMARY

Advancements in 3D printing methods enables the fabrication of cellular structures of almost any microstructural design. Current structure properties heavily depend on the relative density and properties of solid materials. Both these parameters will directly affect the net weight of the structure. Ideally, with greater design freedom by 3D printing, a new cellular structure design where its mechanical properties are independent of its weight would greatly benefit many fields.

The network of cells in conventional cellular structures are tessellations of unit cells i.e. cells of similar shapes are repeated and tiled together to completely cover a plane or 3D space (Figures 1-2, 2-2, 2-3, 2-4, 2-10, 2-25 and 2-26). For examples, a hexagonal honeycomb is a tessellation of hexagonal cells. The reason behind such design is partly due to conventional fabrication methods.

Selection of cushioning structures requires cushioning curves (Figures 2-19 and 2-20). Conventional method of producing cushioning curves is very costly and time consuming. Many samples and dynamic testing are required to obtain a comprehensive set of curves. A method was suggested whereby the cushioning curves for various foam thickness and drop-height can be obtained from a single static compression stress-strain curve [87]. This method can potentially make cushioning selection a more straightforward and efficient process.

CHAPTER 3 - MATERIALS, TESTING AND CHARACTERIZATION METHODS

This chapter presents the material used in the research. Methods of testing the materials and 3D printed cellular structures are also presented in this chapter. Lastly, method of characterization of the cellular structures is described.

3.1 MATERIALS

The polyjet printer used is the Objet500 Connex3 which is capable of printing digital materials (DM) made up of three different polymer resins. The resins that were used during the course of this research were VeroClear^{TM}, TangoPlus^{TM} and TangoBlack^{TM}. The Vero^{TM} family of resins are a range of rigid polymers with similar properties but different colours. The Tango^{TM} family of resins are a range of rubber-like materials with different colour and properties.

VeroClear^{TM} and TangoPlus^{TM} are both transparent while TangoBlack^{TM}, as the name suggest, is a black rubber-like material. Additionally, despite both TangoPlus^{TM} and TangoBlack^{TM} being rubber-like materials, TangoBlack^{TM} is harder and less stretchable. The properties of these three materials as specified by Stratasys is presented in Table 3-1. There no stiffness data of the rubber-like materials provided by Stratasys.

Table 3-1: Properties of materials involved as specified by Stratasys [110]

Properties / **Material**	**Tensile Strength (MPa)**	**Elongation at break (%)**	**Elastic Modulus (MPa)**
VeroClear™	50 – 65	10 – 25	2000 – 3000
TangoPlus™	0.8 – 1.5	170 – 220	No data
TangoBlack™	1.8 – 2.4	45 – 55	No data

As mentioned earlier, the Objet500 Connex3 printer is capable of printing DM made up of up to three resins. Mixing two different resins of varying composition will result in a range of DM with varying properties. For this research, it is advantages to have DM made up of VeroClear™ and TangoPlus™/TangoBlack™ as it provides a range of rubber-like materials from very hard to soft. As shown in Table 3-2, Stratasys provides the expected properties of the various DM when mixing VeroClear™ with TangoPlus™ at various compositions. These compositions are however, not revealed.

Table 3-2: Properties of DM made up of VeroClear™ and TangoPlus™ [110]. 05 – DM to 30 – DM are rigid plastics while 40 – DM to 95 – DM are rubber-like materials.

Properties / **XX-DM**	**Tensile Strength (MPa)**	**Elongation at break (%)**	**Elastic Modulus (MPa)**
05 – DM	40 – 60	15 – 25	1700 – 2300
10 – DM			
15 – DM			
20 - DM			
25 – DM	35 – 45	20 – 30	1400 – 2000
30 – DM	29 – 38	25 – 35	1100 – 1700
40 – DM	1.3 – 1.8	110 – 130	No data
50 – DM	1.9 – 3.0	95 – 110	No data
60 – DM	2.5 – 4.0	75 – 85	No data
70 – DM	3.5 – 5.0	65 – 80	No data
85 – DM	5.0 – 7.0	55 – 65	No data
95 – DM	8.5 – 10.0	35 – 45	No data

The number labels for each digital material does not represent the polymeric composition of the resins. From 40 – DM to 95 – DM, the numbers approximately represent their shore hardness (A) values. For 05 – DM to 30 – DM, it is unclear what these numbers represent. Furthermore, the density values are not provided either, hence

from the data provided alone, it is not possible to ascertain the polymeric composition of each DM. Additionally, without the voxel technology, which is an add-on feature that allow users to directly control the polymeric compositions of DM, drawing a relationship between the polymeric compositions and the resulting properties is not possible. In this study, a method was however developed to overcome this and will be presented Section 3.2.1.

Apart from 3D printable polymer resins, Polyethylene (PE) foams of density 1.7 pounds/ft^3 (pcf) of 2-inch thickness were used for in both static compression and dynamic compression tests. The specimens were cut from a 1 m by 2 m by 1-inch foam sheet.

3.2 MATERIAL TESTING

The various tests involved during the conduct of this research are listed in this section. A specimen preparation method which allows the control of the polymeric composition of DM is presented as well.

3.2.1 Layering

As mentioned earlier in Section 3.1, controlling DM polymeric composition is an issue. The information on polymeric compositions is important in order to derive a relationship with the resulting properties. Layering is a possible method to have control over the polymeric composition of DM.

Layering is basically the manual digital slicing of the part's CAD file using the CAD software itself. The layers are then assembled together before being converted into the stereolithography file format (.stl). This allows the assignment of specific resins to individual layers. The ordering of these layers needs to be accounted for as well to ensure homogeneity. Most importantly, the slicing direction must be in the same direction of the principal load.

An example for the application of the layering method is for the conduct of tensile tests on 3D printed specimens made up of 50% TangoPlus™ and 50% VeroClear™. Dumbbell-shaped specimens with dimensions and shape as shown in Figure 3-1 are required for the conduct of the test. For any layering of parts, the part geometry, dimensions and loading direction should be taken note of.

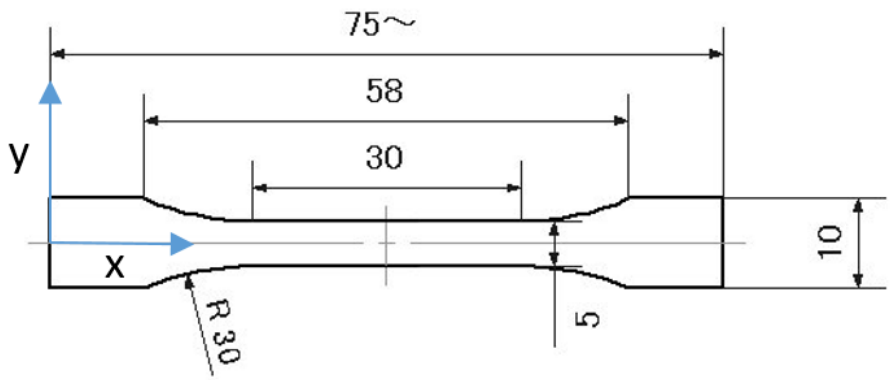

Figure 3-1: ISO 527-2 Type 1BA dumbbell [118]

Given that the dumbbell geometry is two-dimensional (2D) with its thickness in the third dimension, layering can be performed. For homogeneity, each layer should be identical to the other limiting the technique to 2D solids. For the dumbbell as shown in Figure 30, the loading direction will be along the x-axis, hence layering should also be done along the x-axis i.e. stacking of layers along the z-axis. Given the dumbbell thickness of 2 mm and the printer's minimum feature size of 30 µm, a layer thickness of 40 µm will be sufficient to have a dumbbell made up of 50 identical layers. This is as illustrated in Figure 3-2. With 50 layers, polymeric compositions with a minimum increment of 2% can be controlled. Obtaining a 50:50 polymeric composition of TangoPlus™ and VeroClear™ can be achieved by alternating them.

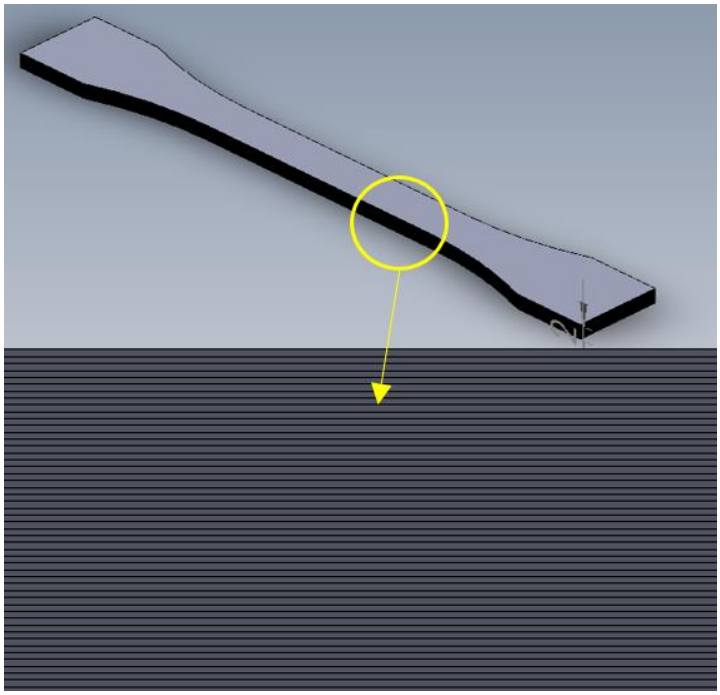

Figure 3-2: ISO 527 specimen sliced into 50 layers

Layering can also be done on cylindrical specimens for compression tests. As long as the part is 2D, layering can be performed. However, for 3D parts such as cellular structures, layering cannot be done without jeopardising the parts homogeneity for both material and load distribution in at least one dimension's axis. Hence, the layering method proposed can instead be used to match the properties of specimens of known polymeric composition to those found in Table 3-2.

3.2.2 Tensile testing of solid materials

The material types to be tested are rigid plastic type (VeroClear^{TM}), rubber-like (TangoPlus^{TM} and TangoBlack^{TM}) and digital polymers made up of both. Testing of VeroClear^{TM} and TangoPlus^{TM}/TangoBlack^{TM} specimens are according to the ISO 527 (Plastics – Determination of tensile properties) [118] and ISO 37 (Rubber, vulcanized or thermoplastic – Determination of tensile stress-strain properties) [119] standards respectively.

Table 3-3 summarizes the recommended test parameters for ISO 527 and ISO 37 standards. Due to limited resins available, smaller specimens, type 1BA (ISO 527) and type 2 (ISO 37) dumbbells were used. Their dimensions are shown in Figure 3-3 and 3-4 respectively. SolidWorks was used to prepare the CAD files of these specimens.

Table 3-3: Test parameters

	ISO 527 [118]	**ISO 37 [119]**
Polymer Type	Plastics	Rubbers
Loading Rate	0.125-500 mm/min	500 mm/min (type 1-2 dumb-bells)
Conditioning **(standard temp.)** *Note: conditioning refers to acclimatizing of the test specimens to the tests environment*	≥ 16 hrs, 23°C, 50% relative humidity	16 hrs (between vulcanization and testing). ≥ 3hrs (test environment conditioning)

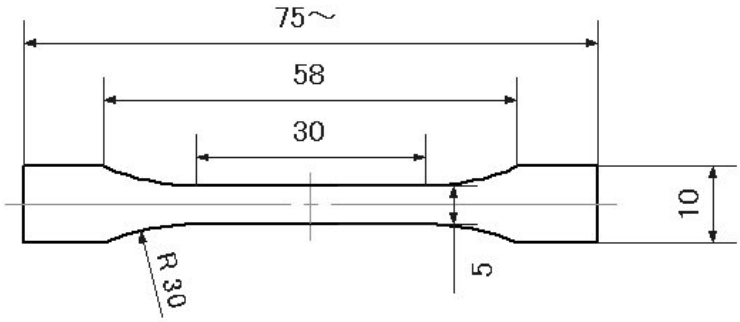

Figure 3-3: ISO 527 Type 1BA specimen

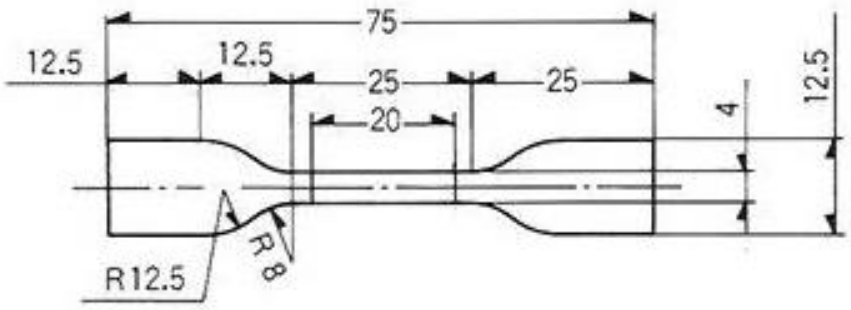

Figure 3-4: ISO 37 Type 2 specimen

For each test, a minimum of three specimens were subjected to tensile extension using an Instron Universal Testing Machine 5560, 50 kN loadcell. The loading rates for the ISO 527 and ISO 37 tests were set at 10 mm/min and 100 mm/min respectively. An extensometer was used to measure the elongation up till 2% strain to obtain a more accurate elastic portion. A loading rate of 500 mm/min could not be achieved by the Instron machine as recommended by the ISO 37 standard, therefore the highest loading rate achievable for accurate testing of 100 mm/min was used.

Testing of digital polymers is not as straightforward. As seen in Table 3-3 and Figures 3-3 and 3-4, the loading rates and specimen geometry are different. Therefore, for digital polymers which are a mixture of rigid plastic and rubber, the test standard that they should be subjected to is unclear (e.g. 50:50 polymeric composition of VeroClear^{TM}:TangoPlus^{TM}).

The tests were conducted to determine which specimen type would yield a more accurate and repeatable result for 50:50 digital polymers (refer to APPENDIX A). ISO 527 specimens produce more accurate tensile testing results and were less likely to experience warpages. As seen in Figure 3-5, ISO 37 specimens experienced significant warping which suggests the presence of residual stresses in the ISO 37 specimens due to photopolymerization shrinkage. This also suggests that the geometry of 3D printed polymers influence the degree of shrinkage. To confirm this, c-factors (mentioned in Section 2.6) of the respective specimen type are calculated to quantify their likelihood of photopolymerization shrinkage. Before the c-factors for the ISO 527 and ISO 37 specimen types were determined, some assumptions were made:

1. The c-factor for the part is calculated based on the individual layer geometry as Polyjet printing is a layer-by-layer process.

2. Both the top and bottom surfaces are considered as bonded surfaces as they are bonded to the neighbouring top and bottom layers and the time it takes to deposit the next layer is insignificant.
3. The only free surfaces are the surfaces making up the perimeter of the layer as these remains unbonded throughout the polyjet printing process.

With these assumptions, it was found that the c-factor for ISO 37 specimen type is 117.6 and that for ISO 527 is 98.6. This is consistent with the observation of ISO 37 specimens experiencing warpages due to higher residual stress within the specimens. More comparison tests are however required for other compositions to determine the minimum composition of rubber required for ISO 37 standards to apply. At the moment of writing, only 50:50 composition was tested.

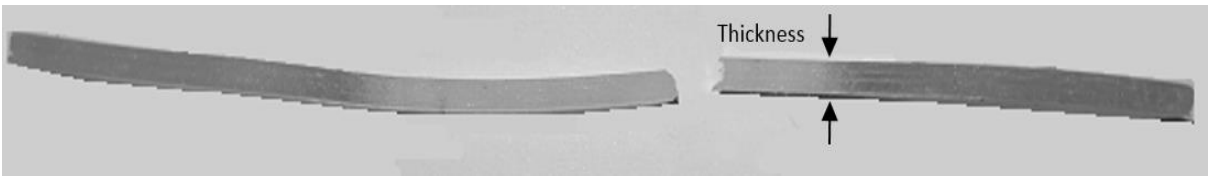

Figure 3-5: Post failure warping – xz plane (ISO 37)

3.2.3 Testing of cellular structures

The cellular structures involved in this research includes both 2D and 3D structures i.e. honeycombs and foams. Given that the objective of this research is to optimize cellular structures for cushioning purposes, the tests are therefore static and dynamic compression of the honeycombs (in-plane) and PE foams. ISO 3386 and ISO 4651 test standards were applied for testing of the 3D printed honeycombs and PE foams for static and dynamic compression tests respectively. The Instron Universal Testing Machine (Figure 3-6) and Cadex Twin Wire 1000 kg Machine (Figure 3-7) were used for the static and dynamic compression tests respectively.

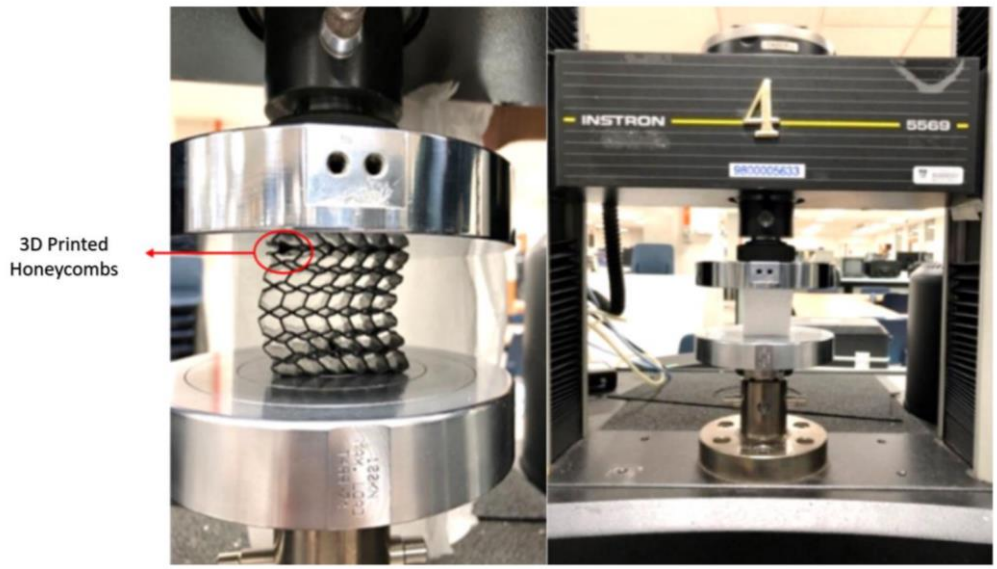

Figure 3-6: Static compression with Instron Universal Testing machine

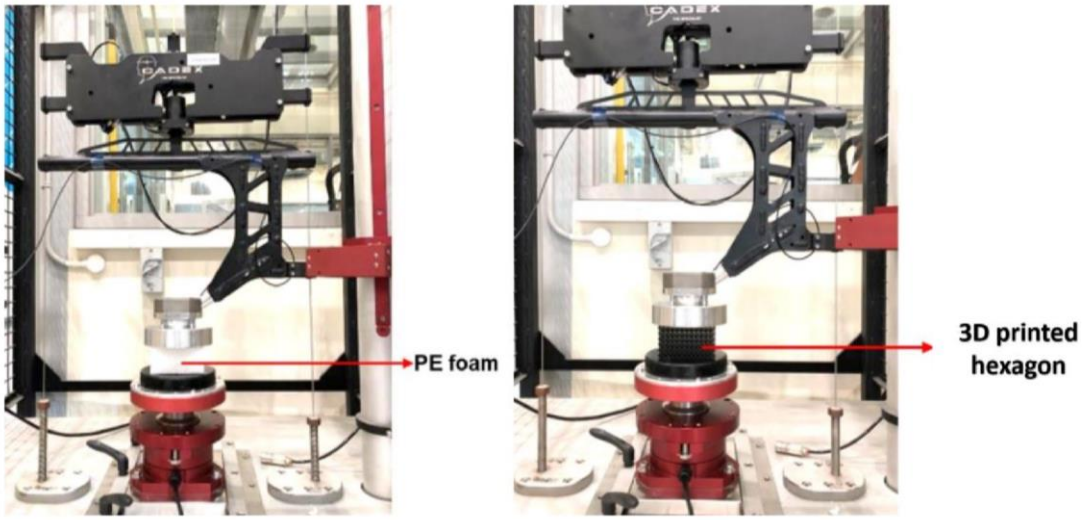

Figure 3-7: Drop-test with Cadex Twin Wire 1000 kg Machine

As mentioned in Section 1.2, polyjet printers are capable of printing thin walls. Theoretically, based on the printer's specification, the smallest feature printable is 16 µm or 0.016 mm. This is provided that the feature is built vertically. However, this building orientation is often avoided due to the need for support material. Before the soluble support material was available, the support material had to be removed physically via water jet which may damage structures which are very thin. For features built along other directions, the theoretical minimum feature size is 200 µm or 0.2 mm.

This is however dependent on the geometry and material. It is easier to achieve the theoretical minimum feature size with rigid materials such as VeroClear^{TM}. However, it is very common to obtain incomplete (Figure 3-6) or warped (Figure 3-7) walls which are a lot thicker than the theoretical minimum feature size of 0.2 mm. The higher the walls, the more likely it is for the walls to be incomplete or warped. 3D printing tips found online recommended a minimum thickness of 0.6 mm to 2 mm depending on the resin type [120, 121].

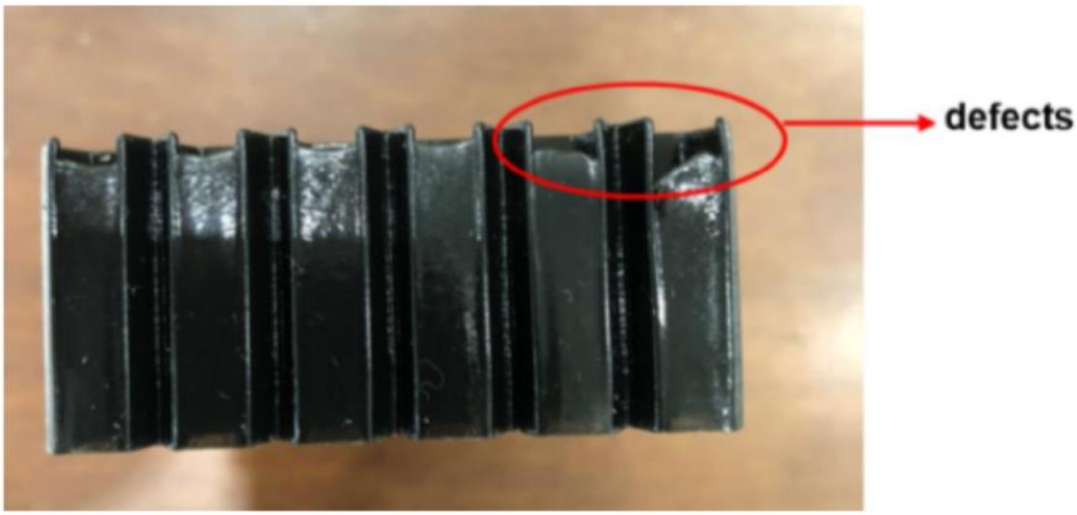

Figure 3-8: Incomplete building of thin walls during Polyjet printing process

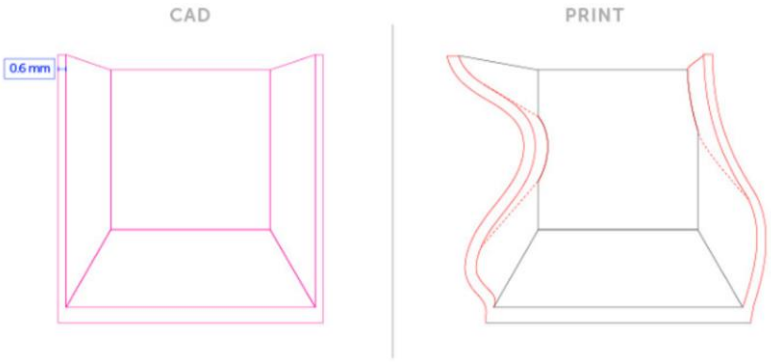

Figure 3-9: Warping of thin walls during polyjet printing process

As such, the honeycomb samples were prepared in the following way with justifications:

- The printing orientation is as illustrated in Figure 3-10 and 3-11. This is to eliminate the need for support material.
- The width (z-axis) is fixed at 30 mm to minimise the chances of having incomplete or deformed cell walls. Furthermore, a 30 mm width would prevent buckling of the structure when it is subjected to compressive loads.

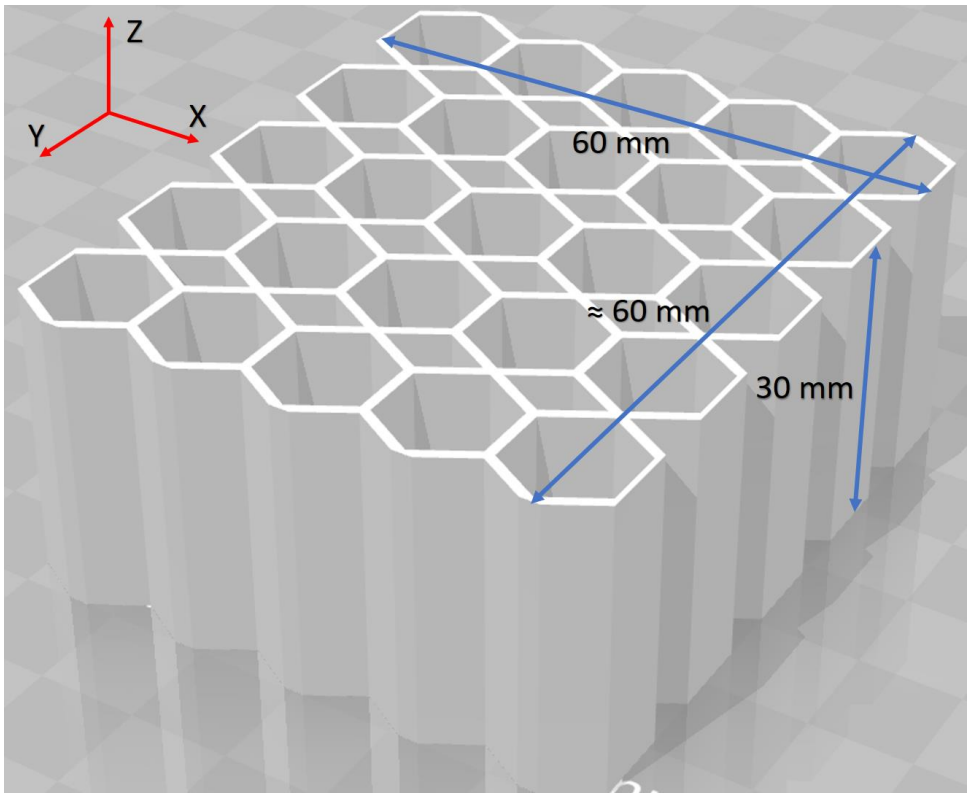

Figure 3-10: Build orientation of honeycomb samples

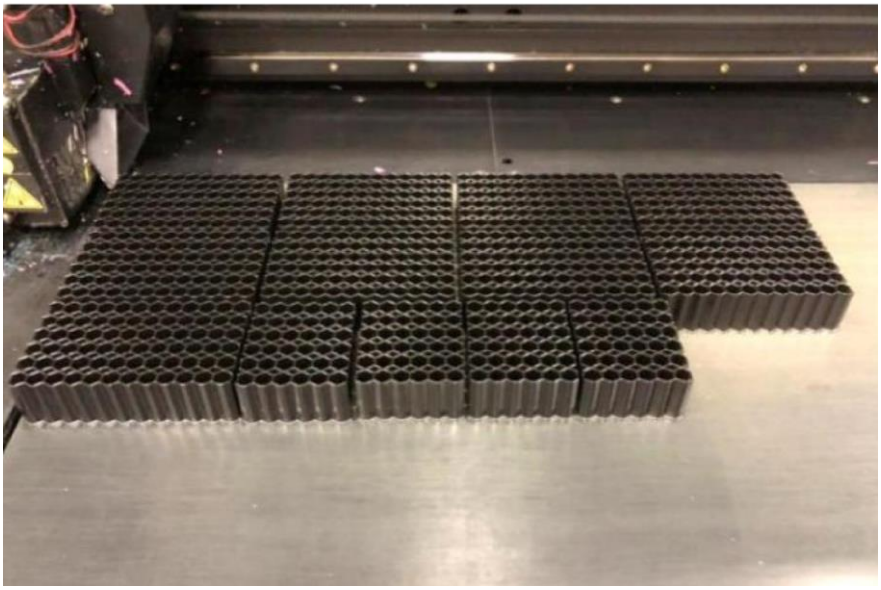

Figure 3-11: 3D Printing of honeycomb samples

The compression loading rate was set at 10 mm/min in the y and z direction (Figure 3-10). For out-of-plane compression test, the samples were prepared in the same way with the same dimensions. The strain rate used was also the same with the compression direction along the z-axis (Figure 3-10).

3.2.4 Preliminary results

Layered vs non-layered

The layering method was presented in Section 3.2.1 to enable users control over the polymeric composition of digital polymers. In order to establish the method as a viable method, the test results of layered samples should not differ significantly from non-layered specimens. Therefore, the first set of tests was the tensile testing of layered and non-layered VeroClear^{TM} specimens. The tensile tests were conducted in two batches (both with 16 hours of conditioning post-printing); batch 1 – immediately after conditioning and batch 2 – after 1 week. Figures 3-12 and 3-13 displays the stress-strain curves for both batches.

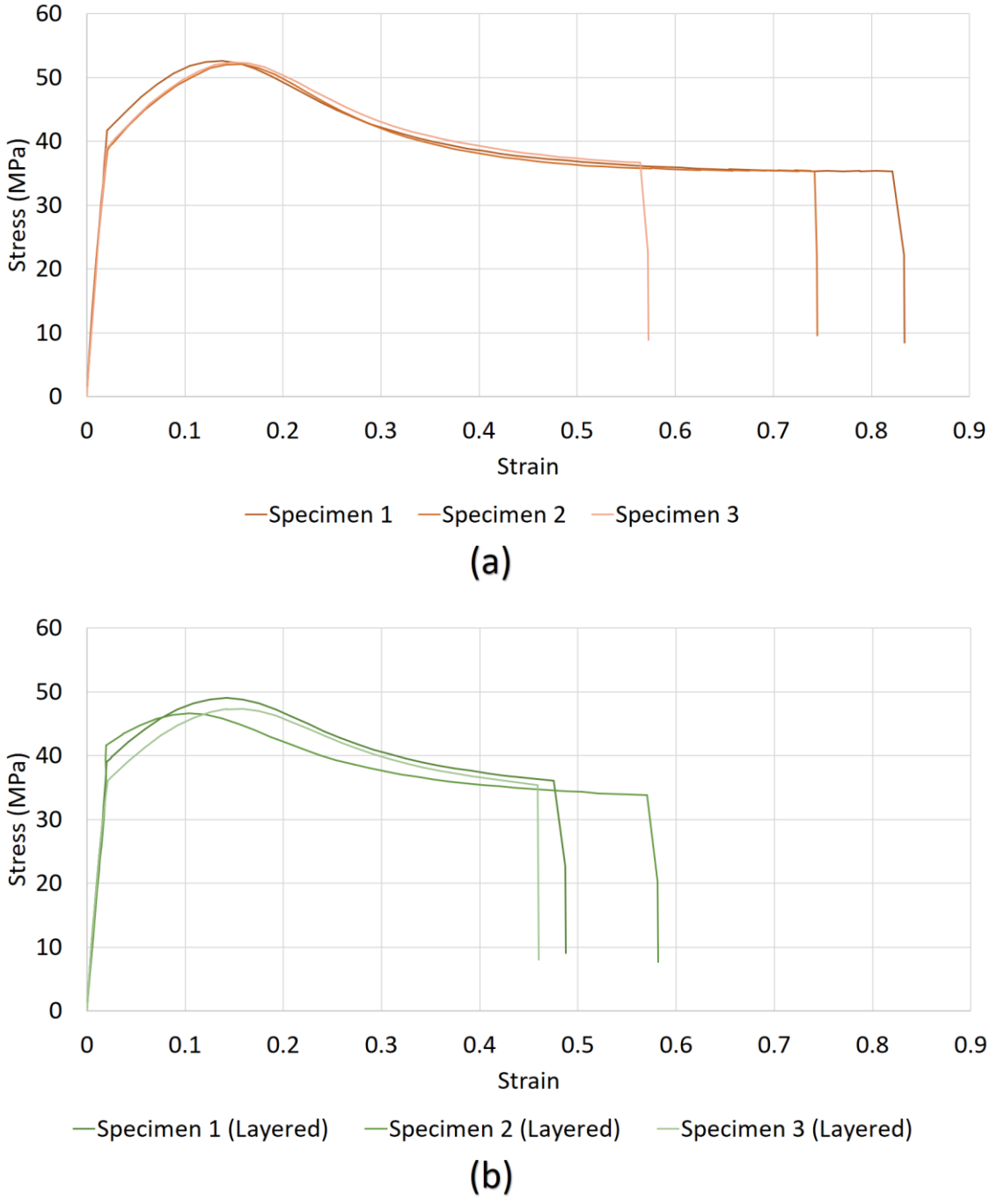

Figure 3-12: Stress-strain curves of (a) non-layered specimens and (b) layered specimens immediate after conditioning (VeroClear specimens).

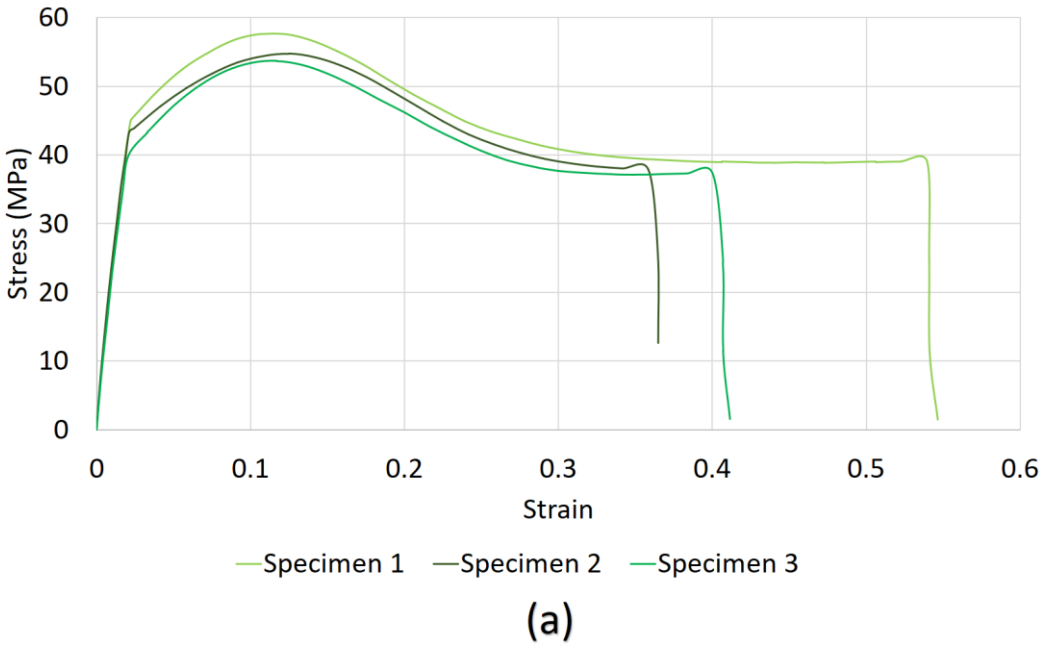

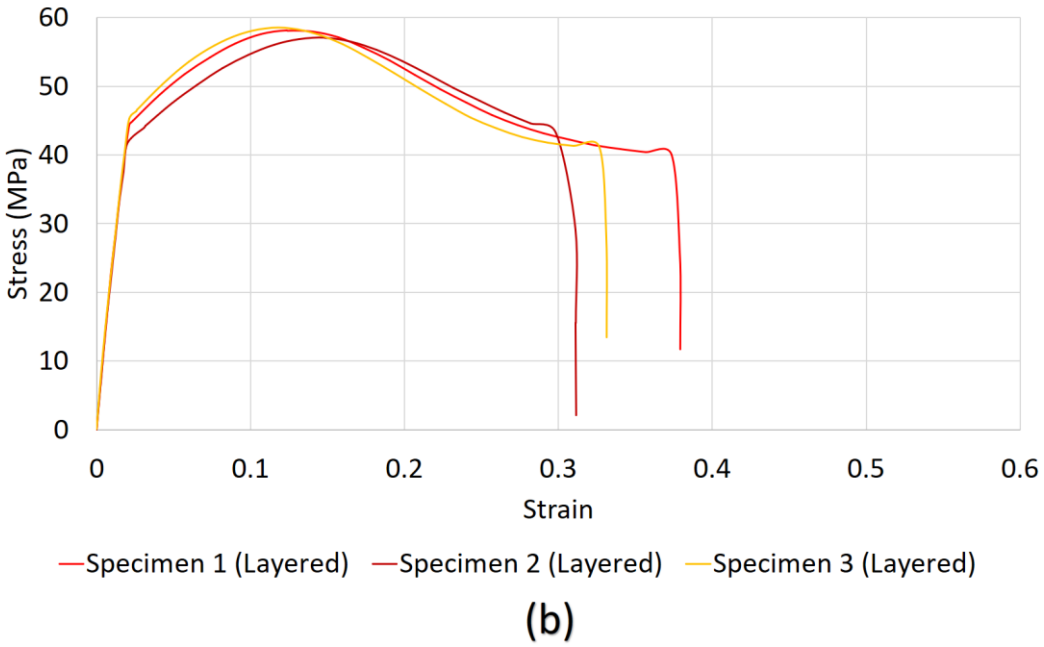

Figure 3-13: Stress-strain curves of (a) non-layered specimens and (b) layered specimens 1 week after conditioning (VeroClear specimens).

The stress-strain response observed in Figure 3-12 shows that the ultimate tensile strength (UTS) for the layered specimens has a lower mean of 47.2 MPa as compared to a mean of 52.4 MPa for the non-layered specimens. Likewise, the mean elastic modulus (***E***) for the layered specimens was lower at 1.76 GPa as compared to 1.95 GPa for the non-layered specimens. Two factor t-test were conducted to confirm that the of

strength due to layering of specimens were statistically significant ($p < 0.05$). The differences between the measure elastic moduli were however statistically insignificant. However, when the specimens were conditioned for an additional week (Figure 3-13), the mean UTS and ***E*** for the layered and non-layered specimens are 57.9 MPa and 55.3 MPa, 2.16 GPa and 2.08 GPa respectively. Although the layered specimens are now found to be stiffer and stronger, performing ANOVA and t-test concludes that these differences are statically insignificant ($p > 0.05$).

Therefore, in order to accept layering as an alternative method to control the composition of digital polymers, the specimens must be conditioned for an additional week. This is to ensure that the differences in the mechanical response when compared to non-layered specimens are statically insignificant. It is also worth to note that the increase in UTS and ***E*** of the layered specimens due to longer conditioning time is statically significant. The same cannot be said for the non-layered specimens. This may imply a time dependency on the mechanical properties of polyjet printed parts.

Summary of tensile test results

Tensile testing was conducted on 3D printed specimens with four different materials; VeroClear™, TangoPlus™, TangoBlack™ and a combination of VeroClear™ and TangoPlus™ with a 50:50 polymeric composition. The results of the various tests are summarized in Table 3-4.

Table 3-4: Tabulated UTS and E of the various tests

Specimen Type	Mean	
	UTS (MPa)	E (MPa)
VeroClear™	53.838	2014.193
TangoPlus™	0.723	$E_{\varepsilon=1} = 0.172$ $E_{\varepsilon=2} = 0.116$ $E_{\varepsilon=3} = 0.114$
TangoBlack™	1.298	$E_{\varepsilon=0.5} = 1.980$
VeroClear™ + TangoPlus™ (50:50)	8.300	391.487

The elastic modulus for TangoBlack^{TM} specimens could not be measured at 100% elongation as all the specimens failed at less than 80% elongation. The measured UTS for both TangoPlus^{TM} and TangoBlack^{TM} specimens are lower than the range of UTS specified by Stratasys (TangoPlus^{TM}: 0.8 – 1.5 MPa, TangoBlack^{TM}: 1.8 – 2.4 MPa). Referring to Table 3, a 50:50 polymeric composition of VeroClear^{TM} and TangoPlus^{TM} is likely the composition for 95 – DM (specified UTS range 8.5 – 10.0 MPa).

3.3 CHARACTERIZATION METHODS

This section discusses the new methods developed to characterize the material properties obtained from stress-strain data for this research.

3.3.1 Material yield strain identification using energy absorption

Yield stress (σ_y) or strain (ε_y) is an important property of all engineering materials as it allows engineers to safely select the appropriate material for an application. Yield strain (or yield point) is determined with an engineering stress-strain curve [122]. As shown in Figure 3-14, some materials have distinguishable yield point. This is normally in the form of an abrupt change from elastic to plastic deformation.

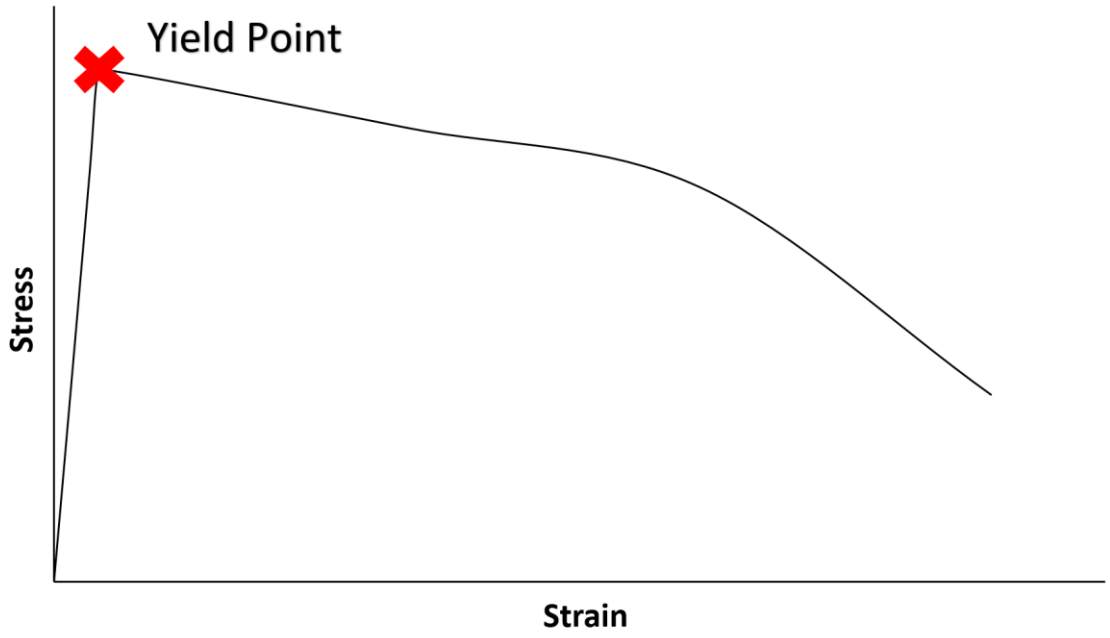

Figure 3-14: Material with distinct yield point

For most materials, the transition from elastic to plastic deformation is smooth, resulting in an indistinctive yield point. For such cases, apart from current methods [123-125], an energy absorption method was developed and adopted. This is to improve the characterization accuracy of materials' yield stress. The technique is to transform the

experimental stress-strain curve into an idealized linearly elastic – perfectly plastic (LEPP) stress-strain curve (Figure 3-15). The yield point is then the "turning point" of the LEPP model.

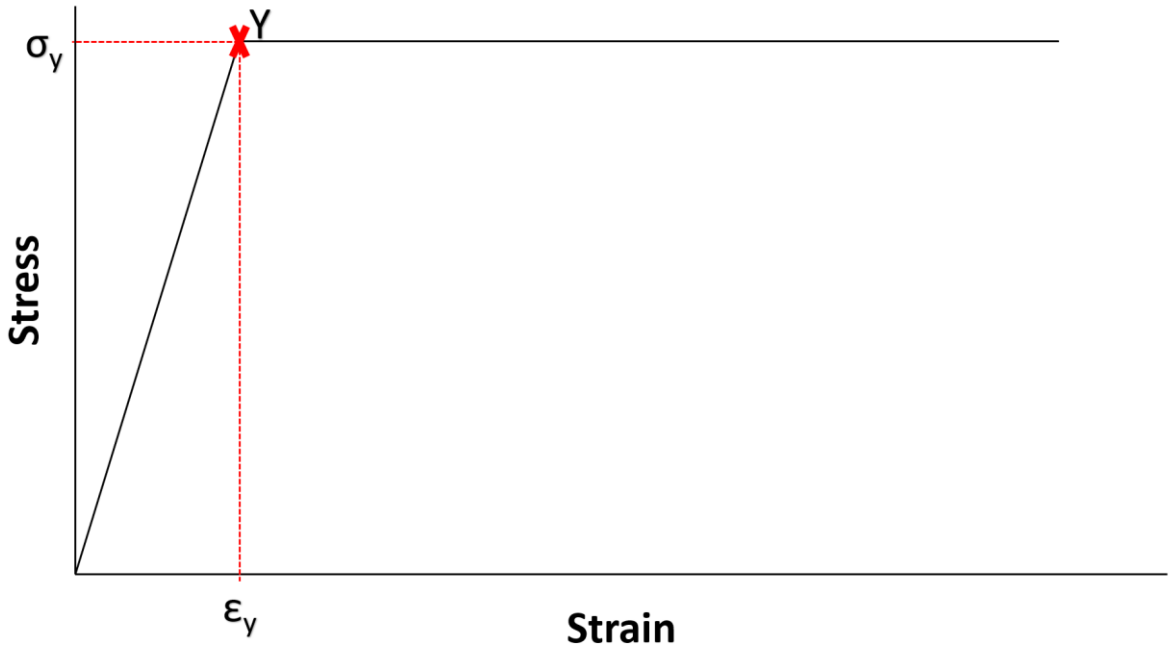

Figure 3-15: Idealised linearly elastic - perfectly plastic model

The detailed method is described below:

1. Identify 1st peak stress ($\boldsymbol{\sigma_{pk}}$).
2. Integrate the experimental stress-strain curve up till the strain value $\boldsymbol{\varepsilon_{pk}}$ corresponding to $\boldsymbol{\sigma_{pk}}$ to determine amount of energy absorbed ($\boldsymbol{W_{pk}}$) as in Figure 3-16.

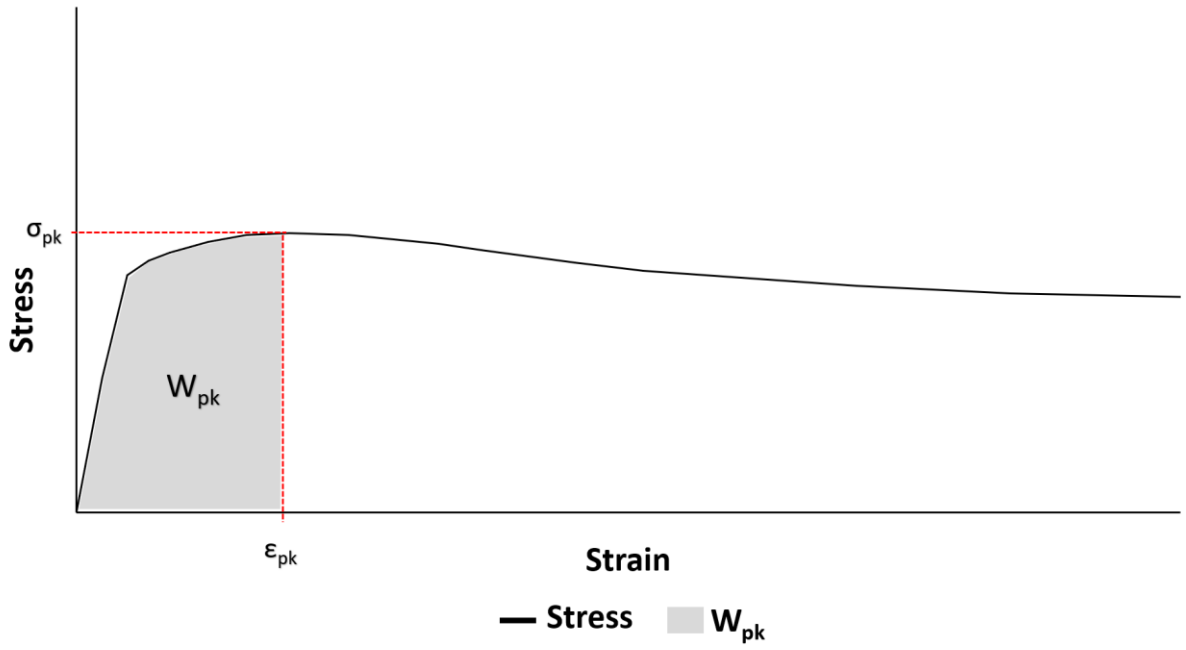

Figure 3-16: Identifying peak stress and corresponding strain

3. Assume yield strain (ε_y) can be anywhere between $\varepsilon=0$ to $\varepsilon=\varepsilon_{pk}$.
4. Select 1st strain value (ε_1) (Figure 3-17).
5. Convert W_{pk} into LEPP model (Figure 3-17). LEPP area, W_{pk}, can be rearranged to determine σ_1' as shown:

$$W_{pk} = \frac{1}{2} \times \left[\varepsilon_{pk} + \left(\varepsilon_{pk} - \varepsilon_1\right)\right] \times \sigma_1'$$

$$\therefore \sigma_1' = \frac{2W_{pk}}{\left[2\varepsilon_{pk} - \varepsilon_1\right]} \quad (21)$$

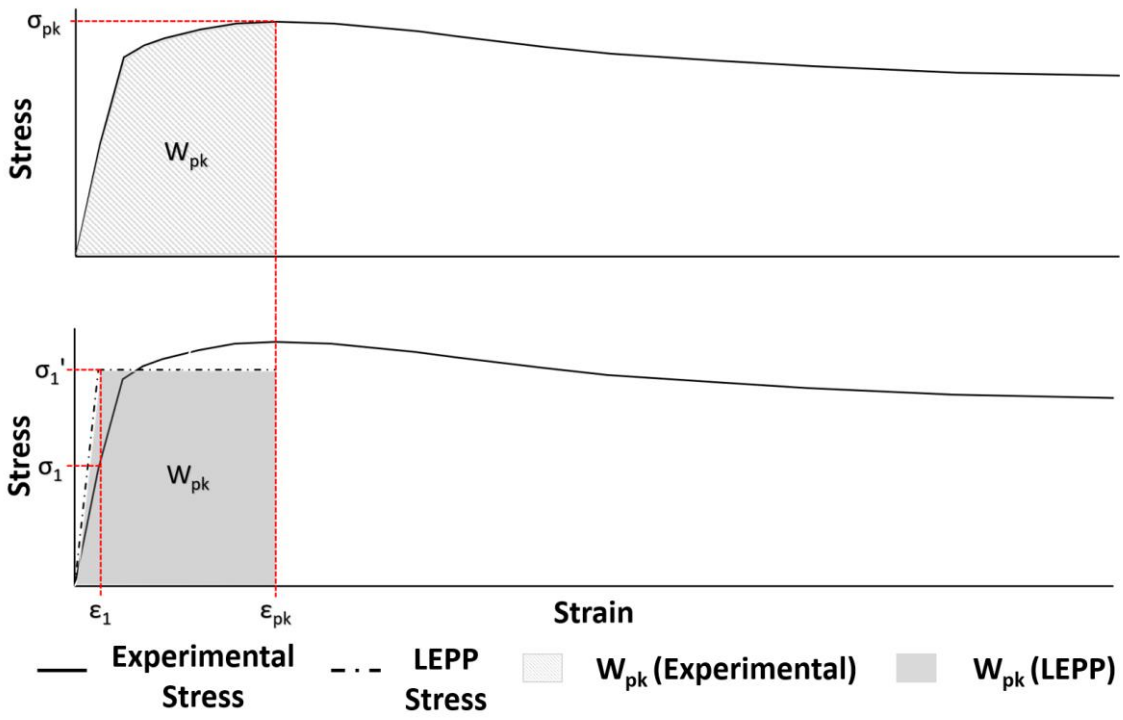

Figure 3-17: Converting stress-strain curve up till ε_{pk} to LEPP model based on amount of energy absorbed

6. The predicted modulus (E_1') for the LEPP model can then be calculated (Equation 22) and the modulus of the actual stress-strain curve (E_1) can be estimated (Equation 23) as shown in Figure 3-18.

$$E_1' = \frac{\sigma_1'}{\varepsilon_1} \tag{22}$$

$$E_1 = \frac{\sigma_1 - \sigma_0}{\varepsilon_1 - \varepsilon_0} \tag{23}$$

where σ_0 and ε_0 are the stress and strain value at the origin which are normally ≈ 0, and σ_1 is the experimental yield stress value on the stress-strain curve corresponding to ε_1.

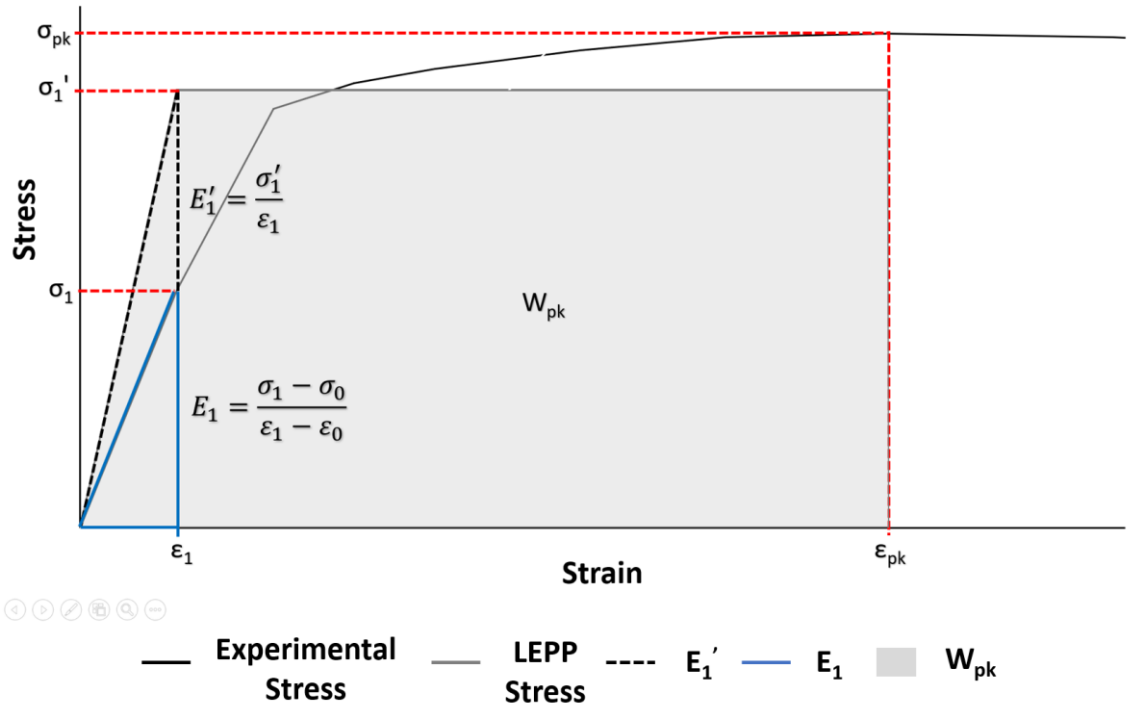

Figure 3-18: Calculating E_1' and E_1. (Zoomed in on Figures 3-13 and 3-14)

7. The difference in modulus (ΔE) can be calculated with Equation 23.

$$\Delta E = \left| \frac{E_1 - E_1'}{E_1} \right| \tag{24}$$

8. Steps 4 to 7 are repeated for all strain values up to ε_{pk}. ΔE is plotted together with the original stress-strain curve as shown in Figure 3-19.

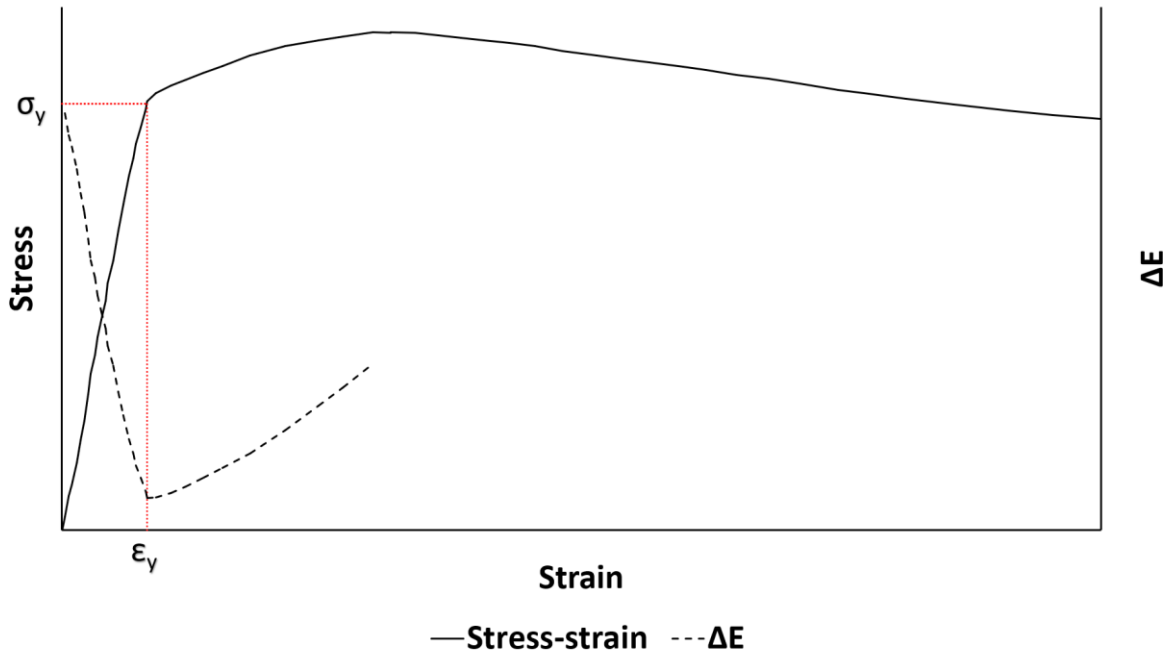

Figure 3-19: Identifying yield strain, ε_y, at minimum ΔE

9. The minimal ΔE corresponds to the $\boldsymbol{\varepsilon_y}$ and respective $\boldsymbol{\sigma_y}$. Therefore, the energy absorption method yield point criterion is defined as:

$$\frac{\partial}{\partial \varepsilon}(\Delta E) = 0 \tag{25}$$

3.3.2 Characterizing static stress-strain properties of cellular structures

The compressive properties of cellular structures are characterized by its linear modulus ($\boldsymbol{E^*}$), plateau stress ($\boldsymbol{\sigma_p}$) and densification strain ($\boldsymbol{\varepsilon_d}$). In Section 2.1.4, a good way to identify $\boldsymbol{\sigma_p}$ was mentioned. This method first calculates the amount of energy absorbs during the plateau phase and divide it by strain range from the onset of plateau to the onset of densification [50]. This is as defined by Equation 26.

$$\sigma_p = \frac{\int_{\varepsilon_p}^{\varepsilon_d} \sigma(\varepsilon) d\varepsilon}{\varepsilon_d - \varepsilon_p} \tag{26}$$

The densification strain can be obtained by locating the strain corresponding to the maximum energy absorbed to strain ratio ($\boldsymbol{W/\sigma}$). The available methods of determining $\boldsymbol{\varepsilon_p}$ are however deemed to be inconsistent. An adjustment to the method as defined by Equation 26 is made to accurately characterize the static compressive properties of cellular structures.

Cellular structures are commonly used for energy absorbing applications up till $\boldsymbol{\varepsilon_d}$. For any cellular structure, there are variations of the linear modulus and plateau stress. However, the energy absorbed by the structure up till $\boldsymbol{\varepsilon_d}$ ($\boldsymbol{W_d}$) is a unique value (Equation 27).

$$W_d = \int_0^{\varepsilon_d} \sigma d\varepsilon \tag{27}$$

The compressive stress-strain response can be idealised as a linearly elastic-perfectly plastic model (Figure 3-20) [50]. Based on this model, an expression can be formulated to equate $\boldsymbol{\varepsilon_p}$, $\boldsymbol{\varepsilon_d}$, $\boldsymbol{E^*}$ and $\boldsymbol{\sigma_p}$ to $\boldsymbol{W_d}$. This is as shown in Equation 28.

$$W_d = \frac{(2\varepsilon_d - \varepsilon_p)\sigma_p}{2} \tag{28}$$

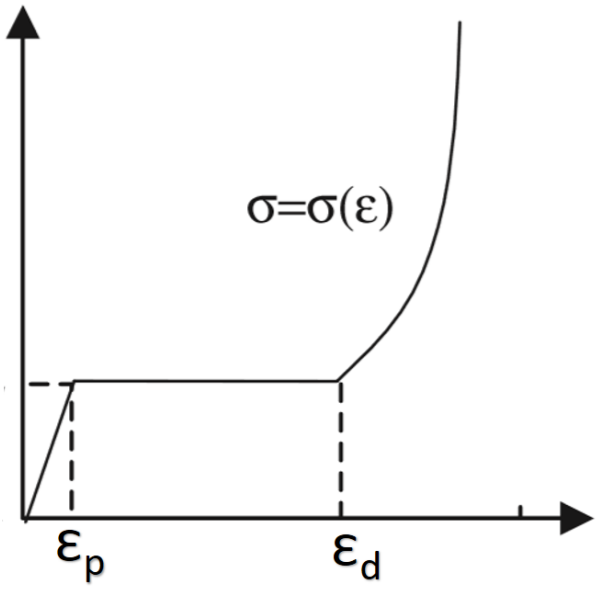

Figure 3-20: Idealised stress-strain curve – linear elastic-perfectly plastic [50]

The first step is to determine $\boldsymbol{\varepsilon_d}$ which is, as mentioned earlier, defined as the strain value corresponding to the maximum energy absorbed to stress ratio. As iterative approach is adopted for both cases where every strain data point from 0 to $\boldsymbol{\varepsilon_d}$ is assumed to be $\boldsymbol{\varepsilon_p}$. With that assumption, Equation 28 can be rearranged to Equation 29 to determine $\boldsymbol{\sigma_p}$ (if the assumed is $\boldsymbol{\varepsilon_p}$ true).

$$\sigma_p = \frac{2W_d}{(2\varepsilon_d - \varepsilon_p)} \tag{29}$$

$\boldsymbol{E^*}$ can then be calculated with Equation 30.

$$E^* = \frac{\sigma_p}{\varepsilon_p} \tag{30}$$

However, this is still part of the iterative process, the value obtained from Equation 30 is compared to the actual $\boldsymbol{E^*}$ (Equation 31).

$$E_e^* = \frac{\sigma_e}{\varepsilon_p} \tag{31}$$

where $\boldsymbol{\sigma_e}$ is the experimental stress value at the assumed $\boldsymbol{\varepsilon_p}$.

The E^* and E_e^* are then compared by calculating their absolute difference (Equation 32). This is repeated for all strain values from 0 to ε_d. The onset of plateau strain is located at the strain value with the lowest ΔE^* as shown in Figure 3-21.

$$\Delta E^* = |E^* - E_e^*| \tag{32}$$

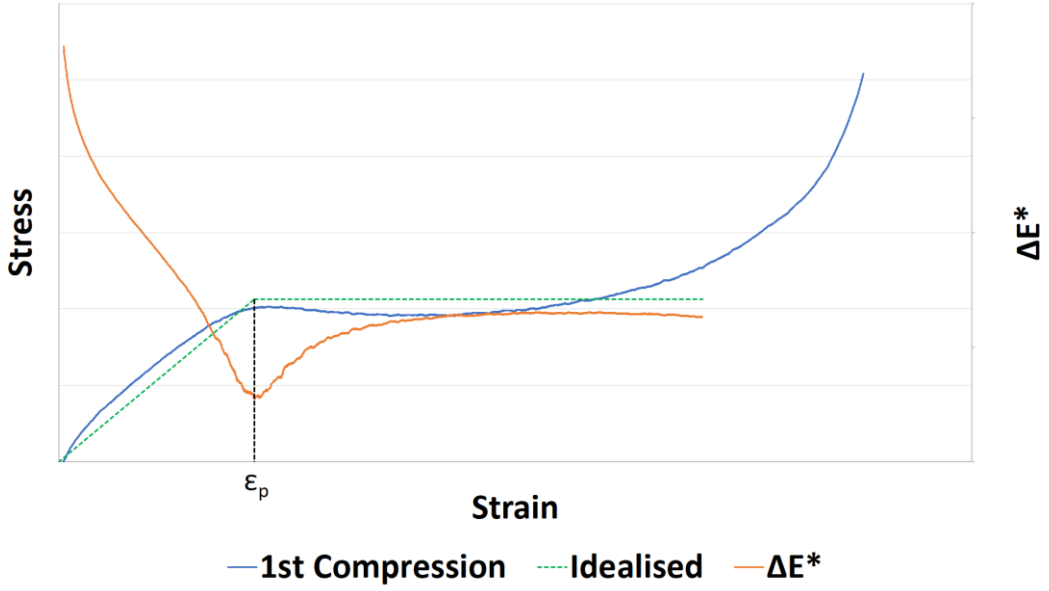

Figure 3-21: Stress-strain curve modelled with linearly elastic-perfectly plastic. Onset of plateau phase located at minimum ΔE^*

Once ε_p is determined, σ_p and E^*can be easily obtained with Equation 29 and 30 respectively. The example in Figure 3-21 used to demonstrate the application of this method suggest a very good curve fit between the idealised and actual curve with an R^2 value of 0.881.

3.4 SUMMARY

The materials involved with this research were presented and the limitations associated with digital polymers were discussed. The layering method is proposed to allow the control over polymeric compositions, but it is also only limited to 2D solids.

The suitability of ISO 527 and ISO 37 specimen types for testing of mix properties digital polymers were investigated. The tensile testing on ISO 527 specimens resulted in higher measured UTS and $\boldsymbol{E}$, and less warping. ISO 527 is therefore deemed to be more suitable for testing of mixed properties digital polymers.

Polyjet printers have limited capabilities in reproducing thin wall structures and steps were taken to maximise it as much as possible. These steps dominate the design the fabrication of honeycomb specimens. A method to accurately identify the compressive mechanical properties of cellular structures is presented. This method idealizes the compressive stress-strain curves of any cellular structure and extracts the important information ($\boldsymbol{E^*}$, $\boldsymbol{\sigma_p}$, $\boldsymbol{\varepsilon_p}$, $\boldsymbol{\varepsilon_d}$) from the idealized curve. The curves have good fit with the experimental curves.

The key findings/information include:

1. Layered specimens must be conditioned longer (≈ 1 week) before conducting any tests.
2. Polyjet printed parts are affected by time (post printing) and shape of part. Shape of Polyet printed part determines the degree of photopolymerization shrinkage. The c-factor may be used to quantify this.

The above requires further work to confirm the findings.

CHAPTER 4 – NOVEL CELLULAR STRUCTURE DESIGN AND NUMERICAL MODELLING

As mentioned in Section 2.1.1, a conventional cellular structure is designed to be filled within a plane (honeycomb) or space (foam) i.e. tessellation of the chosen shape. But due to this nature of design, not all shapes can be used to design a cellular structure. In the case of honeycombs, the cells can either be three-sided (triangles), four-sided (squares/rectangles) or six-sided (hexagons). It is not possible to make honeycombs out of pentagonal or any other polygons. As mentioned in Section 2.4, scaling of the cells influences the stiffness and strength of the structure. However, with conventional design, scaling or refining the cell will not maintain the relative density of the structure. In this section, a novel cellular structure is presented which maximises the scale effect by adopting a new cellular arrangement.

4.1 NEW HONEYCOMB MODEL: POLYGONAL CELLULAR ARRAY

With the greater design freedom provided by 3D printing methods, the honeycomb can be designed such that the unit cells are arranged in a regular cellular array. An analogy to this is like how soldiers form a parade contingent. This arrangement can be seen in Figure 4-1. Any cellular shape can be fitted into the model as seen in Figure 4-2.

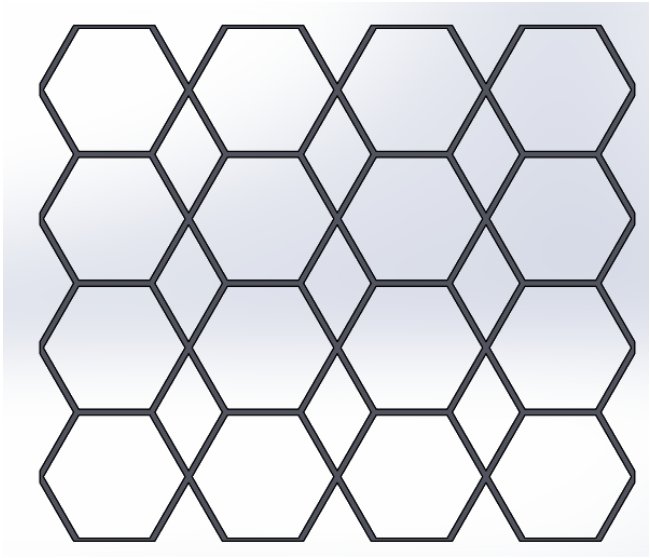

Figure 4-1: Regular Hexagonal Cellular Array

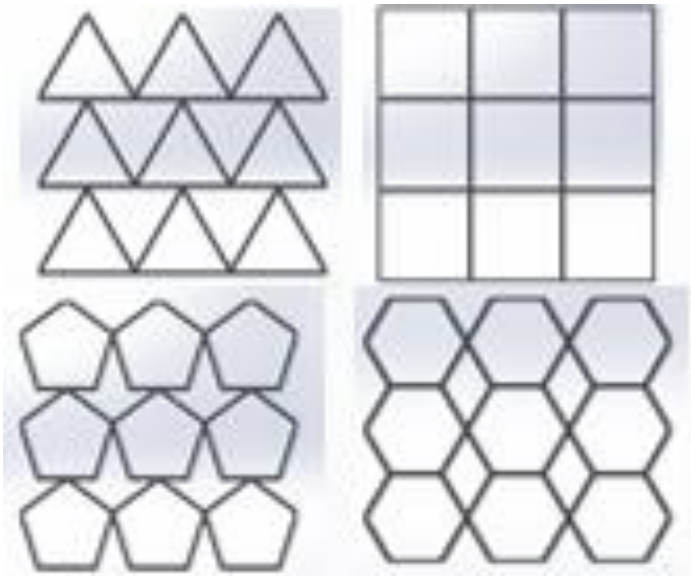

Figure 4-2: Different shapes fitted into the model

As seen in Figure 4-3, the unit cell used requires modifications to enable the array arrangement. This modification is necessary so that the unit cells will be connected at sharp edges (Figure 4-4) or to prevent double cell wall thickness at some of the connected faces (Figure 4-5). Merging of unit cells (Figure 4-6) are required to prevent the above and provide dimensional consistency.

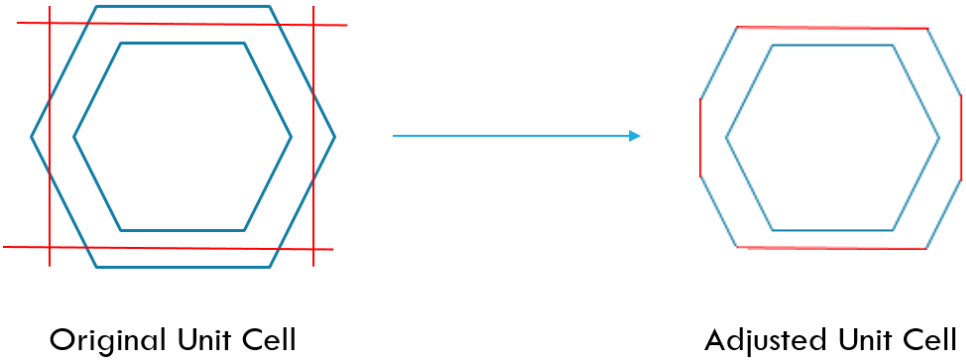

Figure 4-3: Modification of hexagonal unit cell

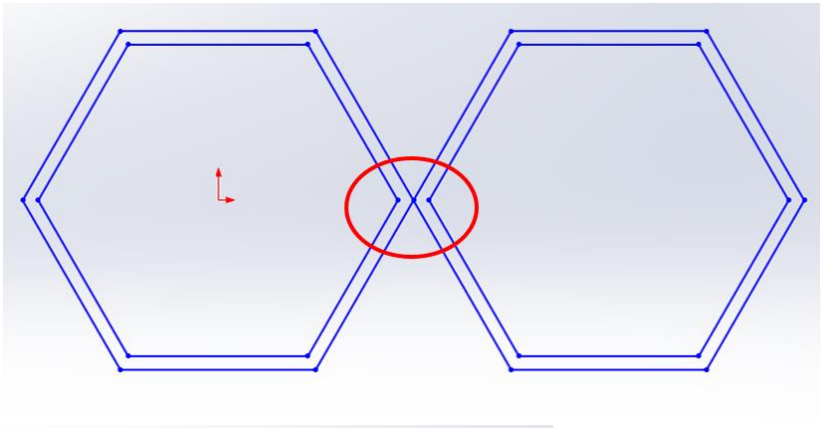

Figure 4-4: Connected at sharp edge

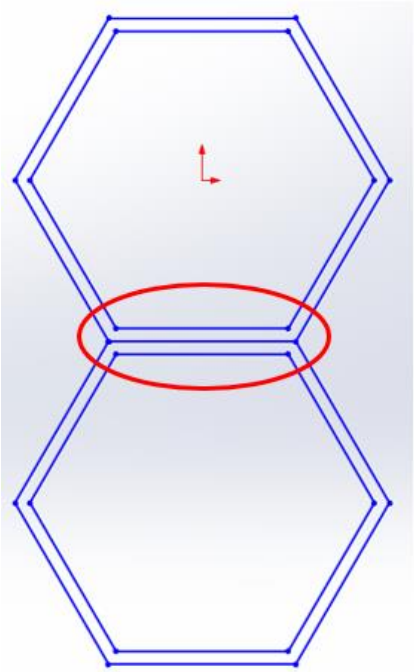

Figure 4-5: Doubled cell wall thickness

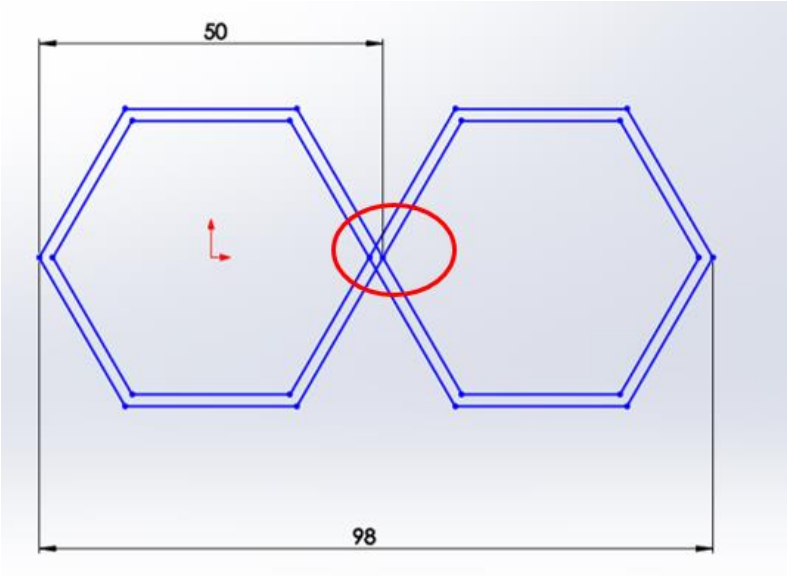

Figure 4-6: Merging of unit cells

The proposed model is designed to achieve constant relative density during scaling (cellular refinement) as seen in Figure 4-7. The relative density of 0.112 is obtained by calculating the ratio of volume of material making up the structure, to the apparent volume. This is as defined by Equation 1 found in Section 2.1.3 and Figure 4-8. Cellular refinement is the scaling down of unit cells from a unit cell of a 1 by 1 honeycomb based

on the refinement factor (***n***). For example, starting from a 1 by 1 hexagonal honeycomb, employing ***n*** = 5 will result in a 5 by 5 honeycomb with the exact same relative density as the 1 by 1 honeycomb. The unit cells are therefore 5 times smaller than those in the 1 by 1 honeycomb.

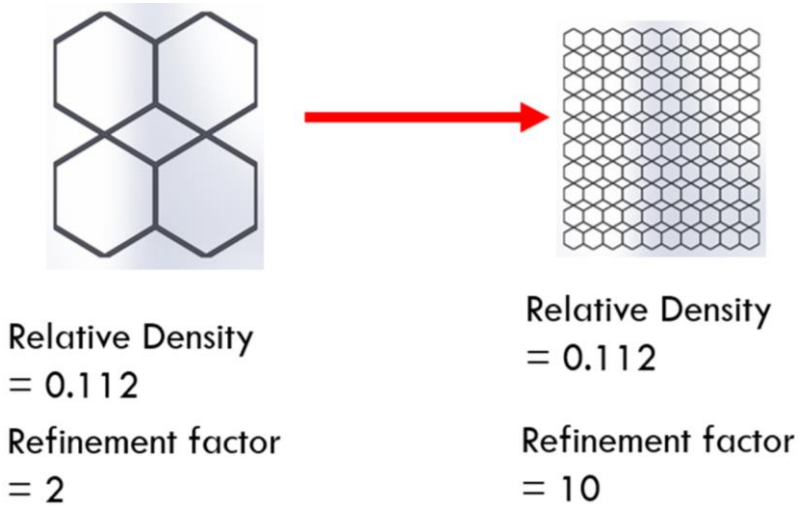

Figure 4-7: Cellular refinement while maintaining relative density

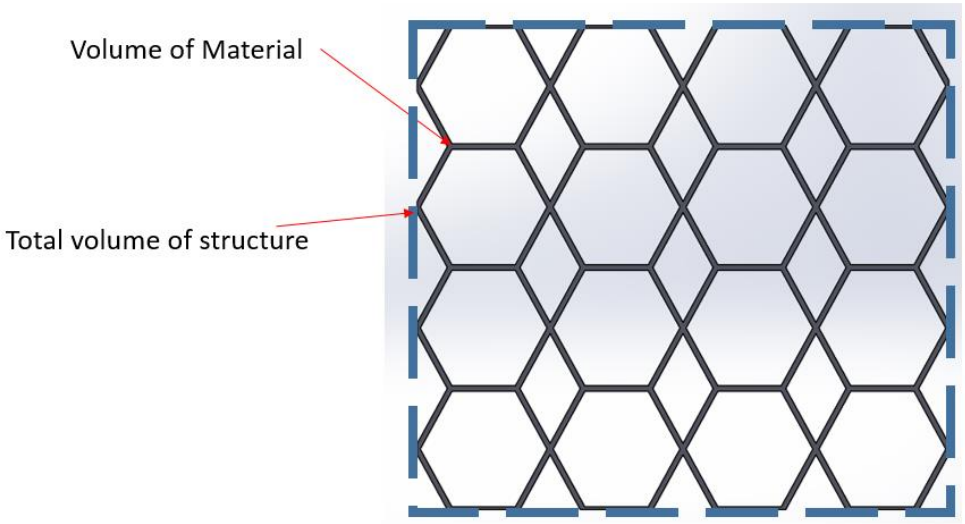

Figure 4-8: Volume of material vs total volume of structure

This design format is not restricted to honeycomb structures. It can also be applied to foam structures with the unit cells being polyhedrons instead of polygons. Similarly, modifications of the unit cells have to be performed. The parameters that can be controlled in designing cellular structure based on this model are:

a. Cellular shape
b. Cell wall thickness (***t***) (Figure 2-7)
c. Cell length (***l***) (Figure 2-7)
d. Refinement factor (***n***)

These parameters provide the opportunity for more comprehensive relations with the mechanical properties which will be useful when optimizing the structure. For this research, the focus is on polygonal array structures made up of hexagonal cells which will be termed as the Hexagonal Array.

4.2 HEXAGONAL ARRAY CUSHION DESIGN FLOW AND VARIABLES

For utilizing the Hexagonal Array for cushioning purposes, six design variables are selected. These design variables are:

1. Number of structural units (***c***)
2. Refinement factor (***n***)
3. Cell wall thickness (***t***)
4. Cell slenderness (***R***)
5. Elastic modulus ($\boldsymbol{E_s}$)
6. Contact area (***A***)

The design flow begins with the user defining the contact area, A. This area is limited to regular quadrilaterals (squares or rectangles). It is defined as the width of cushioning structure, ***X***, multiplied with the depth, $\boldsymbol{L_z}$ (Equation 33), as shown in Figure 4-9.

$$A = XL_z \tag{33}$$

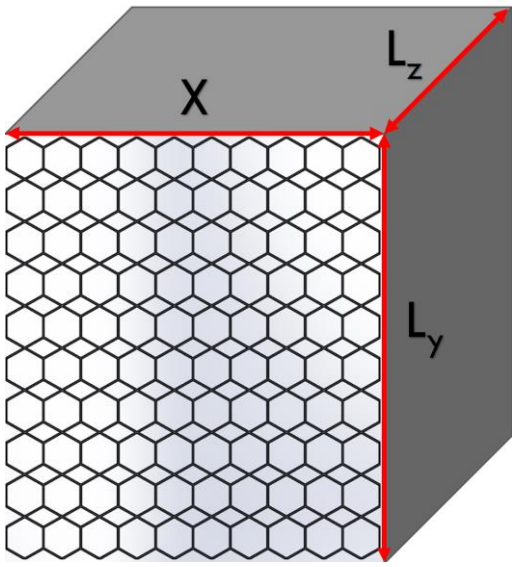

Figure 4-9: Geometry of a hexagonal array

The design process of the hexagonal array begins with assuming a square arrangement of cells (i.e. 2x2, 4x4, 5x5 etc). Therefore, for contact areas requiring very large X, the structures height, $\boldsymbol{L_y}$, will be very large as well because the number of cells or dimension of the cells will increase horizontally and vertically. This may lead to ridiculously thick foams which may not be feasible for fulfilling its purpose. Therefore, number of structural units, $\boldsymbol{c}$, is introduced to scale down $\boldsymbol{L_y}$ by repeating smaller structural units to cover the same $\boldsymbol{X}$. This is illustrated in Figure 4-10 where for the same $\boldsymbol{X}$, $\boldsymbol{L_y}$ is reduced by having the cellular structure scaled down by a factor $\boldsymbol{c}$ and repeated $\boldsymbol{c}$ number of times. Increasing the number of structural units will also result in higher relative density. The relationship between the cushioning structure's width, $\boldsymbol{X}$ and unit structural width, $\boldsymbol{L_x}$, is described in Equation 34.

$$X = cL_x \tag{34}$$

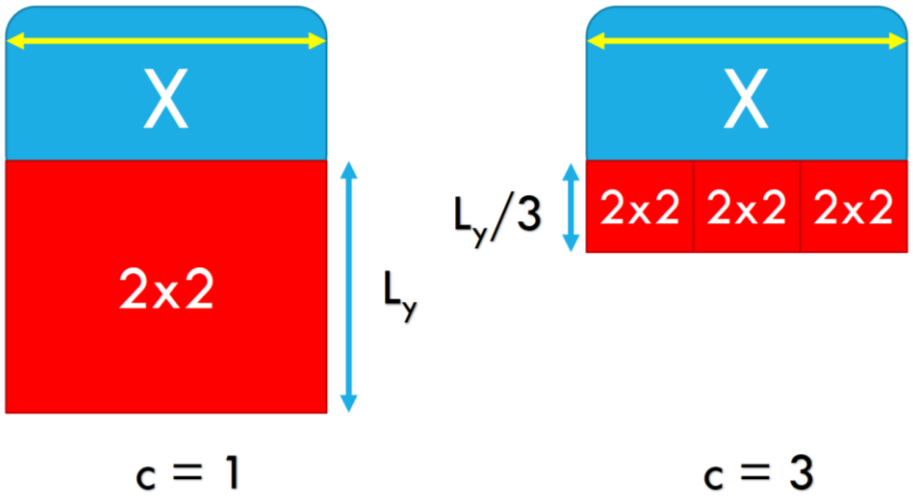

*Figure 4-10: Increasing number of structural units (**c**) to reduce $\boldsymbol{L_y}$.*

Subsequently, the refinement factor, cell wall thickness, cell slenderness and the material elastic modulus can be varied to achieve the desired mechanical properties. These are further elaborated in the subsequent sub-sections.

Refinement factor (n)

Increasing the refinement factor (***n***) will result in smaller geometrically similar unit cells occupying the same design space ($\boldsymbol{L_x}$ by $\boldsymbol{L_y}$) resulting in more cells. Due to the adjustments on the unit cells, relative density is kept constant when varying ***n***. This is mentioned in Section 4.1 and seen in Figure 4-2. The significance of increasing the refinement factor is that it increases the stiffness and strength of the structure possibly by increasing the ratio of inner cell walls to outer cell walls (Section 2.4).

Cell wall thickness (t)

As seen in Figure 2-6, the cell wall thickness, ***t***, is measured on the angled cell wall. Measuring on the vertical cell wall may result in an inaccurate value as the outer cell walls are trimmed as mentioned in Section 4.1. The thickness value used in the calculations is always the cell wall thickness of a 1 by 1 hexagonal array as shown in Figure 4-11. Therefore, in the following sections, this thickness will be referred to as initial thickness. However, logically, it is unreasonable to utilize a 1 by 1 structure for any energy absorbing or load bearing functions. Therefore, as seen in Equation 35, refinement factor, ***n***, is included as a scaling factor to adjust the thickness accordingly during cellular refinement. Varying the cell wall thickness directly affects the relative density of the structure.

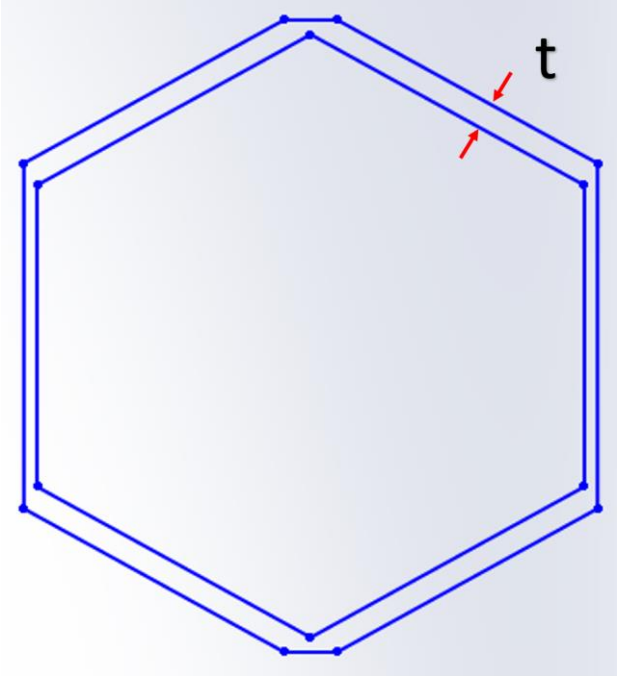

Figure 4-11: 1 by 1 hexagonal array

$$t = nt_n \tag{35}$$

where t_n is the cell wall thickness for a particular n.

Cell slenderness (R)

Cell slenderness R is the ratio of the inner vertical cell wall length to the inner angled cell wall length. Higher R value indicates a slenderer unit cell. This is as described in Figure 4-12 and Equation 36.

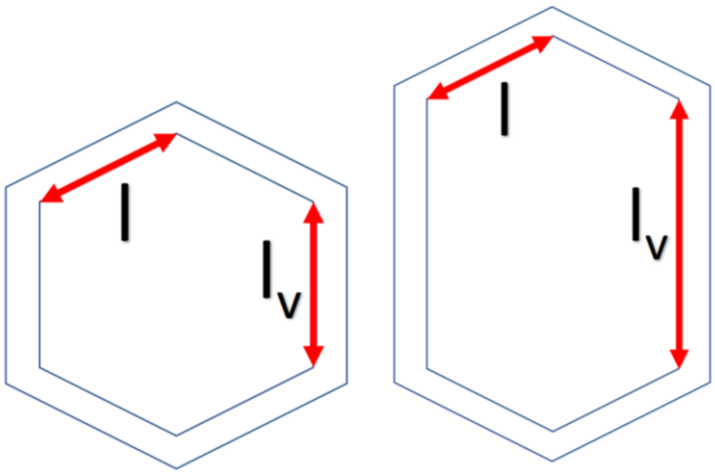

*Figure 4-12: Vertical cell wall length (**l_v**) and angled cell wall length (**l**); Unit cell with **R** > 1*

$$R = \frac{l_v}{l} \tag{36}$$

Recalling Equations 12 and 13, to reduce ***G***, a thicker cushion is required. However, in the conventional sense, this would mean more material, bulkier and heavier cushion. Alternatively, the unit cells can be made to be "taller" hence resulting in "thicker" cushions. This method still result in an increase in the cushion weight but in a much lesser degree. For example, using the conventional method to increase the thickness from 1 cm to 2 cm will double the weight of the cushion. However, by increasing ***R***, the weight increment for the same thickness increase is less than 50% (Figure 4-13).

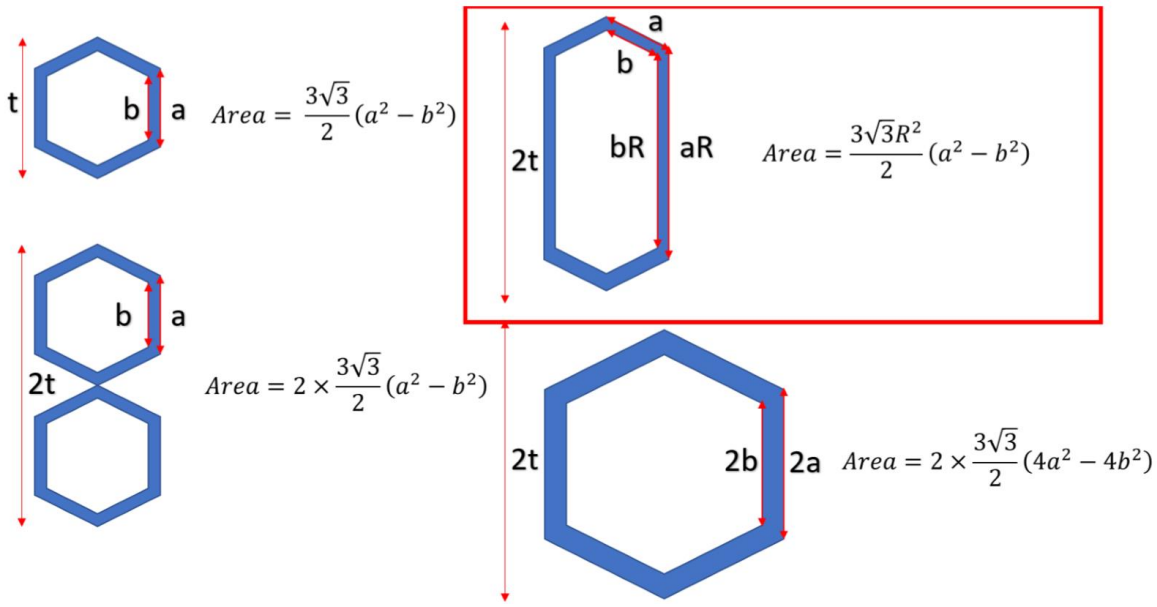

Figure 4-13: Increase in area due to doubling thickness. Slenderness ratio method has the least increase in area → least volume increase → least weight increase

However, the main advantage is that with more slender cell walls, the onset of elastic buckling will be earlier. This shortens the linear phase and extends the plateau phase resulting in a higher energy absorption efficiency. This directly translates to a higher shock absorption capacity (lower ***G*** level). Increasing the cell slenderness therefore increases the structures shock absorption capacity in two ways (increasing $\boldsymbol{L_y}$ and increasing $\boldsymbol{W_{eff}}$).

Elastic modulus

Apart from the geometry and size of the unit cells, the material that makes up the structure will also determine its mechanical properties. The 3D printer (Objet500 Connex3) used for this research is able to mix up to three different type of polymer resins to adjust its elastic modulus.

4.3 PRELIMINARY TESTS

Initial tests of hexagonal array structures involved the 3D printing of structures with $\boldsymbol{n}$ = 2, 5, 8 and 9, initial thickness, $\boldsymbol{t}$ = 2 mm and $\boldsymbol{L_x}$ = 50 mm with TangoPlus^{TM} resin. The resulting relative density is approximately 0.112 (Figure 4-14). An Instron universal testing machine was used to conduct the tests at a strain rate of 10 mm/min. The compression direction is shown in Figure 4-15 and the resulting stress-strain curves are shown in Figure 4-16. From the stress-strain results, it can be seen in Figure 4-17 that with cellular refinement, the linear modulus increases exponentially. The plateau stress also increases with cellular refinement.

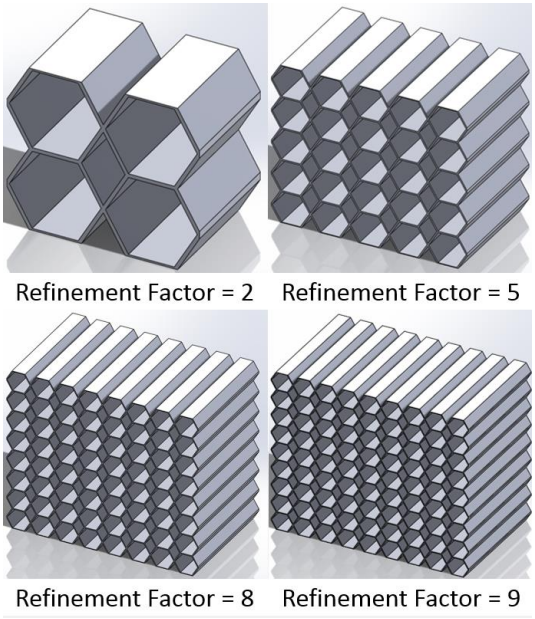

Figure 4-14: Hexagonal honeycombs CAD models of $\boldsymbol{n}$ *= 2,5,8 and 9,* $\boldsymbol{t}$ *= 2 mm,* $\boldsymbol{L_x}$ *= 50 mm*

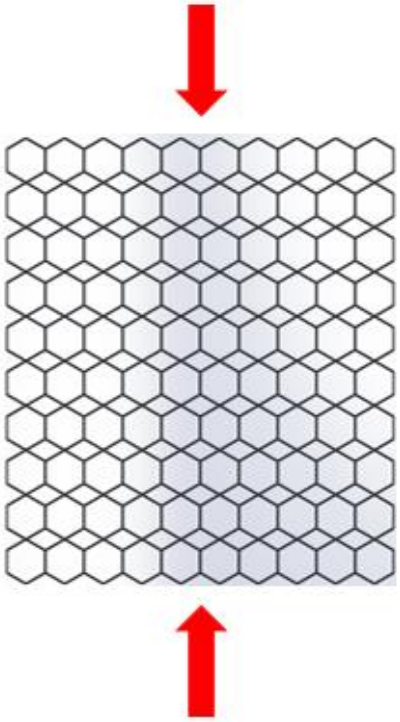

Figure 4-15: Compression direction

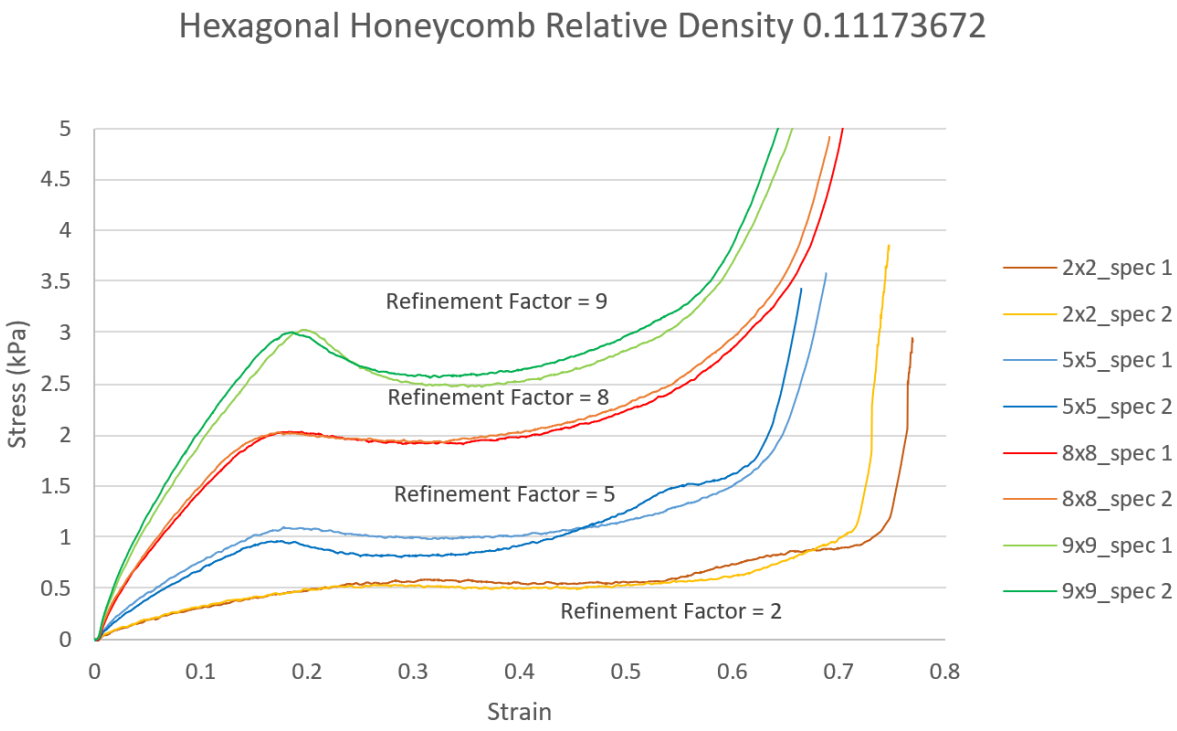

Figure 4-16: Compression stress-strain curve of hexagonal arrays showing increasing stiffness and plateau stress with increasing refinement factors.

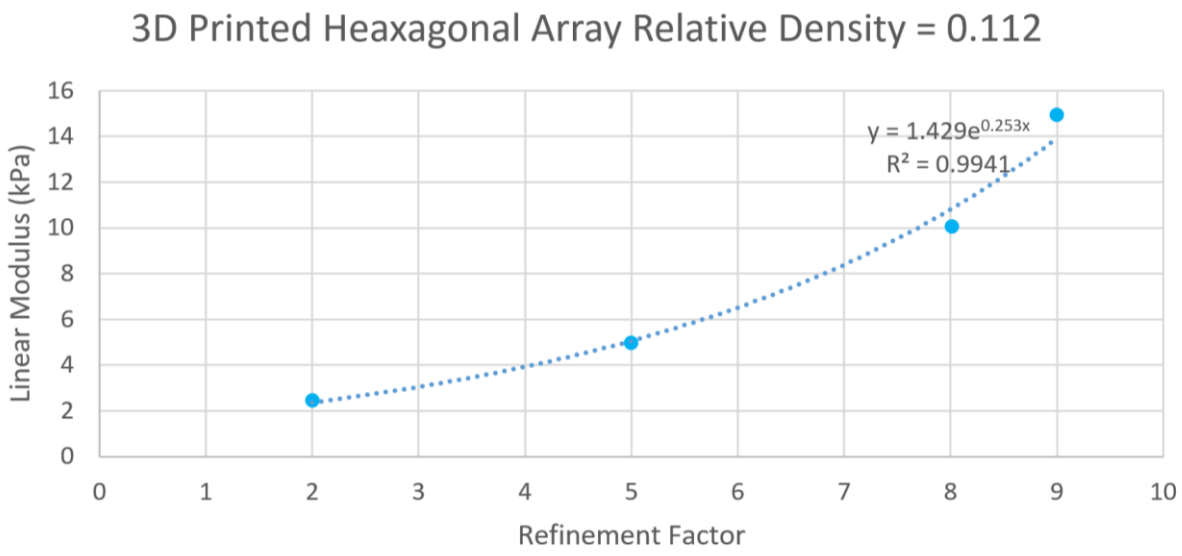

Figure 4-17: Exponentially increasing linear modulus with increasing refinement factor of 3D printed hexagonal arrays.

The obtained stress-strain curves as seen in Figure 4-16 shows typical curves of foams when subjected to compressive loading. The three distinct phases, which were mentioned earlier in Section 2.1.3, can be seen clearly. The increasing stiffness and strength is likely due to the increasing ratio of inner cell walls over the outer cell walls during cellular refinement. This may prove to be advantageous in designing cellular structures to have the desired mechanical properties while still keeping its light weight. To a small degree, the stiffening and strengthening of the structure may also be due to size effect [97] as mentioned in Section 2.4. Size effect is the deviation of materials' mechanical properties from the bulk properties as the size of geometrical similar features/parts/samples decreases.

4.4 MODELLING COMPRESSIVE STRESS RESPONSE FOR HEXAGONAL CELLULAR ARRAY

One of the main objective of this research is to accurately develop a mathematical model for the in-plane compressive stress response of the elastic hexagonal cellular arrays as seen in Figure 4-16. The model will be used to optimize the structural parameters for cushioning purposes. This model is based on mainly the geometry and topology of the structure. It was mentioned earlier, in Section 2.1.3, the compressive stress response of a cellular solid has three distinct phases. Different deformation mechanisms are responsible for each phase. To accurately model the stress response, detailed analysis of each phase is required.

4.4.1 Linear phase

For cellular structures made up of elastomers, the deformation during the linear phase is dominated by cell wall bending. By observing the physical deformation during the compression test itself, it is noted that only the highlighted cell walls in Figure 4-18 are deformed during this phase. These walls are the angled walls, the vertical cell walls remain un-deformed at low strain value.

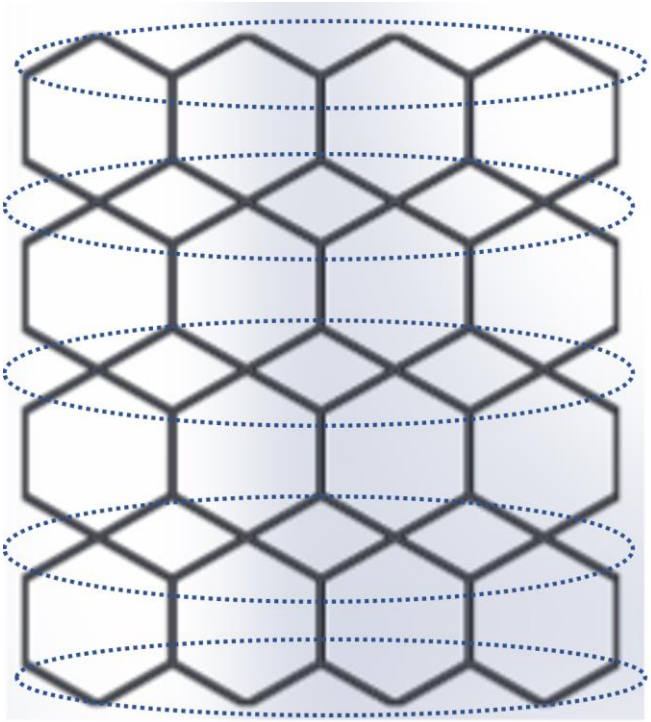

Figure 4-18: Cell walls deformed during linear phase

These walls are either experiencing half wave (red) or full wave (green) bending mode as shown in Figure 4-18. Only the outer cell walls experience half wave bending mode, this may imply that these walls are experiencing pin ends constraint conditions. It was mentioned in Section 2.4, the outer cell walls of any cellular structure are deemed to be free from stress [97]. These walls are therefore disregarded.

Figure 4-19: Half wave and full wave bending modes of the outer and inner cell walls respectively.

For conventional honeycombs, structural modulus $\boldsymbol{E^*}$ is calculated using Equation 3 in Section 2.1.3. This equation is based on the full wave bending mode. However, it does not account for the increasing ratio of inner walls to outer walls during cellular refinement. Therefore, as seen in Equation 37, a factor $\boldsymbol{K_n}$ was introduced to account for the cellular refinement effect on the structure's linear modulus $\boldsymbol{E^*}$ (average modulus of the linear phase). $\boldsymbol{K_n}$ is assumed to be a function of the refinement factor ($\boldsymbol{n}$) and is empirically determined.

$$E^* = \frac{4}{\sqrt{3}}\left(\frac{t}{l}\right)^3 E_s K_n \tag{37}$$

The linear phase continues until a critical strain, εp, is reached. As mentioned in Section 2.1.4, this is also the strain value at the onset of the plateau phase. The plateau phase begins when a critical load is reached. For elastomeric structures, this critical load is the load that is responsible for elastic buckling of the cell walls. The cell walls which buckle are the vertical cell walls as seen in Figure 4-20.

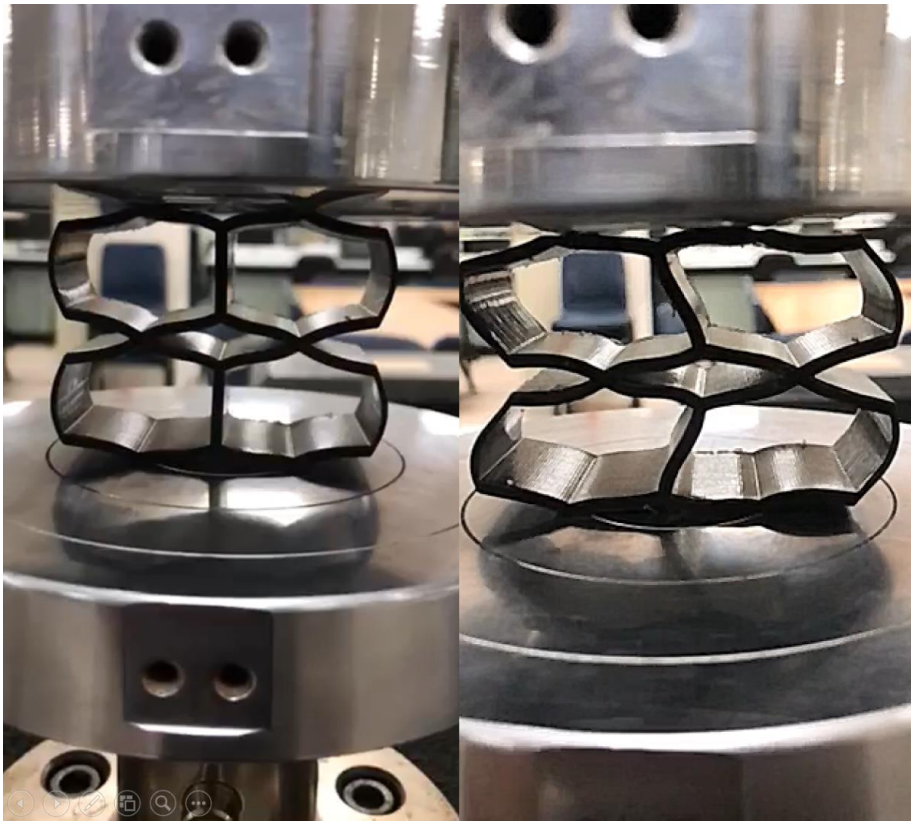

Figure 4-20: No deformation on vertical cell walls (Linear Phase); Buckling of inner vertical cell walls (Plateau Phase).

Since the vertical cell walls are the ones that buckle during plateau phase, it is observed that they are not deformed during linear phase hence the assumption that the stress is insignificant until a certain strain value is made. In this research, the aforementioned strain value is defined as the pre-buckling strain, $\boldsymbol{\varepsilon_p}'$. It was observed that the vertical cell walls start to buckle shortly after the apex of the hexagons are at about the same height as the highest point of the vertical cell wall (Figure 4-21). $\boldsymbol{\varepsilon_p}'$ is therefore the strain value at that instance.

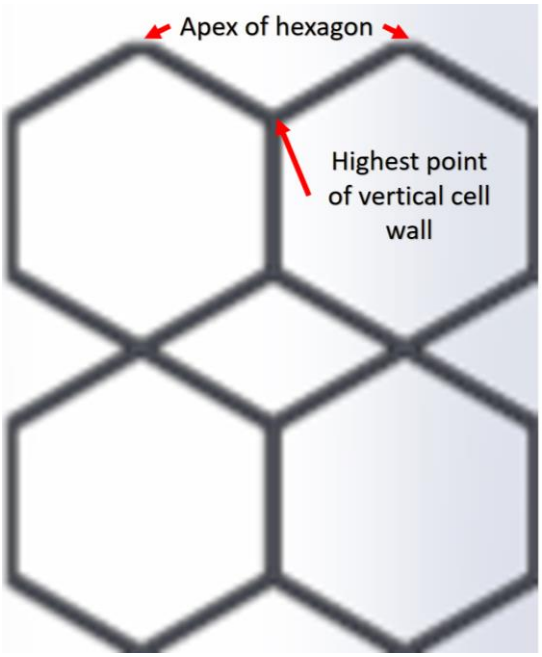

Figure 4-21: Apex of hexagon and highest point of vertical cell wall.

The pre-buckling strain value can easily be calculated by determining $\boldsymbol{\delta}$ (Figure 4-22) and utilizing Equation 38.

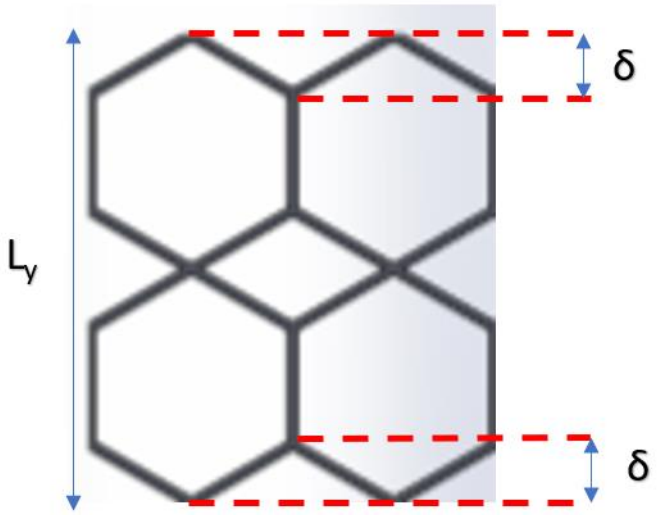

Figure 4-22: Deformation of hexagonal array corresponding to ε_p'

$$\varepsilon_p' = \frac{2\delta}{L_y} \tag{38}$$

For regular hexagons, or hexagons with all internal angles equivalent to 120˚, Equation 38 becomes Equation 39.

$$2\delta = 2l_2 \cos 60° = 2l_2(0.5) = l_2$$
$$\varepsilon_p' = \frac{l_2}{L_y} \tag{39}$$

The subscript "2" denotes that the internal cell wall length for a hexagonal array of a refinement factor of 2 is applied as a fixed value for all other refinement factors.

Equation 39 however does not account for relative density. At higher relative densities, it is expected that $\boldsymbol{\varepsilon_p}'$ is lower than calculated due to reduced porosity of the structure. Equation 40 therefore included a factor $\boldsymbol{K_R}$ which accounts for relative density. $\boldsymbol{K_R}$ is assumed to be a function of relative density and is hypothesized that it is equivalent to the porosity.

$$\varepsilon_p' = \frac{l_2}{L_y} K_R = \frac{l_2}{L_y} (Porosity) = \frac{l_2}{L_y} (1 - Relative\ density) \tag{40}$$

4.4.2 Plateau phase

From strain 0 to $\boldsymbol{\varepsilon_p}'$, the hexagonal array deforms linearly (Figure 4-19). Beyond that, the deformation is still considered linear. The only difference is that the vertical cell walls start to deform but the load is not high enough to result in buckling. The corresponding stress value when the structure buckles is the critical stress, $\boldsymbol{\sigma_{cr}}$, which can be determined based on Euler's critical buckling load [126] (Equation 41).

$$P_{cr} = \frac{\pi^2 E_s I_{m.i}}{(KL)^2} \tag{41}$$

K in Equation 41 is the column effective length factor which depends on the columns end support type. Physically examining the hexagonal array is not sufficient to determine the end support type. However, by observing how the cell walls buckle, the type of end support can be determined by matching the buckling mode to the end support types as shown in Figure 4-23 [126, 127].

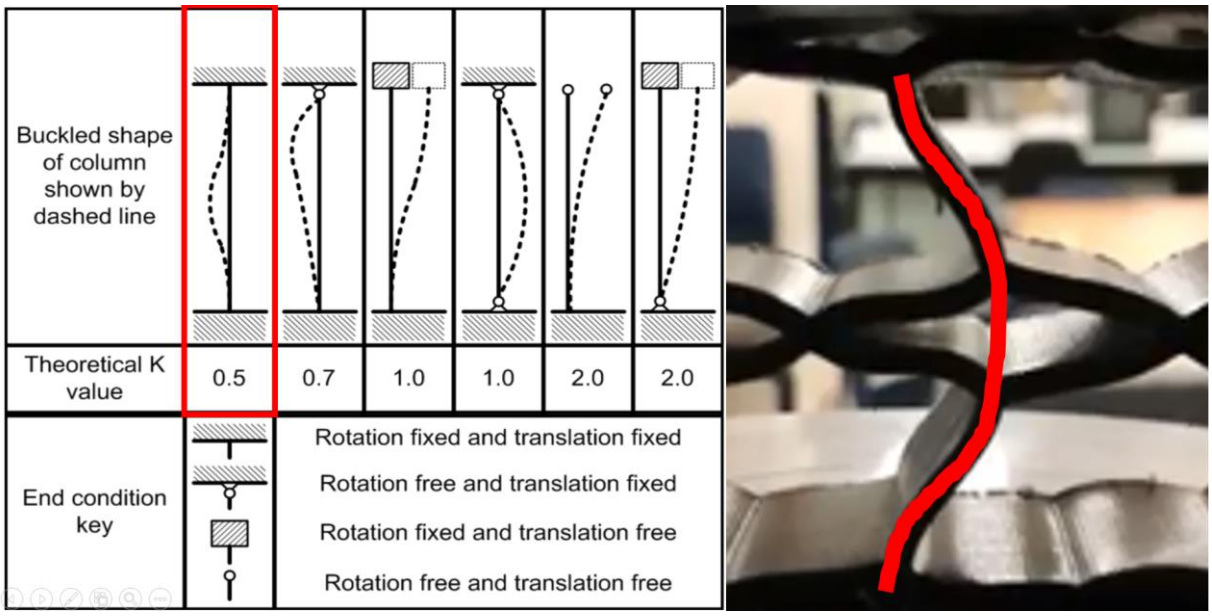

Figure 4-23: Buckling mode corresponding to end support type and their K values [127]; Buckling mode for the hexagonal array structures.

It is observed that although the vertical walls are not connected, they behave as one column with fixed support at both ends. The critical stress can therefore be described by Equation 42.

$$\sigma_{cr} = \frac{4\pi^2 E_s I_{m.i}}{AL^2} \tag{42}$$

where $\boldsymbol{I_{m.i}}$ is the area moment of inertia and $\boldsymbol{L}$ is the structures' total column height (Equation 42).

$$L = nl_2 \tag{43}$$

This phenomenon seen in Figure 4-23 is only observed in hexagonal arrays with even refinement factors, i.e. $\boldsymbol{n}$ = 2, $\boldsymbol{n}$ = 4, $\boldsymbol{n}$ = 6 and so on. For odd numbers, the buckling is unpredictable and unsymmetrical. This is due to a row of hexagonal cells being on the line of symmetry of the structure as seen in Figure 4-23. This row disrupts the symmetrical buckling of the structure. Therefore, for this project, the mathematical model developed are only for even $\boldsymbol{n}$.

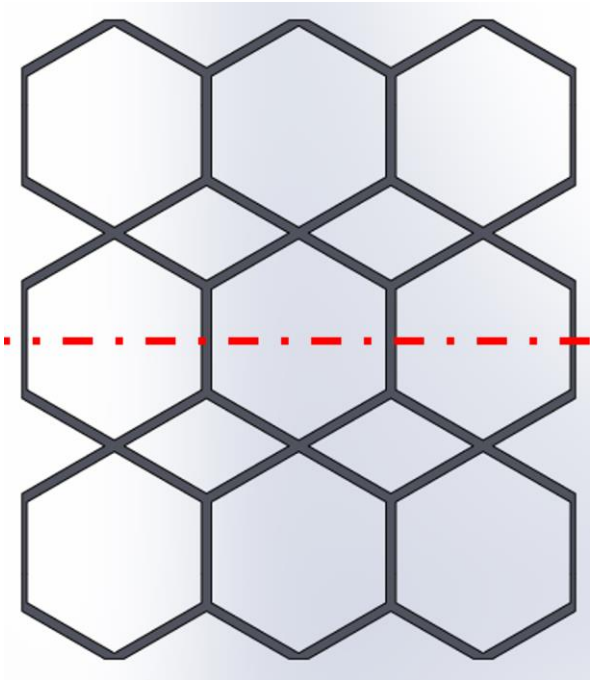

Figure 4-24: Row of cells on line of symmetry of the structure for odd ***n***

The plateau stress, $\boldsymbol{\sigma_p}$, is therefore the sum of $\boldsymbol{\sigma_{cr}}$ and the stress value at $\boldsymbol{\varepsilon_p}'$ which is as shown in Equation 44. The onset of plateau strain, $\boldsymbol{\varepsilon_p}$, can then be calculated with the obtained $\boldsymbol{\sigma_p}$ and $\boldsymbol{E^*}$ (Equation 37) with Equation 45.

$$\sigma_p = E^* \varepsilon_p' + \sigma_{cr} \tag{44}$$

$$\varepsilon_p = \frac{\sigma_p}{E^*} \tag{45}$$

4.4.3 Densification phase

The densification phase begins at a strain value which corresponds to the highest energy absorption efficiency. Initially, it was hypothesized that densification strain, ε_d, is a function of relative density. Logically, higher relative density would mean lower porosity hence the structure will reach densification earlier. However, experimental results suggest that for hexagonal array with relative density less than 0.4, the densification strain remains relatively constant at an average value of approximately 0.57. Therefore, a conservative value of 0.55 is chosen and the densification strain is assumed to be a constant for a range of relative densities of up to 0.4. Beyond relative densities of 0.4, the densification strain no longer averages out to 0.55.

4.4.4 Modelled vs actual stress-strain curves

The actual stress-strain curves were obtained by compressing structures of various ***t*** and ***n***. As mentioned in Section 3.2.3, printing of thin walls is an issue. Therefore, after conducting some test prints, the structures were designed with a minimum thickness of 0.5 mm.

Structures of ***n*** = 2, 3, 4 and 5, ***t*** = 5 mm, 6 mm, 7 mm, 8 mm, 10 mm, 12 mm and 15 mm, and $\boldsymbol{L_x}$ = 60 mm were printed with TangoBlack^{TM} resin resulting in a range of relative densities. Relative density is a function of ***t*** and $\boldsymbol{L_x}$. The equation which defines

relative density as a function of t and L_x was formulated. The derivation is as shown in Appendix B and the function is defined as Equation 46.

$$Relative\ density = -1.75\left(\frac{t}{L_x}\right)^2 + 2.5\left(\frac{t}{L_x}\right) \qquad (46)$$

$$0 < \frac{t}{L_x} < 0.7143$$

The limits of the equation represents the geometric feasibility limit of the hexagonal array. In other words, as the ratio of t/L_x increases beyond 0.7143, it is geometrically and physically impossible to reproduce a hexagonal array of such t/L_x value. The limit was identified by plotting the function from t/L_x = 0 to 1 (Figure 4-25) and observing a maximum point. This point represents the limit of the equation.

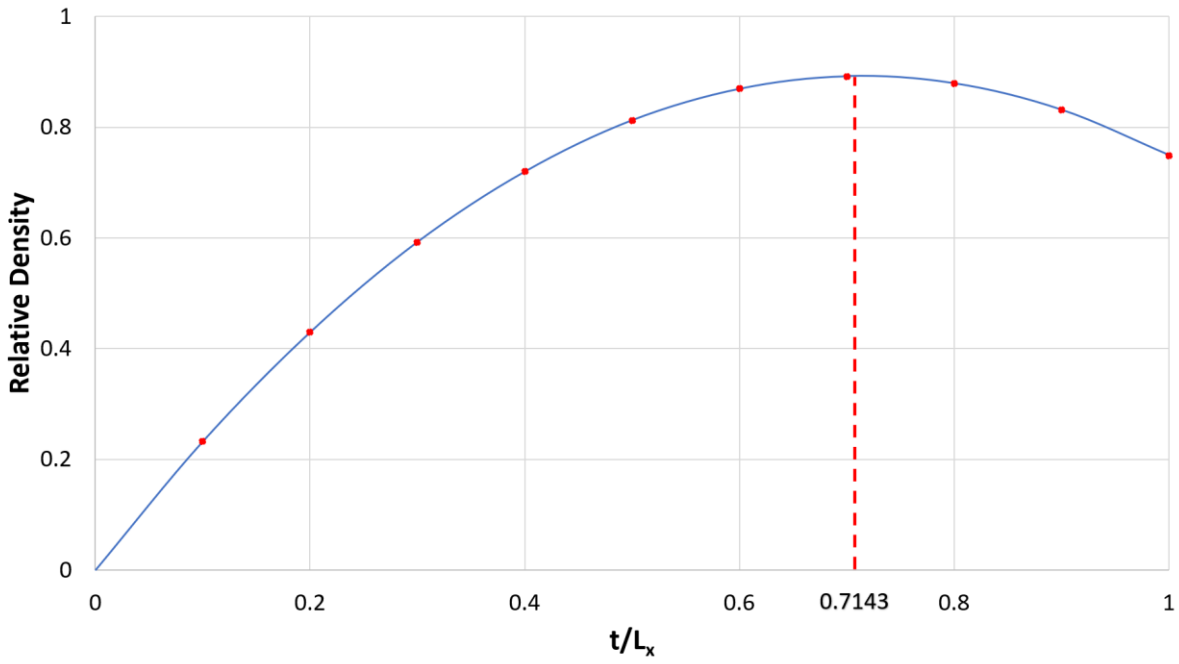

Figure 4-25: Relative density vs t/L_x

In Section 4.4.1, the factor K_n was introduced to account for the effect of cellular refinement on the linear modulus, E^*. To determine K_n, the measured linear modulus of various hexagonal arrays was plotted against their refinement factors as shown in Figure

4-26. An exponential function is fitted into the data with an R^2 value of 0.9802 which signals a good fit. Therefore, Equation 47 describes the relationship between K_n and n.

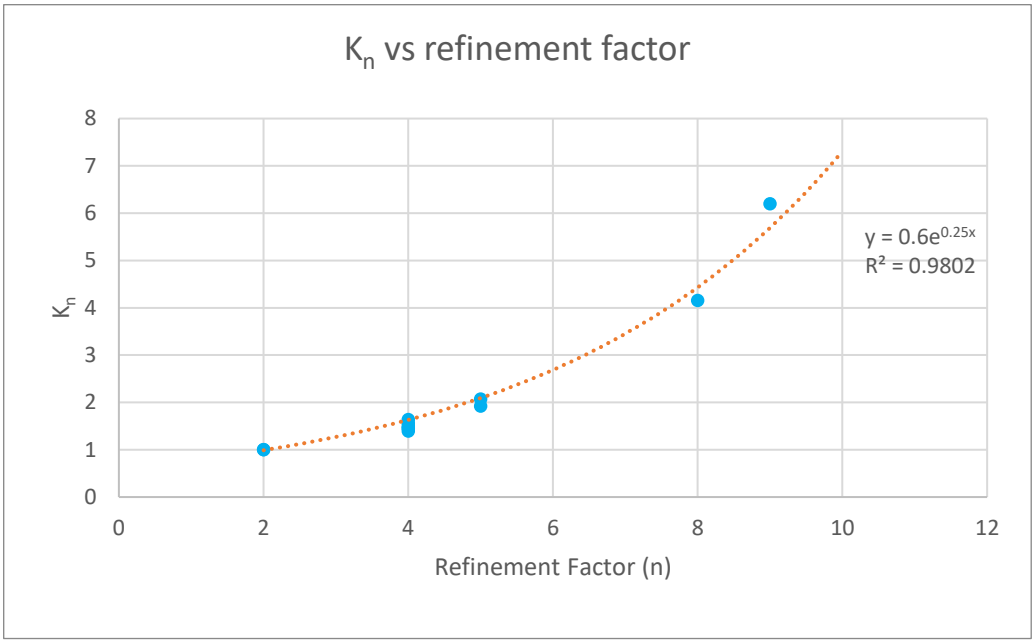

Figure 4-26: Determining the relationship between K_n and n.

$$K_n = 0.6e^{0.25n} \tag{47}$$

In theory, this relationship suggests that at very high n, the stiffness of the structure will be extremely high despite having no increase in weight. However, to further validate this relationship, structures with higher n should be fabricated and tested. This is however limited by the minimum feature size of the 3D printed. With nanotechnology, it is possible to fabricate structures of high n, however, this is beyond the scope of this research. Hence, based on the available data, it is assumed that Equation 46 is true for all n.

Figure 4-26 shows the effect of increasing the cell slenderness R (resulting in tall hexagonal array structures) on the stress-strain behaviour of the structure. In general, increasing R results in a lower plateau stresses and higher densification strain which increases the energy absorption efficiency of the cushion.

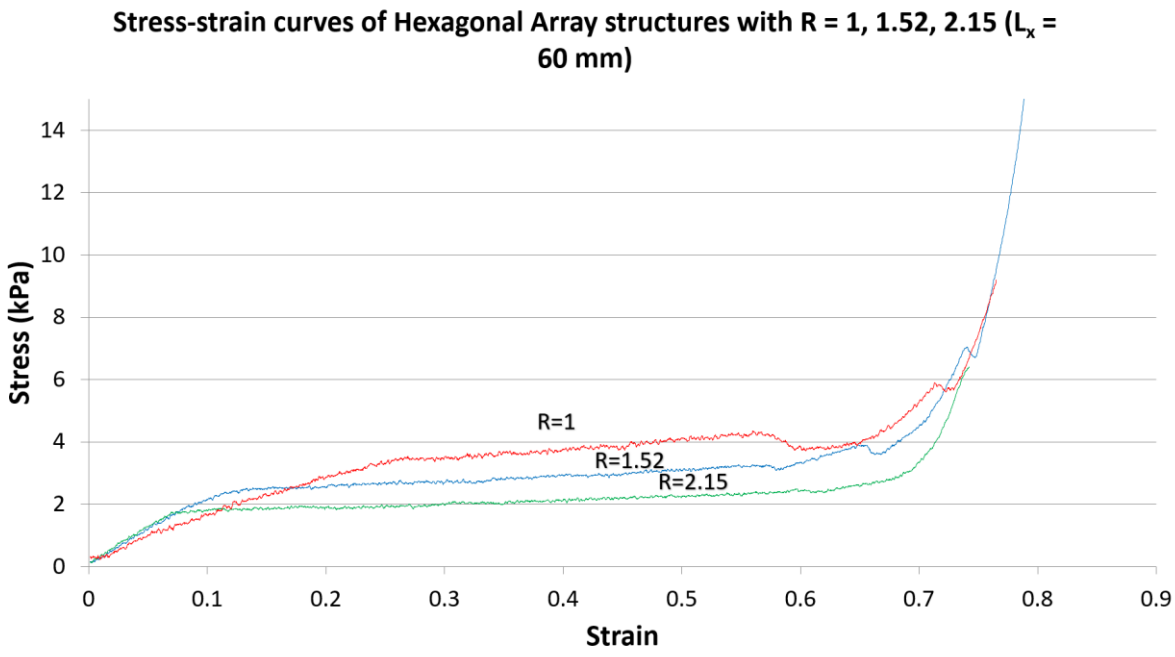

*Figure 4-27: Stress-strain curves for **R** = 1, **R** = 1.52, **R** = 2.15 (**L**x = 60 mm).*

To compare the mathematical model developed to predict the stress-strain response of hexagonal arrays with the actual stress-strain curves obtained, the R^2 value is calculated and displayed to represent how well the model fits the actual response. A second method of quantifying the fit is by comparing the actual and modelled energy absorbed at ε = 0.55 as a percentage difference (Equation 48).

$$\Delta W = \frac{W_{Actual} - W_{Model}}{W_{Model}} \times 100\% \tag{48}$$

In Figure 4-28, experimental stress-strain curve for a hexagonal array of t = 5 mm, n = 2 and L_x = 60 mm is compared to the modelled curve of the same structure. The R^2 and $\Delta W\%$ values implied a reasonable fit. The experimental stress starts to fluctuate beyond a strain of 0.3, probably due to cell wall tearing at the later part of the deformation process as observed during the experiments. Therefore, if the material used has a higher tear resistance, the curve would likely be able to fit better as the mathematical model does not account for cell wall tearing.

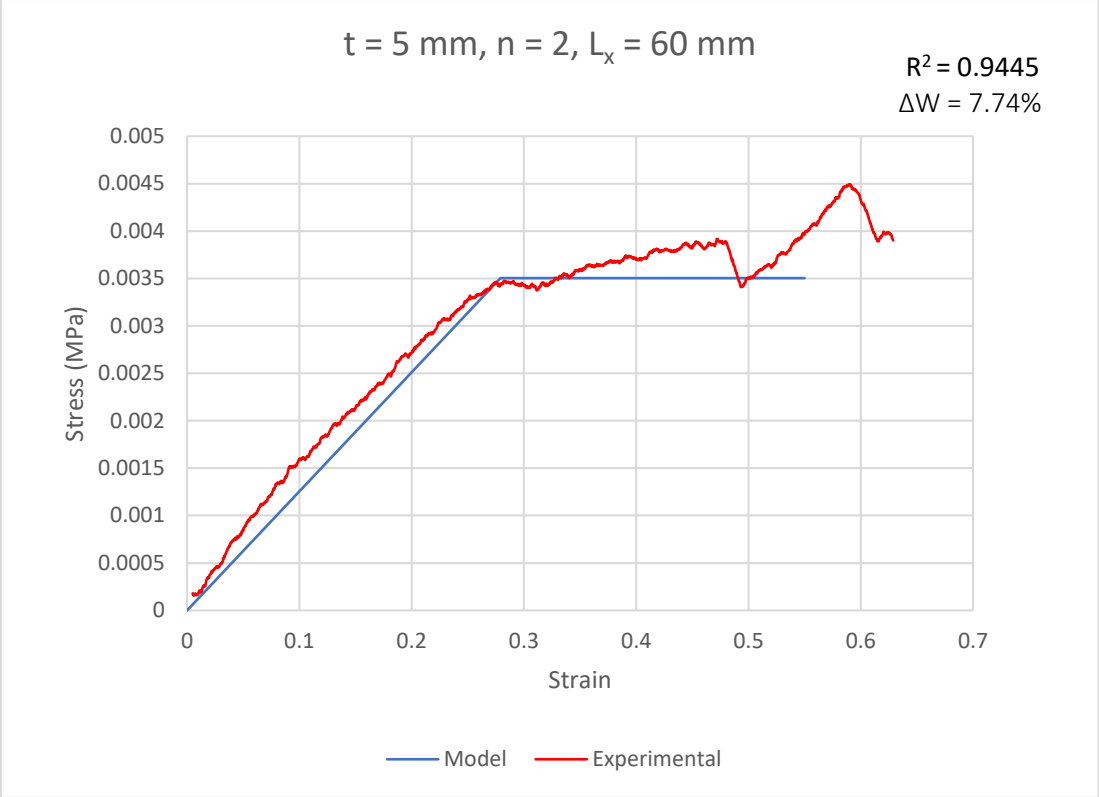

Figure 4-28: Actual and modelled stress-strain curves for t *= 5 mm,* n *= 2,* L_x *= 60 mm.*

As the thickness of the cell walls increase, with all else remaining the same, the cell wall tearing becomes more likely and will likely to occur earlier in the deformation process. This is observed in Figure 4-29 where t = 8 mm, n = 2 and L_x = 60 mm. Sudden change in stresses occurs more frequently and at a greater magnitude. The experimental curve exhibits a lower σ_p at the onset of the plateau phase when compared to the model. This is due to some of the cell wall tearing before the vertical cell walls can fully buckle thus altering the deformation process. Therefore, a lower R^2 of 0.7844 and a slightly higher ΔW of 8.44% resulted.

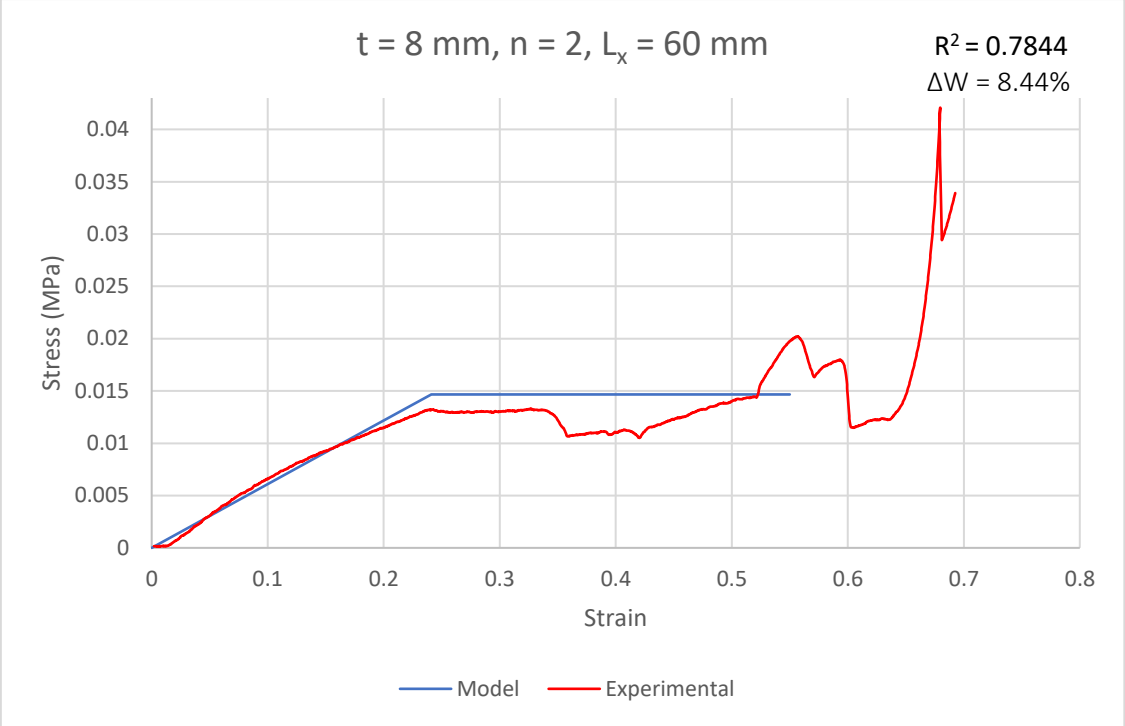

Figure 4-29: Actual and modelled stress-strain curves for t *= 8 mm,* n *= 2,* L_x *= 60 mm.*

However, for the same t, increasing the n to 4 reduces the occurrence of cell wall tearing as seen in Figure 4-30, where the experimental stress-strain curve is smoother. The experimental average σ_p value is still lower than the calculated value based on the model as there are still occurrences of tearing. However, there are fewer cell wall tearing and does not affect the deformation process significantly. The model fits significantly better with an R^2 of 0.9541 and ΔW of 6.02%.

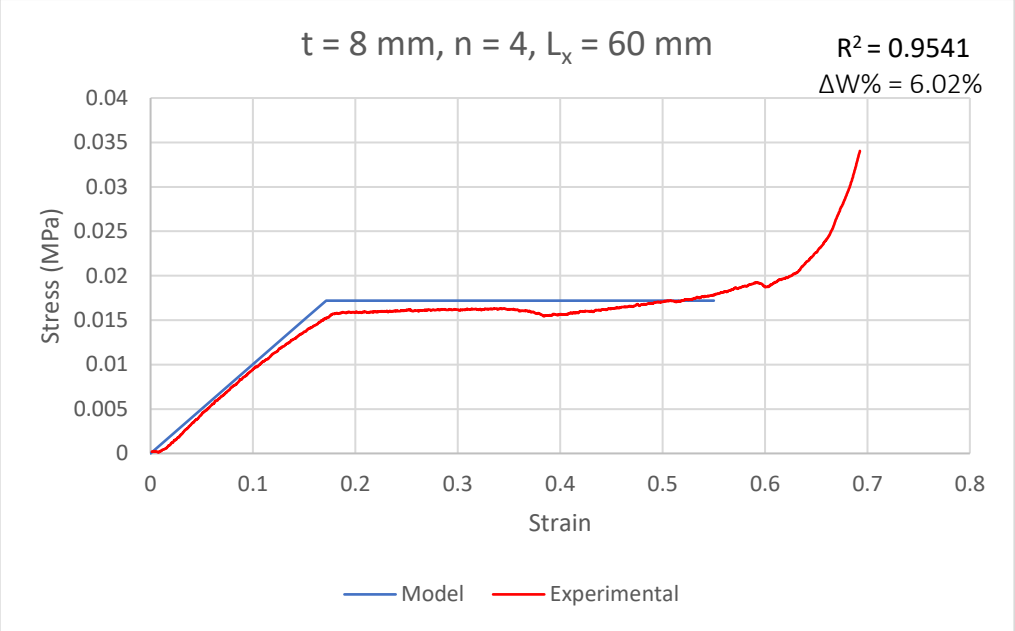

Figure 4-30: Actual and modelled stress-strain curves for ***t*** *= 8 mm,* ***n*** *= 4,* L_x *= 60 mm.*

Hexagonal array with very thick cell walls tear more easily and the model can no longer be accurately fitted to the experimental stress-strain curve as shown in Figure 4-31. As mentioned in Section 4.4.3, the average densification strain of 0.55 only applies for structures of relative density less than 0.4. For this structure (Figure 4-31), the relative density is 0.43 and the densification strain is 0.485.

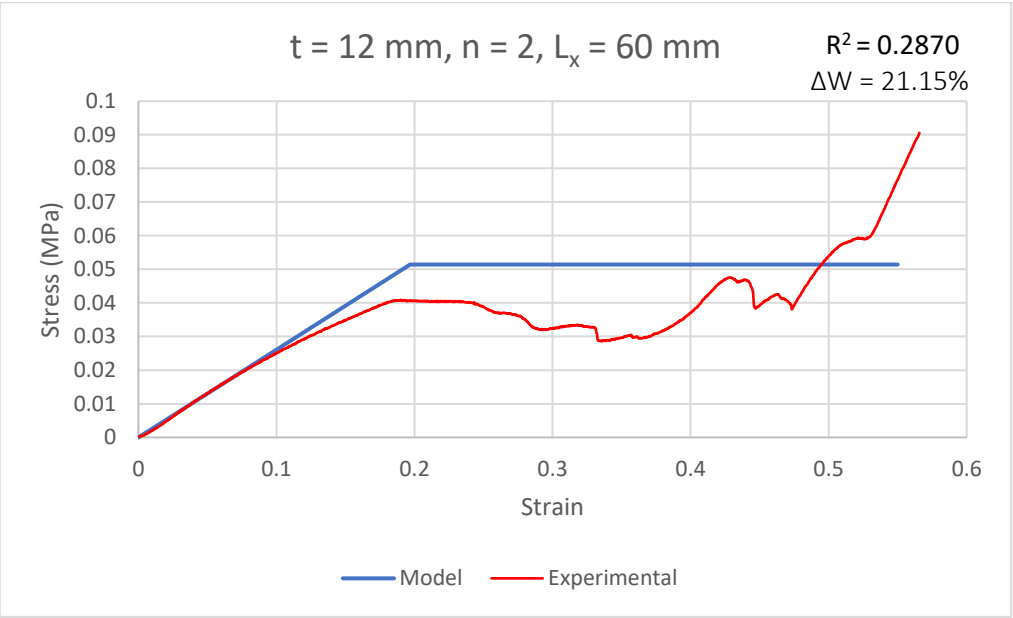

Figure 4-31: Actual and modelled stress-strain curves for ***t*** *= 12 mm,* ***n*** *= 4,* L_x *= 60 mm.*

In Figure 4-32, R^2 and ΔW values for the various hexagonal arrays are plotted against their resulting relative densities as a summary of how well the model predicts the stress response of each structure. Increasing relative density indicates increasing cell wall thickness and hence cell wall tearing was more frequent affecting the deformation of the structure. The curve fitting and how well the model predicts W_d (energy absorbed at densification) is therefore affected and hence the observed increasing of ΔW with increasing relative density. Therefore, the mathematical model developed to predict the stress response of hexagonal array can accurately model structures of low relative density and made up of materials with high tear resistance.

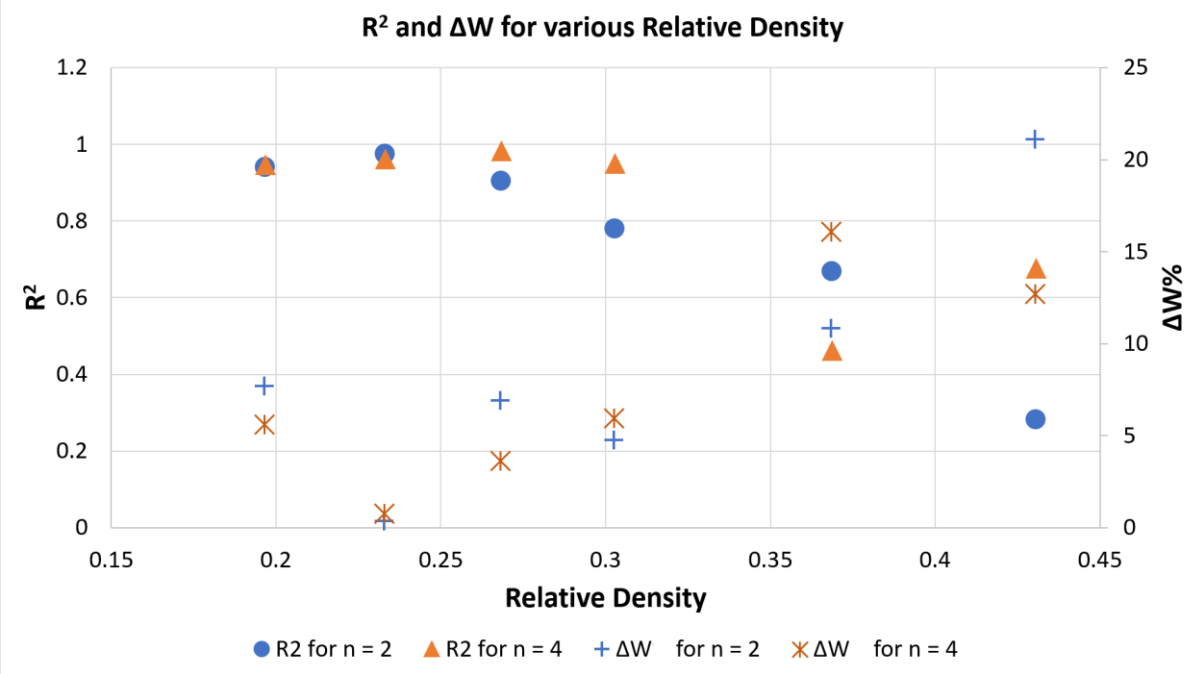

Figure 4-32: R^2 and ΔW for various relative densities.

As mentioned earlier, the densification strain is estimated to be a constant value of 0.55. However, there will be cases where the actual densification strain is lower or higher than 0.55 as demonstrated in Figure 4-31. If the actual densification strain is higher than 0.55, the actual W_d will be higher. Therefore, designing a cushion where the assumed densification strain is lower than the actual will result in the cushion not being fully utilized, i.e. not up till maximum W_{eff} (Figure 4-33). If the actual densification strain is

lower than 0.55, the cushion will be compressed well into the densification phase. This may result in flattening out the cushion and cause damage to the item meant to be cushioned (Figure 4-33).

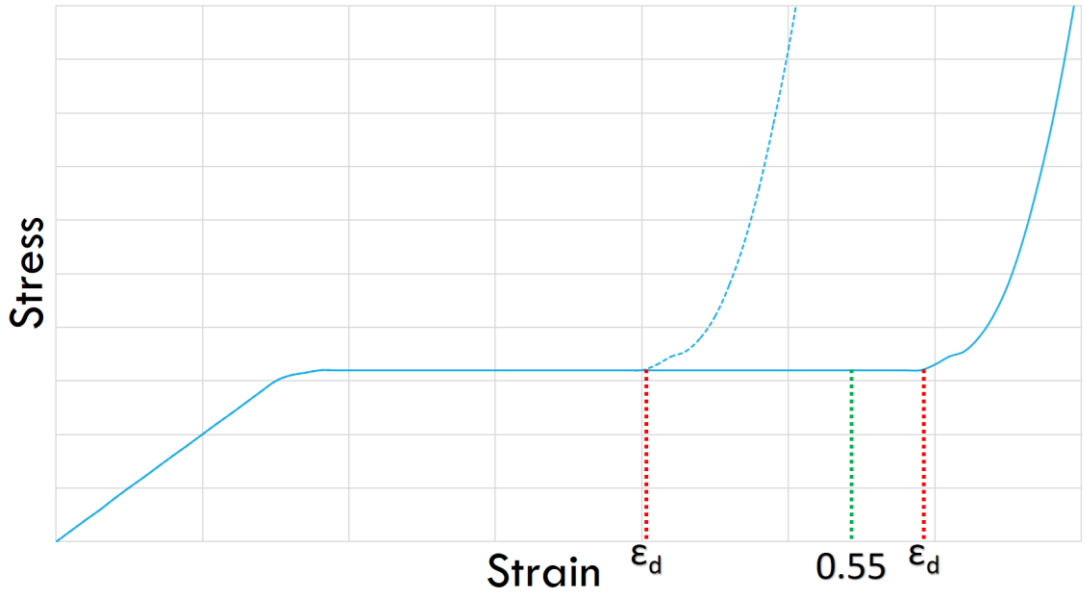

Figure 4-33: Instances if actual densification is before or after the estimated densification strain.

If the structure is optimized to meet the cushioning requirement at a strain of 0.55, if the cushion is underutilized, it will perform as designed. On the other hand, problems will arise if the estimated strain of 0.55 is found to be after $\boldsymbol{\varepsilon_d}$. However, this is unlikely for low relative density structures (< 0.4). Therefore, for low relative desity, it is safe to assume a constant densification strain of 0.55.

4.5 SUMMARY

Adjusting a cellular structure's property while keeping its weight constant is possible with the "Polygonal/Polyhedral Cellular Array". By adjusting its unit cells and arranging them in an array formation, the relative density and overall dimensions of the structure will be preserved when scaling up/down the unit cells. Scaling down or refining the cells will result in stiffer and stronger structures.

A range of parameters dictates the overall design of the structure. These allow for greater control of the resulting properties of the structure. These parameters can be optimized for the structure to meet various applications. For the "Hexagonal Array", the parameters defining its overall design can also model its compressive stress-strain response to a limited extend.

The key findings/information include:

1. The stiffness of the Hexagonal Array increases exponentially with cellular refinement. The strength also increases with cellular refinement. This potential is however currently limited by the minimum feature size of 3D printers. The minimum feature size of the Polyjet printer limits the lowest relative density to approximately 0.12 as well as the number of cells per structure. It is however assumed that due to the regular arrangement and predictability of the deformation, apart from refinement factor, the number of cells per structure does not significantly affect the observations and conclusion.
2. The introduction of slenderness ratio $\boldsymbol{R}$ of cells will result in cushions with better $\boldsymbol{W_{eff}}$ by making the structure buckle earlier.
3. Cell wall tearing is dominant in structures with low $\boldsymbol{n}$ and high relative densities. The mathematical model for Hexagonal Arrays does not account for cell wall

tearing. Size effect which by definition is the deviation of the materials' properties from the bulk properties as the size of geometrical similar features/parts/samples decreases [128], is also not accounted by the model. The smallest relative density for which the mathematical model can be applied for accurately is dependent on the characteristic length of the material [129]. The smaller the characteristic length, the lower the relative density limit is. For rubbers, size effect is relative absent for features not smaller than approximately 2 microns [129]. This makes the lower relative density limit for rubber hexagonal arrays approximately 0.0005. For cell wall tearing, it is observed to be significant at relative densities of > 0.4.

CHAPTER 5 – PARAMETER OPTIMIZATION FOR CUSHIONING

To optimize the Hexagonal Array structure for cushioning purposes, first, the modelled compressive response must be associated to the established cushion selection methods. The method of choice for most practitioners is with the aid of cushioning curves. Therefore, this chapter will present the method of associating cushioning curves with the stress-strain response of Hexagonal Array followed by formulating an optimization algorithm. It will then conclude with several case studies where the algorithm developed is applied.

5.1 GENERATING CUSHIONING CURVES

In Section 2.3, the conventional method of generating cushioning curves were discussed along with alternative methods. The method suggested by Gruenbaum and Miltz [87] was deem suitable above all others as it is capable of generating a set of cushioning curves for various foam height and drop-height from just one static compression test. The logistics requirement is relatively low and straightforward.

In this section, the method is tested on PE foams (1.7 pcf, 2-inch) for verify the theory behind this method. Following that, the theory is further expanded and incorporated as part of the cushioning optimization process.

5.1.1 Drop test on PE foams

Drop test were performed on PE foams (90 mm by 100 mm by 50 mm), dropping a mass of 3.291 kg from 15 mm, 30 mm and 45 mm drop-heights. Ten specimens were prepared by cutting from a 2000 mm by 1000 mm by 50 mm PE foam board and labelled 1 to 10

(Figure 5-1). Five samples were selected at random for testing. The experimental set up is as shown in Figure 3-7 in Section 3.2.3.

Figure 5-1: PE foam specimens for drop-test

The resulting experimental dimensionless deceleration G_{exp} (deceleration divided by 9.81 ms^{-2}) values are presented in Table 6. Performing static compression tests on the PE foams and applying the method suggested by Gruenbaum and Miltz [87] resulted in predicted dimensionless deceleration G_{cal} values as listed in Table 5-1 as well.

Table 5-1: Measured and calculated dimensionless deceleration experience by drop weight on PE foams

Drop-heights (mm)	Experimental average deceleration (G_{exp}) (n = 5)	Calculated deceleration (G_{cal})	% Difference ($G_{exp} - G_{cal}$)/G_{exp})
15	23.014	17.977	21.9
30	41.959	31.809	24.2
45	66.696	46.375	30.5

As observed, at 15 mm drop-height, the % difference between G_{exp} and G_{cal} is the lowest. However, with increasing drop-heights, the difference between the measure G and the calculated G increases. This is consistent with the results reported by Gruenbaum and Miltz [87] (highlighted in Section 2.3.1). The same observation can be expected for decreasing foam thickness.

This method is a viable method which can be further improved by incorporating the dynamic factors discussed in Section 2.3.3. The dynamic factor is a function of both strain and strain rate. To accurately determine it, large amount of physical experiments and in-depth study is required. However, due to resource limitations, this can only be earmarked for future work. At the current moment, the dynamic effect is acknowledged but must be temporarily disregarded due to the resource limitations.

5.1.2 Expansion of method

By combining Equations 12 and 13 in Section 2.3.1, ***G*** can be seen to be clearly and directly related to ***H*** and L_y:

$$G = \frac{\sigma}{\int_0^{\varepsilon} \sigma \, d\varepsilon}\left(\frac{H}{L_y}\right) \tag{49}$$

For a cushion compressed up till a certain strain value of ε = b, Equation 49 can then be further simplified to Equation 50.

$$G = \frac{\sigma_b}{W_b}\left(\frac{H}{L_y}\right) \tag{50}$$

Recall in Section 2.2.4 (Figure 2-18), "Method C", the optimal design point for any cellular structure is at the strain value where the energy absorbed (W) to stress (σ) ratio or W_{eff} is at its maximum. Observing Equation 50, for any cushion, the shock absorption capacity is at its maximum when W/σ or W_{eff} is at its maximum (σ/W at its minimum) as it will return the lowest possible ***G*** for a particular combination of ***H*** and L_y. Conveniently, the optimal design point (maximum W/σ or W_{eff}) is also the densification point (refer to Section 2.1.4) [50].

Therefore, it can be deduced that any specific foam or honeycomb is optimally meant to provide a shock absorption capacity of $\boldsymbol{G}$ for an item with a static stress ($\boldsymbol{\sigma_s}$) described by Equations 50 and 51 respectively.

$$G = \frac{\sigma_d}{W_d}\left(\frac{H}{L_y}\right) \tag{50}$$

$$\sigma_s = W_d\left(\frac{L_y}{H}\right) \tag{51}$$

where the subscript "d" denotes densification.

This reduces the number of steps involved in the cushioning selection process. For any cushioning structure, the densification point, energy absorbed at densification ($\boldsymbol{W_d}$) and densification stress ($\boldsymbol{\sigma_d}$) can quickly be identified. Utilizing Equations 50 and 51, the cushion's shock absorption capacity and the ideal weight of the item to be cushioned can be quickly identified.

5.2 OPTIMIZATION ALGORITHM

In Section 4.2, it was mention that there are six design variables for the Hexagonal Array structure. Five of the variables are purely geometrical whereas the remaining one is the elastic modulus of the solid material. During the design process, the elastic modulus should not be an optimized value as it is a fix and discreet value depending on the available materials.

Out of the remaining five variables, one of them, the contact area of the cushion, is pre-determined during the design process based on the user specification. The remaining four variables have their own constraints which governs the range of values they can hold. Table 5-2 summarizes these four variables and the constraints they are each subject to.

Table 5-2: Optimizable design variables and their constraints

DESIGN VARIABLE	CONSTRAINTS
Initial thickness, t (mm)	$\boldsymbol{t} > 0$
Number of structural units, c	Must be an integer, $\boldsymbol{c} \geq 1$
Refinement factor, n	Must be an even integer, $\boldsymbol{n} \geq 2$
Cell slenderness, R	$\boldsymbol{R} \geq 1$

Prior to the optimization process, the user will input three important values:

1. **Item fragility**: The item's fragility is represented in terms of $\boldsymbol{G}$. The cushioning structure must have a shock absorption capacity of $\boldsymbol{G} \leq \boldsymbol{G_{item}}$.
2. **Item mass**: The item's mass is measured in kg and will determine the $\boldsymbol{\sigma_s}$ it will exert on the cushioning structure. This is as described by Equation 52 and will ensure that the optimized cushion is capable of having the above-mentioned shock absorption capacity for an item of the stated mass.

3. **Required contact area (*X* by L_z)**: The contact area will also determine σ_s. This is also as described by Equation 52. But most importantly, it determines the design space for the cushion.

$$\sigma_s = \frac{mg}{XL_z} \tag{52}$$

Table 5-3 summarizes the requirements of a cushion. The item's fragility (G_{item}) is the the maximum deceleration (in terms of G) the item can experience before getting damaged. The shock absorption offered by the cushion ($G_{cushion}$) should always never be greater than the item's fragility. The most important requirement is the static stress (σ_s) since if a cushion is optimized to cushion an item of a certain weight, any significant change to the weight will not allow the structure to cushion it optimally. The least important is the mass of the cushion, ideally the cushion should be as light as possible, but it must meet the first two requirements.

Table 5-3: Cushioning requirements

	REQUIREMENTS
Item's fragility (G_{item})	$G_{cushion} \leq G_{item}$
Static stress (σ_s)	$\sigma_{s,cushion} = \sigma_s$
Cushion mass ($m_{cushion}$)	As low as possible

Therefore, the objective of the optimization problem should be to minimize the cushions weight subjected to constraints which ensure that the first two requirements are met, and the design variable constraints. The optimization problem is therefore defined as:

Minimize $$f = Relative\ density(XL_yL_z)\rho_{material} \tag{54}$$

subject to

$$h_1 = \sigma_{s,cushion} - \left(\frac{mg}{XL_z}\right) = 0 \quad (55)$$

$$g_1 = G_{cushion} - G_{item} \leq 0 \quad (56)$$

$$g_2 = -t < 0 \quad (57)$$

$$g_3 = 1 - c \leq 0 \quad (58)$$

$$g_4 = 2 - n \leq 0 \quad (59)$$

$$g_5 = 1 - R \leq 0 \quad (60)$$

$$c, n \quad integer$$

The above optimization problem can be solved by using Microsoft Excel Solver. In the next section, case studies of various cushioning requirements are presented.

5.3 CASE STUDIES

In these case studies, applicable conventional foams are compared with the optimized hexagonal array structures to meet the same cushioning requirements.

5.3.1 Case study 1

An item with a mass of 9 kg has a fragility value of 80 G. It requires a cushion of a contact area of 375 mm by 375 mm. The transportation mode of the item involves a risk of the packaging being dropped over a maximum height of 750 mm. Conventionally, a cushioning curve for a drop-height of 750 mm is required as shown in Figure 5-2.

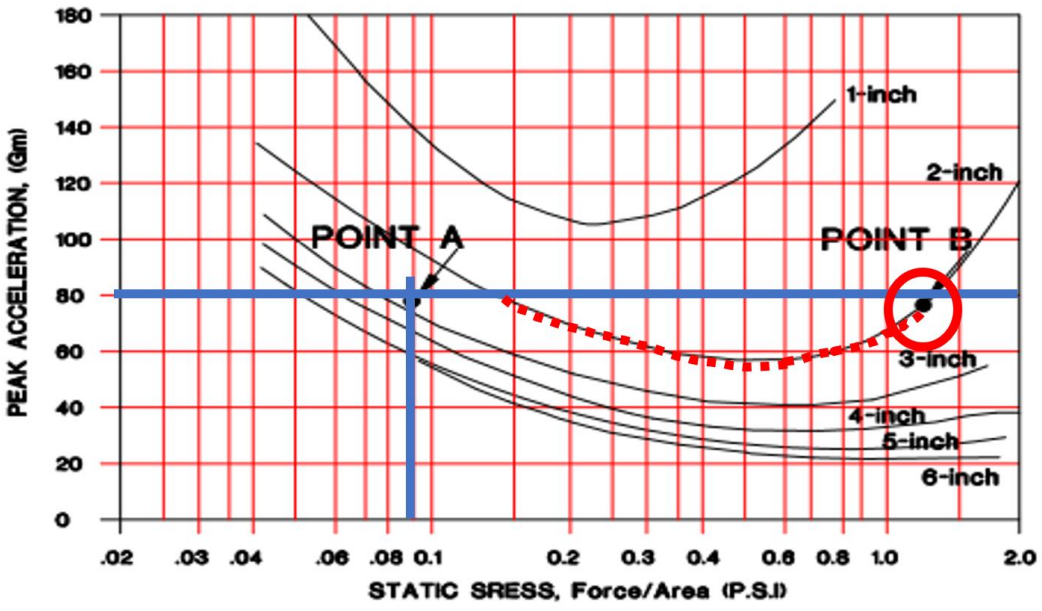

Figure 5-2: Cushioning curve for polyethylene (2pcf) foam, for drop-height of 750 mm [15]

From the above stated information regarding the item, the static stress is 0.09 psi. This qualifies the 3, 4 and 5-inch foams (below point A). However, if the static stress can be adjusted to be 1.25 PSI, the 2 and 6-inch foam can also be used (below point B). This can be done by using less foam to reduce the contact area to increase the static stress. The hexagonal array is also optimized to meet the above stated cushioning requirements without any adjustments to the contact area. Table 5-4 summarizes the user inputs (based

on the requirements), suitable conventional foam mass and thickness and optimized hexagonal array design variables, thickness and mass. The optimized hexagonal array is thinner and lighter than conventional cushions.

Table 5-4: Summary of case study 1

USER INPUT	CONVENTIONAL METHOD	OPTIMIZED HEXAGONAL ARRAY
Mass: 9 kg Contact area: 375 x 375 mm **G** ≤ 80 G **H**: 750 mm	No adjustments to area: L_y **= 76.2 mm** **Mass = 129 g** With adjustments to area: L_y **= 50.8 mm** **Mass = 16 g**	**t** = 69 nm **n** = 82 **R** = 1 **c** = 19 **L_y = 22.8 mm** **Mass = 2.77 g**

5.3.2 Case study 2

An item with a mass of 3.4 kg has a fragility value of 25 G. It requires a cushion with a contact area of 510 mm by 510 mm. The transportation mode of the item involves a risk of the packaging being dropped over a maximum height of 600 mm. After closely looking at various foams' cushion curves, the most suitable foams are as listed in Table 10. Similarly, the details regarding the optimized hexagonal array for this application is also listed Table 5-5.

Table 5-5: Summary of case study 2

USER INPUT	CONVENTIONAL METHOD	OPTIMIZED HEXAGONAL ARRAY
Mass: 3.4 kg Contact area: 510 x 510 mm **G** ≤ 25 G **H**: 600 mm	Polystyrene (1.5 pcf): **L_y = 76.2 mm** **Mass = 148 g** Polyurethane (1.5 pcf): **L_y = 76.2 mm** **Mass = 258 g** Polystyrene (2.5 pcf): **L_y = 101.6 mm** **Mass = 222 g** Polyurethane Ether (1.5 pcf): **L_y = 50.8 mm** **Mass = 315 g** Polyurethane Ether (2 pcf): **L_y = 50.8 mm** **Mass = 420 g**	**t** = 33 nm **n** = 90 **R** = 1 **c** = 10 **L_y = 58.9 mm** **Mass = 3.12 g**

The optimized hexagonal array for this application is slightly thicker than the thinnest conventional foam but significantly lighter than any of the conventional foams.

5.3.3 Case study 3

Running shoes comes with cushioning structure incorporated into its sole. Most shoes offer a shock absorption capacity where only 10 G is transmitted to the foot. Barefoot running with forefoot strike returns about 2.7 G instead. Most shoes have a cushioning thickness of about 20 mm and a mass of about 100 g to 300 g. Take an example where a man weighs 80 kg, a relatively rectangular foot profile of 362 mm by 97 mm and for every stride he makes, his feet free falls for about 100 mm. Given the above information, the hexagonal array can be optimized to meet these requirements as summarized in Table 5-6.

Table 5-6: Summary of case study 3

USER INPUT	CONVENTIONAL METHOD	OPTIMIZED HEXAGONAL ARRAY
Mass: 80 kg Contact area: 362 x 97 mm **G** ≤ 10 G **H**: 100 mm	**L_y ≈ 20 mm** **Mass ≈ 100 - 300 g**	**t** = 574 nm **n** = 56 **R** = 5.6 **c** = 70 **L_y = 19.6 mm** **Mass = 6.16 g**

The optimized hexagonal array has similar thickness to those conventional foams used in running shoes. However, it is significantly lighter which is a desirable property as it reduces the net weight of the running shoe which helps the runner to perform better.

5.4 SUMMARY

Conducting a drop test on PE foams demonstrates the increasing significance of the dynamic effect at increasing drop-heights. This signals the need for the dynamic factor to account for the dynamic effect. The dynamic factor is however not fully established. Due to resource limitations, the dynamic effect is acknowledged but not accounted for provided that the cushioning applications involve low drop-heights and cushions with high thicknesses.

The minimum point of cushioning curves corresponds to the densification point of the cushion i.e. the cushion returns the lowest $\boldsymbol{G}$ when compressed till $\boldsymbol{\varepsilon_d}$. This is consistent with the fact that the densification point is also the optimal design point of a cushion. To fully utilize a cushion, it must be optimized for a certain application based on this optimal design point. This eliminates the need for cushioning curve as only information on the densification point is required (i.e. $\boldsymbol{\varepsilon_d}$, $\boldsymbol{\sigma_d}$ and $\boldsymbol{W_d}$).

Optimized theoretical Hexagonal Arrays are superior to conventional cushions. For the cases presented in the previous section, the optimized Hexagonal Arrays are always lighter and at most, as thick as the corresponding conventional cushions. Physical manufacturing of these structures is not possible yet based on current technology.

CHAPTER 6 – CONCLUSIONS AND FUTURE WORK

This chapter serves as a summary of all the work performed for the completion of the thesis. Future work to further the subject area presented in the thesis is also proposed. Limitations associated with the research are discussed as well. Finally, published research writings by the author are listed.

6.1 CONCLUSIONS

A cellular structure design which properties can be independent of its relative density is developed for the first time. This is possible due to the design freedom offered by AM technologies allowing the design of a cellular structure that depart away from conventional design. A design framework for the novel cellular structure design for hexagonal cells (Hexagonal Array) was proposed to be incorporated with a parameter optimization process for cushioning purposes. The optimized structures were compared with conventional cushions serving the same purpose. Finally, new methods developed for the purpose of testing and characterization and cushion selection are summarized.

The key contributions of the research are elaborated in the following sections.

6.1.1 Polygonal/Polyhedral cellular array structure

Traditionally, relative density is always considered the main parameter dictating the properties of cellular structure. This limits the potential of cellular structures from achieving ultra-high specific strength and stiffness. However, with the novel polygonal/polyhedral cellular array structure design, the strength and stiffness can be improved while keeping the relative density and weight constant (Figure 4-16 and 4-17).

This is achieved by scaling down the unit cells (cellular refinement). The mechanisms responsible for this increase in strength and stiffness are size effect and the increase in the number of load bearing cell walls to the total number of cell walls. With cellular refinement, the number of cells in a design space increases and so will the number of cell walls. Since the outer cell walls do not bear any load, the ratio of load bearing cell walls to total number of cell walls increases.

In addition, the cellular array structure provides a wide range of controllable design parameters for fine tuning the structure to achieve the desired properties. It also makes it possible for unit cells to take up shapes which were not possible in conventional design. Applying the cellular array structure to produce functionally graded structure (FGS) is also feasible. For the first time, a FGS with constant relative density (Figure 6-1) can be design and fabricated.

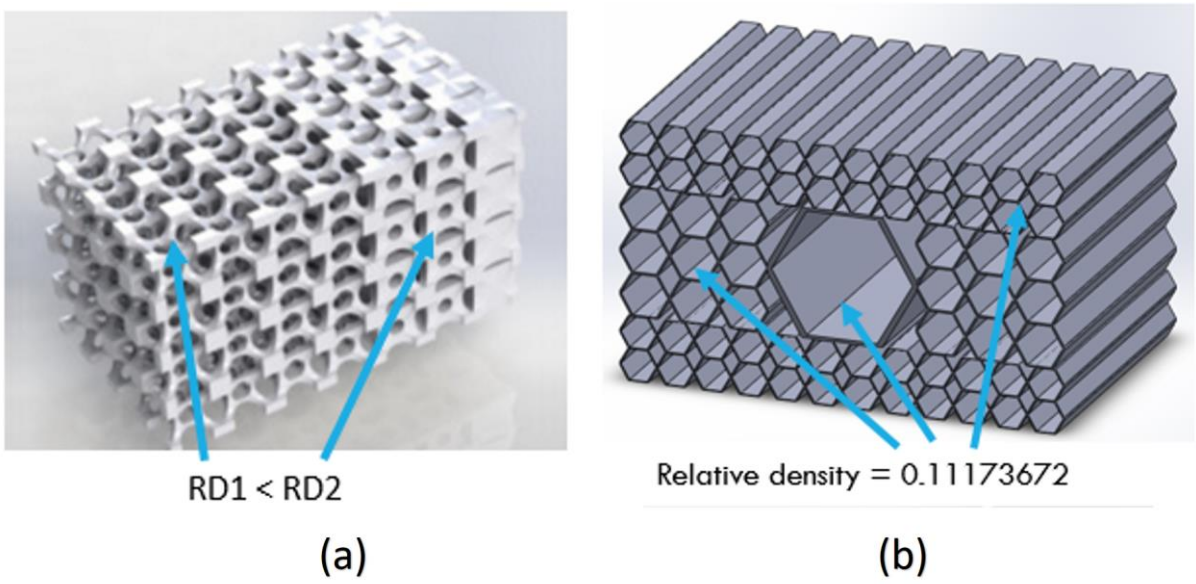

Figure 6-1(a): Conventional FGS with varying relative densities; (b) Constant relative density FGS designed with cellular arrays.

6.1.2 Parameter optimization of Hexagonal Array for cushioning

Six design variables were listed in Section 4.2 where four are optimizable. The two fixed variables are contact area (***A***) and material elastic modulus (E_s). That leaves the number of structural units (***c***), refinement factor (***n***), cell wall thickness (***t***) and cell slenderness (***R***) as optimizable variables.

The modelled compressive mechanical response of the Hexagonal Array is a function of all six design variables. The model is capable of predicting the compressive response accurately provided the actual densification strain (ε_d) is ≥ 0.55 with minimal cell wall tearing (Section 4.4).

The optimal strain for any cushioning structure is located at maximum energy absorption efficiency (W_{eff}) which is also ε_d, this strain value corresponds to the minimum point for all cushioning curves (Section 5.1). This eliminates the need for cushioning curves entirely and since ***G***-level for any static stress (σ_s) can be calculated using the static compression stress-strain data, only the data corresponding to the ε_d are relevant (i.e. ε_d, σ_d and W_d).

Since the stress-stain response can be modelled, the shock absorption capacity of a Hexagonal Array can be predicted by performing mathematical calculations with a combination of equations which are the functions of the six design variables. The accuracy however drops as the drop-height (***H***) increases and foam thickness (L_y) decreases.

The optimized Hexagonal Arrays for various cushioning requirements were compared to conventional cushioning solutions. The Hexagonal Arrays were found to be always lighter with comparable thickness.

Although 3D printing allows for customization at no added cost and time, in general it is more time consuming than conventional manufacturing methods. Therefore, the design freedom that 3D printing offers can be utilised to fabricate moulds or dies of optimized structures, so that these structures can be mass produced for many uses of the same application.

6.1.3 Methods Developed

Layering was introduced to control the polymeric composition of digital polymers (Section 3.2.1). Layering is however limited to 2D solid parts. An extended conditioning time is also required before layered parts can be used/tested.

Standardized methods were introduced and proposed for the purpose of identifying yield point, linear modulus ($\boldsymbol{E^*}$), plateau stress ($\boldsymbol{\sigma_p}$), plateau strain ($\boldsymbol{\varepsilon_p}$) and densification strain ($\boldsymbol{\varepsilon_d}$) from the compressive stress-strain response of cellular structures. Conventionally, there are various "standards" that can be used to identify these. The method proposed in this thesis idealizes the stress-strain response based on the amount of energy absorbed by performing an iterative process. The idealized curves were able to fit the actual stress-strain curves well.

Finally, a cushion selection method which does not involve cushioning curves was developed. This method assumes that the optimal design point of cushions is consistently located at $\boldsymbol{\varepsilon_d}$. The details were discussed in Section 6.1.2. The significance of this method is that the optimal cushioning conditions for any cushion can be predicted by performing a simple static compression test. However, there are still room for improvements in order to increase the accuracy of the predicted optimum $\boldsymbol{G}$ and static stress ($\boldsymbol{\sigma_s}$). As mentioned earlier, the accuracy decreases with increased drop-height ($\boldsymbol{H}$) and decreased cushion thickness ($\boldsymbol{L_y}$). This can be accounted for with a dynamic factor.

The dynamic factor accounts for $\boldsymbol{H}$ and $\boldsymbol{L_{y,}}$ and modified for the predicted values accordingly. However, more research is required to properly understand the dynamic factor.

6.2 FUTURE WORK

The following research areas are recommended for future work:

6.2.1 Determining the function defining dynamic factor

The dynamic factor mentioned in Section 2.3.3 helps improve our understanding on how drop height and thickness of a cushion affects the cushions shock absorption. Furthermore, it will make the extraction of the dynamic properties of a foam from their static stress-strain data more accurate.

The dynamic factor serves as an adjustment factor to account for the effect of drop-height and foam height. If the function that defines the dynamic factor is found to be universal i.e. applies for all types of foams and cellular solids, there will no longer be a need for cushion curves. This is a huge step forward in the field of cushioning design. It is a welcoming step as well with current 3D printing technologies capable of printing new cellular solids with wide range of structures. Dynamic tests will not be required for these cellular solids if the dynamic factor have been fully developed and found to be a universal function.

6.2.2 Projecting Hexagonal Arrays to polygonal/polyhedronal array structures

Only the hexagonal array was studied in this project. However, the design framework which the hexagonal array is based on (Section 4.1) allows it to be fitted with other types of polygons which may have different mechanical behaviour. The hexagonal array structure is classified as a polygonal cellular array structure in this research. Similarly, polyhedronal cellular array structures can also be designed, printed and tested. Polyhedrons are basically the three-dimensional version of a polygon. For example, a square is a polygon while a cube is a polyhedron. A polyhedral structure can be assumed

to be better than a polygonal one as its mechanical behaviour is less dependent on the loading direction.

6.2.3 Polygonal/Polyhedronal array structure for load bearing applications

For cushioning purposes, the property in question is the energy absorption efficiency. However, for load bearing applications, it is more straightforward. The stiffness and strength of the structure should be able to bear the designed load with only elastic deformation. It is shown that with cellular refinement, the stiffness and strength of the structure increases exponentially. Not only will structures of this type be designed to be stronger, it will also have a significantly lower weight.

6.2.4 Geometry effect on photopolymerization shrinkage

From Section 3.2.2, photopolymers are known to undergo shrinkage during photopolymerization resulting in residual stresses. However, it is not known how the geometry, or the shape affects this shrinkage. Several specimens are to be 3D printed and their printed dimensions are to be compared with the design dimensions. Non-destructive tests will also be involved in determining the residual stresses in each sample. C-factor should also be explored as a means to quantify the extent of shrinkage.

6.2.5 Cellular array structure with negative stiffness/negative poisson ratio

In Section 2.5, novel 3D printable structures with negative stiffness and negative poisson were listed. Adopting the unit cells of this structures into the array arrangement might offer further improvements in terms of lowering the weight of the structure. Investigation on the feasibility of doing so is highly encouraged.

6.3 LIMITATIONS

Some of the methods and theory presented in this research comes with its limitations which are presented in this section. The limitations are:

1. The mathematical model presented in Section 4.4 can only be applied to even refinement factors. Therefore, the hexagonal array structures can only have a refinement factor value which is even. An even refinement factor ensures that the number of cellular rows in the structure is even allowing it to buckle symmetrically thus validating the mathematical model.

2. Fabrication and tests of hexagonal arrays with higher refinement factors were not done due to the limitations in 3D printing of thin wall structures. However, as technology improves, it can be expected that these limitations will be overcome allowing the fabrication of hexagonal arrays with high refinement factors.

3. The hexagonal array can only be designed to take a form of a cube or cuboid. Currently, it is not possible to have a cylindrical hexagonal array without any incomplete cells.

6.4 LIST OF PUBLICATIONS

1. **S. Abdul Jalil**, S.M. Chou, K. Tai, *Controlling Polymer Digital Material Composition With Layering,* International Conference on Progress in Additive Manufacturing, Pro-AM 2016, Singapore, 16 – 19 May 2016
2. **S. Abdul Jalil,** A. Anwar, S.M. Chou, K. Tai, *Material Yield Strain Identification using Energy Absorption,* The Journal of Strain Analysis for Engineering Design
3. **S. Abdul Jalil,** S.M. Chou, K. Tai, *Simplified Method to Identify Compressive Stress-Strain Properties of Cellular Solids using Energy Method*, in preparation
4. **S. Abdul Jalil,** S.M. Chou, K. Tai, *3D printing of Novel Cellular Array Structure Capable of Achieving Ultra-High Strength to Weight Ratio*, in preparation
5. **S. Abdul Jalil,** S.M. Chou, K. Tai, *Mathematical Modelling of Hexagonal Cellular Array Structures*, in preparation

REFERENCES

1. Chua, C.K., Leong, K.F. and Lim, C.S., Rapid prototyping: principles and applications. 2010: World Scientific.
2. Yan, C., Hao, L., Hussein, A., Young, P. and Raymont, D., Advanced lightweight 316L stainless steel cellular lattice structures fabricated via selective laser melting. Materials & Design, 2014. 55: p. 533-541.
3. Vashishtha, V.K., Makade, R., and Mehla, N., Advancement of rapid prototyping in aerospace industry-a review. International Journal of Engineering Science and Technology, 2011. 3(3): p. 2486-2493.
4. Yeong, W.Y., Sudarmadji, N., Yu, H.Y., Chua, C.K., Leong, K.F., Venkatraman, S.S., Boey, Y.C.F. and Tan, L.P., Porous polycaprolactone scaffold for cardiac tissue engineering fabricated by selective laser sintering. Acta biomaterialia, 2010. 6(6): p. 2028-2034.
5. Barbas, A., Bonnet, A.S., Lipinski, P., Pesci, R., and Dubois, G., Development and mechanical characterization of porous titanium bone substitutes. Journal of the mechanical behavior of biomedical materials, 2012. 9: p. 34-44.
6. Naing, M.W., Chua, C.K., Leong, K.F. and Wang, Y., Fabrication of customised scaffolds using computer-aided design and rapid prototyping techniques. Rapid Prototyping Journal, 2005. 11(4): p. 249-259.
7. Heinl, P., Muller, L., Korner, C., Singer, R.F. and Muller, F.A., Cellular Ti–6Al–4V structures with interconnected macro porosity for bone implants fabricated by selective electron beam melting. Acta biomaterialia, 2008. 4(5): p. 1536-1544.

8. Bak, D., Rapid prototyping or rapid production? 3D printing processes move industry towards the latter. Assembly Automation, 2003. 23(4): p. 340-345.
9. Ready, S., Endicott, F., Whiting, G.L., Ng, T.N., Chow, E.M. and Lu, J., 3D printed electronics. in NIP & Digital Fabrication Conference. 2013. Society for Imaging Science and Technology.
10. Choi, S. and Cheung, H., A multi-material virtual prototyping system. Computer-Aided Design, 2005. 37(1): p. 123-136.
11. Yap, Y.L. and Yeong, W.Y., Additive manufacture of fashion and jewellery products: A mini review: This paper provides an insight into the future of 3D printing industries for fashion and jewellery products. Virtual and Physical Prototyping, 2014. 9(3): p. 195-201.
12. Ramon, O., Mizrahi, S., and Miltz, J., Mechanical properties and behavior of open cell foams used as cushioning materials. Polymer Engineering & Science, 1990. 30(4): p. 197-201.
13. Guoxing, L. and Yu, T.X., Energy Absorption of Structures and Materials, ed. G. Jones. 2003, Cambridge, England: Woodhead Publishing Limited.
14. Gibson, L.J. and Ashby, M.F., Cellular solids: structure and properties. 1997, Cambridge university press Cambridge.
15. Handbook, M.S., Package Cushioning Design. MILHDBK-304B. Test Methods (October 1978), 1978.
16. Frederick, E., Physiological and ergonomics factors in running shoe design. Applied ergonomics, 1984. 15(4): p. 281-287.
17. Shuaeib, F.M., Hamouda, A.M.S., Hamdan, M.M., Umar, R.R. and Hashmi, M.S.J., Motorcycle helmet: Part II. Materials and design issues. Journal of materials processing technology, 2002. 123(3): p. 422-431.

18. Daum, M., A simplified process for determining cushion curves: The stress-energy method. Proceedings from Dimensions, 2006. 2006.

19. Othman, A.R., Honeycomb. Wiley Encyclopedia of Composites.

20. Saraswathy, G., Gopalakrishnam G., Das, B.N., Radhakrishnanm G., and Pal, S., Development of polyurethane-based sheets by phase inversion method for therapeutic footwear applications: Synthesis, fabrication, and characterization. Journal of Applied Polymer Science, 2009. 111(5): p. 2387-2399.

21. Miltz, J. and Gruenbaum, G., Evaluation of Cushioning Properties of Plastic Foams From Compressive Measurements. Polymer Engineering and Science 1981. 21.

22. Meisel, N., Gaynore, A., Williams, C., and Guest, J., Multiple-material topology optimization of compliant mechanisms created via Polyjet 3d printing. in 24th Annual international solid freeform fabrication symposium an additive manufacturing conference. 2013.

23. Campbell, I., Bourell, D., and Gibson, I., Additive manufacturing: rapid prototyping comes of age. Rapid prototyping journal, 2012. 18(4): p. 255-258.

24. Singh, R., Process capability study of Polyjet printing for plastic components. Journal of mechanical science and technology, 2011. 25(4): p. 1011-1015.

25. Sá, A.M., Mello, V.M., Echavarria, K.R., and Covill, D., Adaptive voids. The Visual Computer, 2015. 31(6-8): p. 799-808.

26. Rosa, M.E., An introduction to solid foams. Philosophical Magazine Letters, 2008. 88(9-10): p. 637-645.

27. Shaw, J.A., Grummon, D.S., and Foltz, J., Superelastic NiTi honeycombs: fabrication and experiments. Smart Materials and Structures, 2007. 16(1): p. S170.

28. Bitzer, T., Honeycomb technology: materials, design, manufacturing, applications and testing. 2012: Springer Science & Business Media.

29. Pflug, J., Vangrimde, B., Verpoest, I., Bratfisch, P. and Vandepitte, D., Continuously produced honeycomb cores. in INTERNATIONAL SAMPE SYMPOSIUM AND EXHIBITION. 2003. SAMPE; 1999.

30. Papka, S.D. and Kyriakides, S., Experiments and full-scale numerical simulations of in-plane crushing of a honeycomb. Acta materialia, 1998. 46(8): p. 2765-2776.

31. Skochdopole, R., Foamed Plastics, Vol. 9. Encyclopedia of Chemical Technology, 1990.

32. Klempner, D. and Frisch, K.C., Handbook of polymeric foams and foam technology. Vol. 404. 1991: Hanser Munich etc.

33. LeMay, J.D., Hopper, R., Hrubeshm L.W. and Pekala, R.W., Low-Density Microcellular Materials: Introduction. MRS bulletin, 1990. 15(12): p. 19-20.

34. Liao, X., Zhang, H. and He, T., Preparation of porous biodegradable polymer and its nanocomposites by supercritical CO 2 foaming for tissue engineering. Journal of Nanomaterials, 2012. 2012: p. 6.

35. Banhart, J., Manufacture, characterisation and application of cellular metals and metal foams. Progress in materials Science, 2001. 46(6): p. 559-632.

36. Shapovalov, V., Porous metals. Mrs Bulletin, 1994. 19(4): p. 24-28.

37. Davies, G. and Zhen, S., Metallic foams: their production, properties and applications. Journal of Materials science, 1983. 18(7): p. 1899-1911.

38. Miyoshi, T., Materials Research Society, Symposium Proceedings, Volume 521. Porous and Cellular Materials for Structural Applications. 1998, MATERIALS RESEARCH SOCIETY WARRENDALE PA.

39. Queheillalt, D.T., Hass, D.D., Sypeck, D.J. and Wadley, H.N., Synthesis of open-cell metal foams by templated directed vapor deposition. Journal of Materials Research, 2001. 16(4): p. 1028-1036.

40. Cherevko, S., Xing, X. and Chung, C.H., Electrodeposition of three-dimensional porous silver foams. Electrochemistry Communications, 2010. 12(3): p. 467-470.

41. Banhart, J., Ashby, M. and Fleck, N., Metal foams and porous metal structures. in Conference on Metal Foams and Porous Metal Structures. 1999.

42. Miyoshi, T., Itoh, M., Akiyama, S. and Kitahara, A., ALPORAS aluminum foam: production process, properties, and applications. Advanced engineering materials, 2000. 2(4): p. 179-183.

43. Gallego, N.C. and Klett, J.W., Carbon foams for thermal management. Carbon, 2003. 41(7): p. 1461-1466.

44. Ashby, M. and Medalist, R., The mechanical properties of cellular solids. Metallurgical and Materials Transactions A, 1983. 14(9): p. 1755.

45. Maiti, S., Gibson, L. and Ashby, M., Deformation and energy absorption diagrams for cellular solids. Acta metallurgica, 1984. 32(11): p. 1963-1975.

46. Gibson, L.J., Ashby, M., Schajer, G.S. and Robertson, C.I., The mechanics of two dimensional cellular materials. in Proceedings of the Royal Society of London A: Mathematical, Physical and Engineering Sciences. 1982. The Royal Society.

47. Finnie, I. and Patel, M., Structural features and mechanical properties of rigid cellular plastics(Rigid cellular plastics mechanical properties based on model assuming pentagonal dodecahedron cell form). Journal of Materials, 1970. 5: p. 909-932.

48. Menges, G. and Knipschild, F., Estimation of mechanical properties for rigid polyurethane foams. Polymer Engineering & Science, 1975. 15(8): p. 623-627.

49. Gibson, L.J. and Ashby, M., The mechanics of three-dimensional cellular materials. in Proceedings of the Royal Society of London A: Mathematical, Physical and Engineering Sciences. 1982. The Royal Society.

50. Li, Q., Magkiriadis, I. and Harrigan, J., Compressive strain at the onset of densification of cellular solids. Journal of cellular plastics, 2006. 42(5): p. 371-392.

51. Gent, A. and Thomas, A.G., The deformation of foamed elastic materials. Journal of Applied Polymer Science, 1959. 1(1): p. 107-113.

52. Cote, F., Deshpande, V.S., Fleck, N.A and Evans, A.G., The out-of-plane compressive behavior of metallic honeycombs. Materials Science and Engineering: A, 2004. 380(1): p. 272-280.

53. Zhang, J. and Ashby, M., The out-of-plane properties of honeycombs. International Journal of Mechanical Sciences, 1992. 34(6): p. 475-489.

54. Xu, S., Beynon, J.H., Ruan, D. and Lu, G., Experimental study of the out-of-plane dynamic compression of hexagonal honeycombs. Composite Structures, 2012. 94(8) p. 2326-2336.

55. László, O., Lajos, B. and Tibor, C., Investigation of highly porous poly (ECaprolactone) scaffolds. Biomechanica Hungarica, 2008. 1(1).

56. Ashby, M.F., The Properties of Foams and Lattices. Philosophical Transactions: Mathematical, Physical and Engineering Sciences, 2006. 364(1838): p. 15-30.

57. Avalle, M., Belingardi, G. and Ibba, A., Mechanical models of cellular solids: parameters identification from experimental tests. International Journal of Impact Engineering, 2007. 34(1): p. 3-27.

58. Instituition, B.S., ISO 13314: Mechanical testing of metals – Ductility testing – Compression test for porous and cellular metals. 2011.

59. Nieh, T., Higashi, K. and Wadsworth, J., Effect of cell morphology on the compressive properties of open-cell aluminum foams. Materials Science and Engineering: A, 2000. 283(1): p. 105-110.

60. Paul, A. and Ramamurty, U., Strain rate sensitivity of a closed-cell aluminum foam. Materials Science and Engineering: A, 2000. 281(1): p. 1-7.

61. Chan, K. and Xie, L., Dependency of densification properties on cell topology of metal foams. Scripta Materialia, 2003. 48(8): p. 1147-1152.

62. Vural, M. and Ravichandran, G., Microstructural aspects and modeling of failure in naturally occurring porous composites. Mechanics of Materials, 2003. 35(3): p. 523536.

63. Tan, P., Harrigan, J. and Reid, S., Inertia effects in uniaxial dynamic compression of a closed cell aluminium alloy foam. Materials science and technology, 2002. 18(5): p. 480-488.

64. Bai, C., Franchinm G., Elsayed, H., Zaggia, A., Conte, L., Li, H. and Colombo, P., High-porosity geopolymer foams with tailored porosity for thermal insulation and wastewater treatment. Journal of Materials Research, 2017: p. 1-9.

65. Zhang, J. and Ashby, M., Mechanical selection of foams and honeycombs used for packaging and energy absorption. Journal of Materials Science, 1994. 29(1): p. 157163.

66. Weder, D.E., Packaging material. 1999, Google Patents.

67. Koike, M., Cushioning material for packaging and packaging matter. 2003, Google Patents.

68. Garland, M.G., Santer, M.J. and Morrison, J.F., Optimal aero-structural design of an adaptive surface for boundary layer motivation using an auxetic lattice skin. Journal of Intelligent Material Systems and Structures, 2017: p. 1045389X16685446.

69. Farooq, U., Ahman, M.S., Rakha, S.A., Ali, N., Khurram, A.A. and Subhani, T., Interfacial Mechanical Performance of Composite Honeycomb Sandwich Panels for Aerospace Applications. Arabian Journal for Science and Engineering, 2017. 42(5): p. 1775-1782.

70. Cellucci, D., Jenett, B. and Cheung, K.C., Digital cellular solid pressure vessels: A novel approach for human habitation in space. in Aerospace Conference, 2017 IEEE. 2017. IEEE.

71. Goode, D.P., Lateral or transverse flex sports board. 2017, Google Patents.

72. Nakamoto, I.L., Inflatable water self-rescue and carrying device. 2017, Google Patents.

73. Svagan, A.J., Müllertz, A. and Löbmann, K., Floating solid cellulose nanofibre nanofoams for sustained release of the poorly soluble model drug furosemide. Journal of Pharmacy and Pharmacology, 2017. 69(11): p. 1477-1484.

74. Bendsøe, M.P. and Sigmund, O., Topology optimization by distribution of isotropic material, in Topology Optimization. 2004, Springer. p. 1-69.

75. Lakes, R.S., Negative-Poisson's-Ratio Materials: Auxetic Solids. Annual Review of Materials Research, 2017(0).

76. Zorzetto, L. and Ruffoni, D., Re-entrant inclusions in cellular solids: From defects to reinforcements. Composite Structures, 2017. 176(Supplement C): p. 195-204.

77. Mojzes, A., Földesi, P., and Böröcz, P., Define cushion curves for environmental friendly packaging foam. Annals of the Faculty of Engineering Hunedoara, 2012. 10(1): p. 113.

78. Avalle, M., Belingardi, G. and Montanini, R., Characterization of polymeric structural foams under compressive impact loading by means of energy-absorption diagram. International Journal of Impact Engineering, 2001. 25(5): p. 455-472.

79. Aguinaldo, A. and Mahar, A., Impact loading in running shoes with cushioning column systems. Journal of applied biomechanics, 2003. 19(4): p. 353-360.

80. Baldwin, B.B. and Higgins, H., Gymnastic mat. 1979, Google Patents.

81. Bassette, A.B. and Durr, N., Sports helmet. 1998, Google Patents.

82. De Luca, N.P., Reyes, O.M. and Jacques, P.M., Inflatable, cushioning, bubble wrap product having multiple, interconnected, bubble structures. 2002, Google Patents.

83. Wosk, J. and Voloshin, A.S., Low back pain: conservative treatment with artificial shock absorbers. Archives of physical medicine and rehabilitation, 1985. 66(3): p. 145-148.

84. Belbasis, A.F., Fuss, F.K., Van Den Hazel, B. and Schlegel, M., Foam mechanics: evaluating performance based on energy absorption at optimal strain, in 2014 International Conference in Sports Science & Technology (ICSST). 2014: Singapore.

85. Corporation, S.C. Dynamic Cushioning Curve. 2010; Available from: http://cybercase.com/custom-interiors-2.htm.

86. Sek, M.A., Minett, M., Rouillard, V. and Bruscella, B., A new method for the determination of cushion curves. Packaging Technology and Science, 2000. 13(6): p. 249-255.

87. Gruenbaum, G. and Miltz, J., Static versus dynamic evaluation of cushioning properties of plastic foams. Journal of Applied Polymer Science, 1983. 28(1): p. 135.

88. Hyun, S. and Torquato, S., Optimal and manufacturable two-dimensional, Kagome-like cellular solids. Journal of Materials Research, 2002. 17(1): p. 137-144.

89. Bendsøe, M.P. and Kikuchi, N., Generating optimal topologies in structural design using a homogenization method. Computer methods in applied mechanics and engineering, 1988. 71(2): p. 197-224.

90. Sigmund, O. and Torquato, S., Design of materials with extreme thermal expansion using a three-phase topology optimization method. Journal of the Mechanics and Physics of Solids, 1997. 45(6): p. 1037-1067.

91. Bulman, S., Sienz, J. and Hinton, E., Comparisons between algorithms for structural topology optimization using a series of benchmark studies. Computers & Structures, 2001. 79(12): p. 1203-1218.

92. Rozvany, G.I., Zhou, M. and Birker, T., Generalized shape optimization without homogenization. Structural and Multidisciplinary Optimization, 1992. 4(3): p. 250-252.

93. Zhang, W. and Sun, S., Scale-related topology optimization of cellular materials and structures. International Journal for numerical methods in Engineering, 2006. 68(9): p. 993-1011.

94. Tantikom, K., Aizawa, T. and Mukai, T., Symmetric and asymmetric deformation transition in the regularly cell-structured materials. Part I: experimental study. International Journal of Solids and Structures, 2005. 42(8): p. 2199-2210.

95. Burgueño, R., Quagliata, M.J., Mohanty, A.K., Mehta, G., Drzal, L.T. and Misra, M., Hierarchical cellular designs for load-bearing biocomposite beams and plates. Materials Science and Engineering: A, 2005. 390(1): p. 178-187.

96. Bauer, J., Hengsbach, S., Tesari, I., Schwaiger, R. and Kraft, O., High-strength cellular ceramic composites with 3D microarchitecture. Proceedings of the National Academy of Sciences, 2014. 111(7): p. 2453-2458.

97. Onck, P., Andrews, E. and Gibson, L., Size effects in ductile cellular solids. Part I: modeling. International Journal of Mechanical Sciences, 2001. 43(3): p. 681-699.

98. Brackett, D., Ashcroft, I. and Hague, R., Topology optimization for additive manufacturing. in Proceedings of the Solid Freeform Fabrication Symposium, Austin, TX. 2011.

99. Gill, S. and Kaplas, M., Efficacy of powder-based three-dimensional printing (3DP) technologies for rapid casting of light alloys. The International Journal of Advanced Manufacturing Technology, 2011. 52(1-4): p. 53-64.

100. Masood, S.H. and Song, W.Q., Development of new metal/polymer materials for rapid tooling using Fused deposition modelling. Materials & Design, 2004. 25(7): p. 587594.

101. Choi, S.H. and Chueng, H.H., A multi-material virtual prototyping system. Computer Aided Design, 2005. 37(1): p. 123-136.

102. Liou, F., Rapid Prototyping and Engineering Applicaons. 1st Edi on. New York: CRC Press Taylor and Francis Group, 2008.

103. Correa, D.M., Klatt, T., Cortes, S., Haberman, M., Kovar, D. and Seepersad, C., Negative stiffness honeycombs for recoverable shock isolation. Rapid Prototyping Journal, 2015. 21(2): p. 193-200.

104. Kashdan, L., Seepersad, C., Haberman, M. and Wilson, P.S., Design, fabrication, and evaluation of negative stiffness elements using SLS. Rapid Prototyping Journal, 2012. 18(3): p. 194-200.

105. Duoss, E.B., Weisgraber, T.H., Hearon, K., Zhu, C., Small IV, W., Metz, T.R. Vericella, J.J., Barthm H.D., Kuntz, J.D., Maxwell, R.S. amd Spadaccini, C.M., Three dimensional printing of elastomeric, cellular architectures with negative stiffness. Advanced Functional Materials, 2014. 24(31): p. 4905-4913.

106. Clausen, A., Wang, F., Jensen, J.S., Sigmund, O. and Lewis, J.A., Topology optimized architectures with programmable Poisson's ratio over large deformations. Advanced Materials, 2015. 27(37): p. 5523-5527.

107. Schumacher, C., Bickel, B., Rys, J., Marschner, S., Darajo, C. and Gross, M., Microstructures to control elasticity in 3D printing. ACM Transactions on Graphics (TOG), 2015. 34(4): p. 136.

108. Maiti, A., Small, W., Lewicki, J.P., Weisgraber, T.H., Duoss, E.B., Chinn, S.C., Pearson, M.A., Spadaccini, C.M., Maxwell, R.S. and Wilson, T.S., 3D printed

cellular solid outperforms traditional stochastic foam in long-term mechanical response. Scientific reports, 2016. 6: p. 24871.

109. Zelený, P., Šafka, J. and Elkina, I.,The Mechanical Characteristics of 3D Printed Parts According to the Build Orientation. in Applied Mechanics and Materials. 2014. Trans Tech Publ.

110. Stratasys. Polyjet Materials. 2015; Available from: http://www.stratasys.com/materials/Polyjet.

111. Barclift, M.W. and Williams, C.B., Examining variability in the mechanical properties of parts manufactured via Polyjet direct 3D printing. in International Solid Freeform Fabrication Symposium. 2012.

112. Cazón, A., Morer, P. and Matey, L., Polyjet technology for product prototyping: Tensile strength and surface roughness properties. Proceedings of the Institution of Mechanical Engineers, Part B: Journal of Engineering Manufacture, 2014. 228(12): p. 1664-1675.

113. Blanco, D., Fernandez, P. and Noriega, A., Nonisotropic experimental characterization of the relaxation modulus for Polyjet manufactured parts. Journal of Materials Research, 2014. 29(17): p. 1876-1882.

114. Abdul Jalil, S., Chou, S.M. and Tai, K., Controlling Polymer Digital Material Composition With Layering. 2016.

115. Brajlih, T., Drstvensek, I., Kovacic, M. and Balic, J., Optimizing scale factors of the Polyjet™ rapid prototyping procedure by genetic programming. Journal of achievements in materials and manufacturing engineering, 2006. 16(1-2): p. 101-106.

116. Ishikiriama, S.K., Valeretto, T.M., Franco, E.B. and Mondelli, R.F.L., The influence of" C-factor" and light activation technique on polymerization

contraction forces of resin composite. Journal of Applied Oral Science, 2012. 20(6): p. 603-606.

117. Yang, H., Lim, J.C., Liu, Y., Qi, X., Yap, Y.L., Dikshit, V., Yeong, W.Y. amd Wei, J., Performance evaluation of projet multi-material jetting 3D printer. Virtual and Physical Prototyping, 2017. 12(1): p. 95-103.
118. ISO, ISO 527-2: Plastics - Determination of Tensile Properties. Test conditions for moulding and extrusion. 2012.
119. ISO, ISO 37: Rubber, vulcanized or thermoplastic — Determination of tensile stressstrain properties. 2017.
120. Tran, R. Recommended Wall Thickness for 3D Printing. fictiv 2016; Available from: https://www.fictiv.com/hwg/fabricate/recommended-wall-thickness-for-3d-printing.
121. Cameron, M. Design for 3D printing: advice from a Stratasys applications engineer. GrabCAD Blog 2016; Available from: http://blog.grabcad.com/blog/2016/05/11/design-for-3d-printing-advice/.
122. Dowling, N.E., Mechanical behavior of materials: engineering methods for deformation, fracture, and fatigue. 2012: Pearson.
123. Bird, J., Ross, C. and Little, A., Mechanics of solids. 2016: Routledge.
124. Bhavikatti, S., Mechanics of solid. 2010: New Age International.
125. Dieter, G.E. and Bacon, D.J., Mechanical metallurgy. Vol. 3. 1986: McGraw-hill New York.
126. Chajes, A., Principles of structural stability theory. 1974: Prentice Hall.
127. Construction, A., Steel Construction Manual. 2005, United State: AISC.

128. Vollertsen, F., Biermann, D., Hansen, H.N., Jawahir, I.S. and Kuzman, K., *Size effects in manufacturing of metallic components.* CIRP annals, 2009. **58**(2): p. 566-587.

129. Nikolov, S., Han, C.S. and Raabe, D., *On the origin of size effects in small-strain elasticity of solid polymers.* International Journal of Solids and structures, 2007. **44**(5): p. 1582-1592.

APPENDIX A – TENSILE TESTS OF 3D PRINTED POLYMERS

Tensile test on 3D printed digital polymer with 50% VeroClearTM and 50% TangoPlusTM based on ISO 527 and ISO 37 standards.

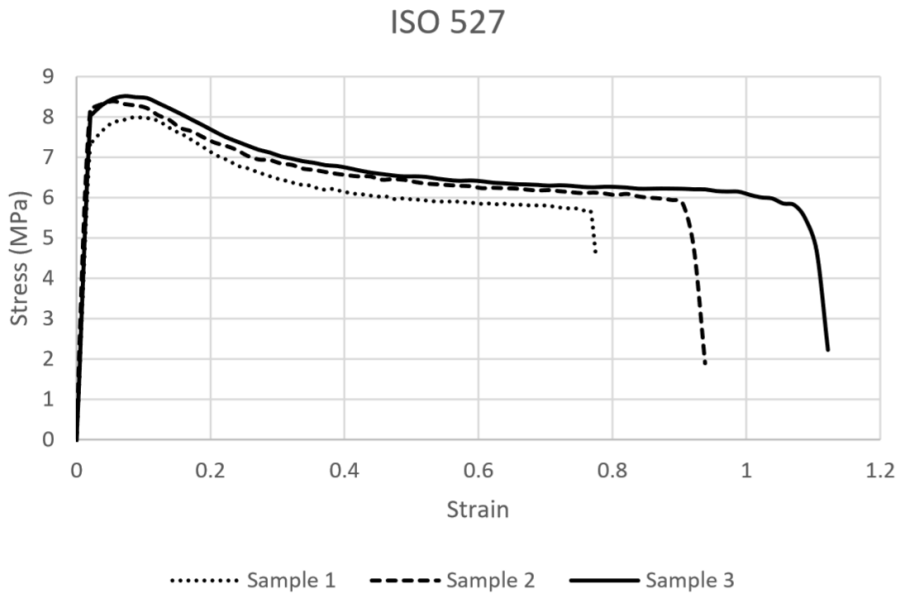

Figure A-1: ISO 527 stress-strain curve

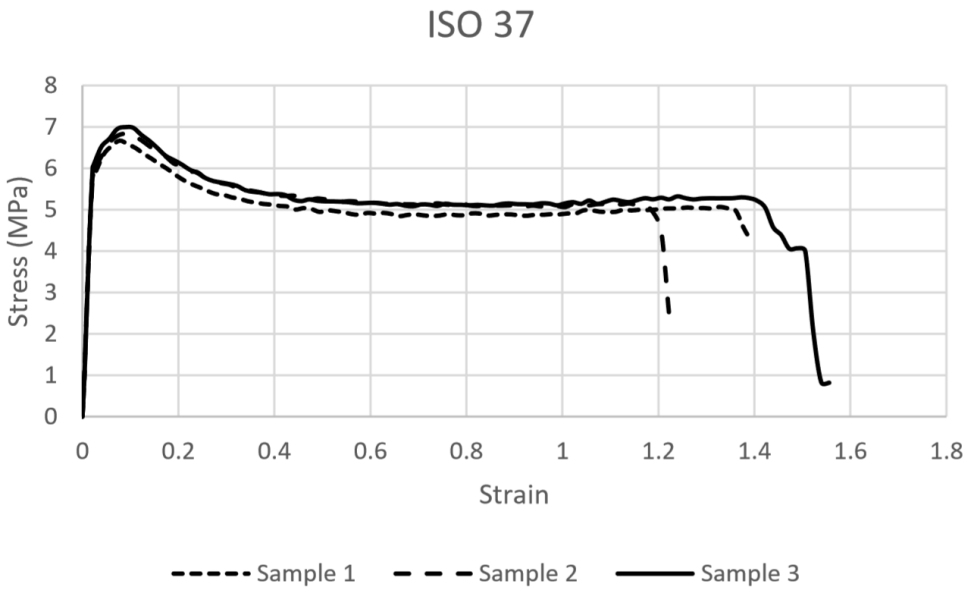

Figure A-2: ISO 37 stress-strain curve

Table A-1: Tabulated Results

Specimen Type / Specimen No.	ISO 527		ISO 37	
	UTS (MPa)	E (MPa)	UTS (MPa)	E (MPa)
1	7.991	391.942	6.666	285.602
2	8.391	414.192	6.835	277.050
3	8.518	397.450	6.993	300.985
Mean	8.300	391.487	6.831	287.879
Standard Deviation	0.275	11.588	0.134	9.903
Coefficient of Variation (%)	3.31	2.89	1.96	3.44

Table A-2: T-test (assuming equal variance) for the elastic moduli of ISO 527 and 37

	Elastic Modulus (MPa)	
	ISO 527	***ISO 37***
Mean	391.487	287.879
Variance	686.486	147.106
Observations	3	3
Pooled Variance	416.796	-
Hypothesized Mean Difference	0	-
Df	4	-
t Stat	6.215498	-
P(T<=t) one-tail	0.001705	-
t Critical one-tail	2.131847	-
P(T<=t) two-tail	0.00341	-
t Critical two-tail	2.776445	-

t Stat < -t Critical two-tail or ***t Stat > t Critical two-tail*** *=> null hypothesis rejected (insignificant difference between the elastic modulus of ISO 527 and ISO 37).* ***Therefore, the difference between the elastic modulus of ISO 527 and ISO 37 is statistically significant.***

Table A-3: T-test (assuming equal variance) for the ultimate tensile strength of ISO 527 and 37

	Ultimate Tensile Strength (MPa)	
	ISO 527	***ISO 37***
Mean	8.300	6.831
Variance	0.076	0.027
Observations	3	3
Pooled Variance	0.0511	-
Hypothesized Mean Difference	0	-
df	4	-
t Stat	7.953864	-
P(T<=t) one-tail	0.000677	-
t Critical one-tail	2.131847	-
P(T<=t) two-tail	0.001353	-
t Critical two-tail	2.776445	-

t Stat < -t Critical two-tail or t Stat > t Critical two-tail => null hypothesis rejected (insignificant difference between the ultimate tensile strength of ISO 527 and ISO 37). ***Therefore, the difference between the ultimate tensile strength of ISO 527 and ISO 37 is statistically significant***

Table A-4: Tabulated results (conditioned 16 hours)

Specimen Type / Specimen No.	Conditioned for 16 hours			
	Layered (100% **VeroClear™**)		Non-layered (100% **VeroClear™**)	
	UTS (MPa)	E (GPa)	UTS (MPa)	E (GPa)
1	49.058	1.877	52.621	2.041
2	46.625	1.780	52.073	1.849
3	46.017	1.625	52.360	1.959
Mean	47.233	1.760	52.352	1.950
Standard Deviation	1.609	0.127	0.274	0.096
Coefficient of Variation (%)	3.41	7.22	0.52	4.92

Table A-5: Tabulated results (conditioned 16 hours + 7 days)

Specimen Type / Specimen No.	Conditioned for 16 hours + 7 days			
	Layered (100% **VeroClear™**)		Non-layered (100% **VeroClear™**)	
	UTS (MPa)	E (GPa)	UTS (MPa)	E (GPa)
1	58.129	2.173	57.563	2.149
2	57.084	2.093	54.725	2.136
3	58.431	2.211	57.563	1.951
Mean	57.881	2.159	55.325	2.079
Standard Deviation	0.577	0.049	1.638	0.091
Coefficient of Variation (%)	1.00	2.27	2.96	4.38

Table A-6: T-test (assuming unequal variances) for the ultimate tensile strength of layered and non-layered specimens conditioned for 16 hours

	Ultimate Tensile Strength (MPa) – Conditioned for 16 hours	
	Layered	***Non-layered***
Mean	47.23333	52.35133
Variance	2.589472	0.075132
Observations	3	3
Hypothesized Mean Difference	0	-
df	2	-
t Stat	-5.43056	-
P(T<=t) one-tail	0.016138	-
t Critical one-tail	2.919986	-
P(T<=t) two-tail	0.032276	-
t Critical two-tail	4.302653	-

t Stat < -t Critical two-tail or t Stat > t Critical two-tail => null hypothesis rejected (insignificant difference between the ultimate tensile strength of ISO 527 and ISO 37). ***Therefore, the difference between the ultimate tensile strength of layered specimens and non-layered specimens conditioned for 16 hours is statistically significant.***

Table A-7: T-test (assuming equal variances) for the elastic modulus of layered and non-layered specimens conditioned for 16 hours

	Ultimate Tensile Strength (MPa) – Conditioned for 16 hours	
	Layered	***Non-layered***
Mean	47.23333	52.35133
Variance	2.589472	0.075132
Observations	3	3
Hypothesized Mean Difference	0	-
df	2	-
t Stat	-5.43056	-
P(T<=t) one-tail	0.016138	-
t Critical one-tail	2.919986	-
P(T<=t) two-tail	0.032276	-
t Critical two-tail	4.302653	-

t Stat < -t Critical two-tail or t Stat > t Critical two-tail => null hypothesis rejected (insignificant difference between the ultimate tensile strength of ISO 527 and ISO 37). ***Therefore, the difference between the ultimate tensile strength of layered specimens and non-layered specimens conditioned for 16 hours is statistically significant.***

Table A-8: T-test (assuming unequal variances) for the ultimate tensile strength of layered and non-layered specimens conditioned for 16 hours + 7 days.

	Ultimate Tensile Strength (MPa) – Conditioned for 16 hours + 7 days	
	Layered	***Non-layered***
Mean	57.88133	56.617
Variance	0.499606	2.684748
Observations	3	3
Hypothesized Mean Difference	0	-
df	3	-
t Stat	1.227189	-
P(T<=t) one-tail	0.153635	-
t Critical one-tail	2.353363	-
P(T<=t) two-tail	0.30727	-
t Critical two-tail	3.182446	-

t Stat < -t Critical two-tail or t Stat > t Critical two-tail => null hypothesis rejected (insignificant difference between the ultimate tensile strength of layered and non-layered specimens conditioned for 16 hours +7 days). ***Therefore, the difference between the ultimate tensile strength of layered specimens and non-layered specimens conditioned for 16 hours + 7 days is statistically insignificant.***

Table A-9: T-test (assuming unequal variances) for the elastic modulus of layered and non-layered specimens conditioned for 16 hours + 7 days

	Elastic Modulus (GPa) – Conditioned for 16 hours + 7 days	
	Layered	***Non-layered***
Mean	2.159	2.078667
Variance	0.003628	0.012266
Observations	3	3
Hypothesized Mean Difference	0	-
df	3	-
t Stat	1.10366	-
P(T<=t) one-tail	0.17516	-
t Critical one-tail	2.353363	-
P(T<=t) two-tail	0.35032	-
t Critical two-tail	3.182446	-

t Stat < -t Critical two-tail or t Stat > t Critical two-tail => null hypothesis rejected (insignificant difference between the elastic modulus of layered and non-layered specimens conditioned for 16 hours +7 days). ***Therefore, the difference between the elastic modulus of layered specimens and non-layered specimens conditioned for 16 hours + 7 days is statistically insignificant.***

APPENDIX B – DERIVATION OF THE EQUATION DEFINING RELATIVE DENSITY OF HEXAGONAL ARRAYS AS A FUNCTION OF t and L_x

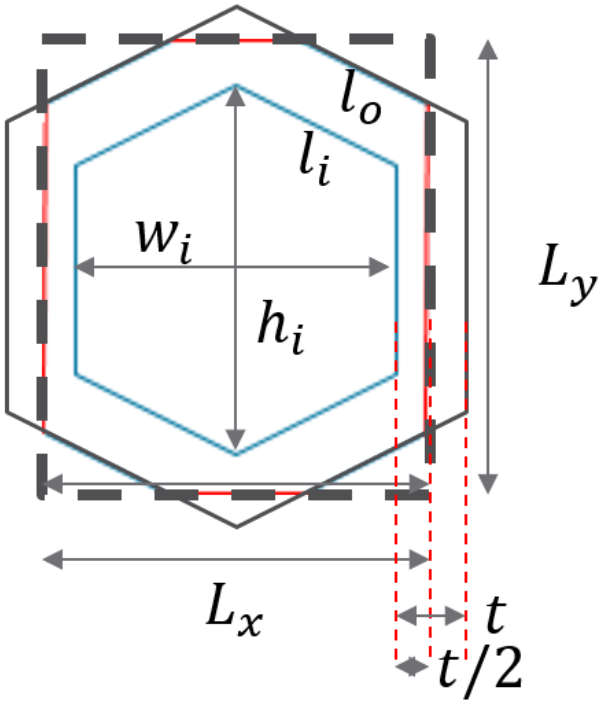

The hexagonal array unit cell can be seen as a snipped version of the generic hexagonal unit cell. For such unit cells, the cross-sectional area is the area of the outer hexagon (subscript 'o') minus the area of the inner hexagon (subscript 'i'). For the adjusted unit cell, the area is the above minus the areas of the sections outside the dotted box. The derivation for this area is follows:

$$w_i = L_x - t$$

$$l_i = \frac{L_x - t}{\sqrt{3}}$$

$$l_o = \frac{L_x + t}{\sqrt{3}}$$

$$h_i = 2l_i = \frac{L_x - t}{\sqrt{3}}$$

$$h_o = 2l_o = \frac{L_x + t}{\sqrt{3}}$$

$$L_y = h_i + \frac{h_o - h_i}{2} = \frac{2L_x}{\sqrt{3}}$$

Area of hexagon:

$$A = L_y L_x = \frac{2L_x^2}{\sqrt{3}}$$

Area of inner hexagon:

$$A_i = \frac{\sqrt{3}(L_x - t)^2}{2}$$

Area of outer hexagon:

$$A_o = \frac{\sqrt{3}(L_x + t)^2}{2}$$

Area of standard hexagonal unit cell:

$$A_H = A_i - A_o = 2\sqrt{3}L_x t$$

To obtain the area of the adjusted hexagonal unit cell, areas of the side sections and top and bottom tip sections needs to be deducted from $\boldsymbol{A_H}$.

Area of side sections (total):

$$A_{side} = 2\left[0.5 * \left(2l_o + \frac{t}{\sqrt{3}}\right) * \frac{t}{2}\right] = \frac{t}{2\sqrt{3}}(2L_x + 3t)$$

Area of top and bottom tips (total):

$$A_{tip} = 2\left[0.5 * 2t * \left(\frac{h_o - h_i}{4}\right)\right] = \frac{2t^2}{\sqrt{3}}$$

Recall relative density can be calculated as follows:

$$R.d = \frac{\rho^*}{\rho} = \frac{m/V^*}{m/V} = \frac{V}{V^*}$$

where superscript * denotes apparent values i.e. apparent density, apparent volume.

Since the hexagonal array is considered as a 2D structure where the cross-sectional area is constant along one axis, relative density can therefore be calculated as:

$$\boldsymbol{R.d = \frac{A}{A^*} = \frac{A_H - A_{side} - A_{tip}}{A^*} = 2.5\frac{t}{L_x} - 1.75\left(\frac{t}{L_x}\right)^2}$$

APPENDIX C – EXPERIMENTAL RESULTS OF CELLULAR STRUCTURES

Static compression test results (3D printed hexagonal array - TangoBlack™)

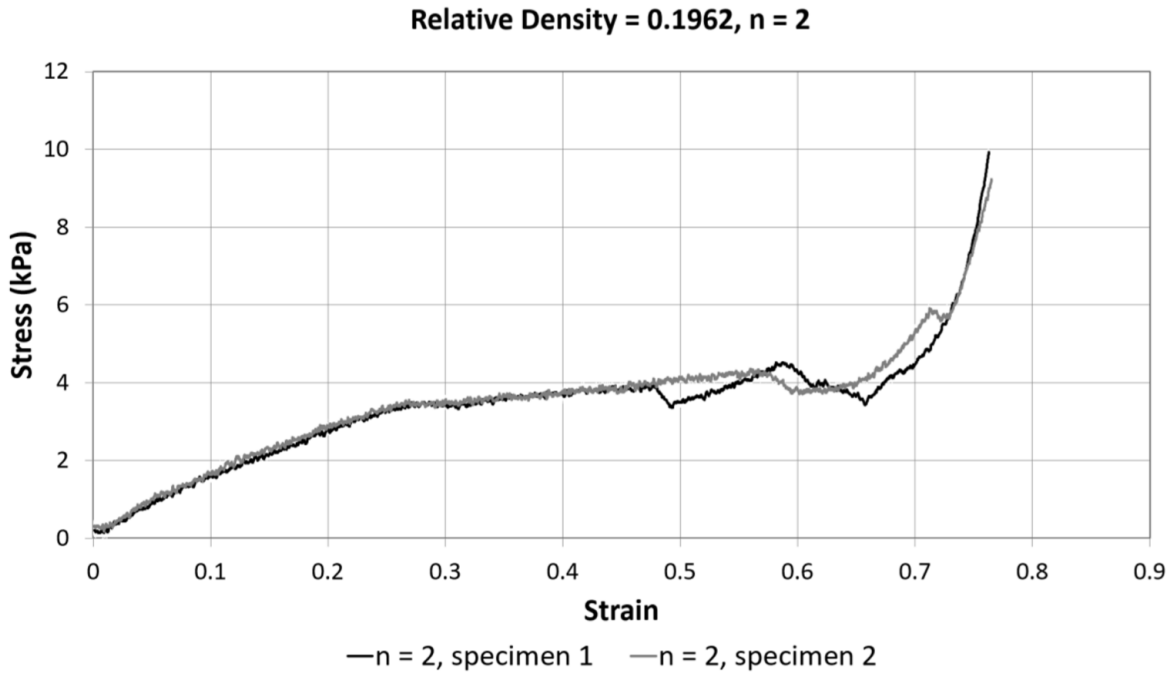

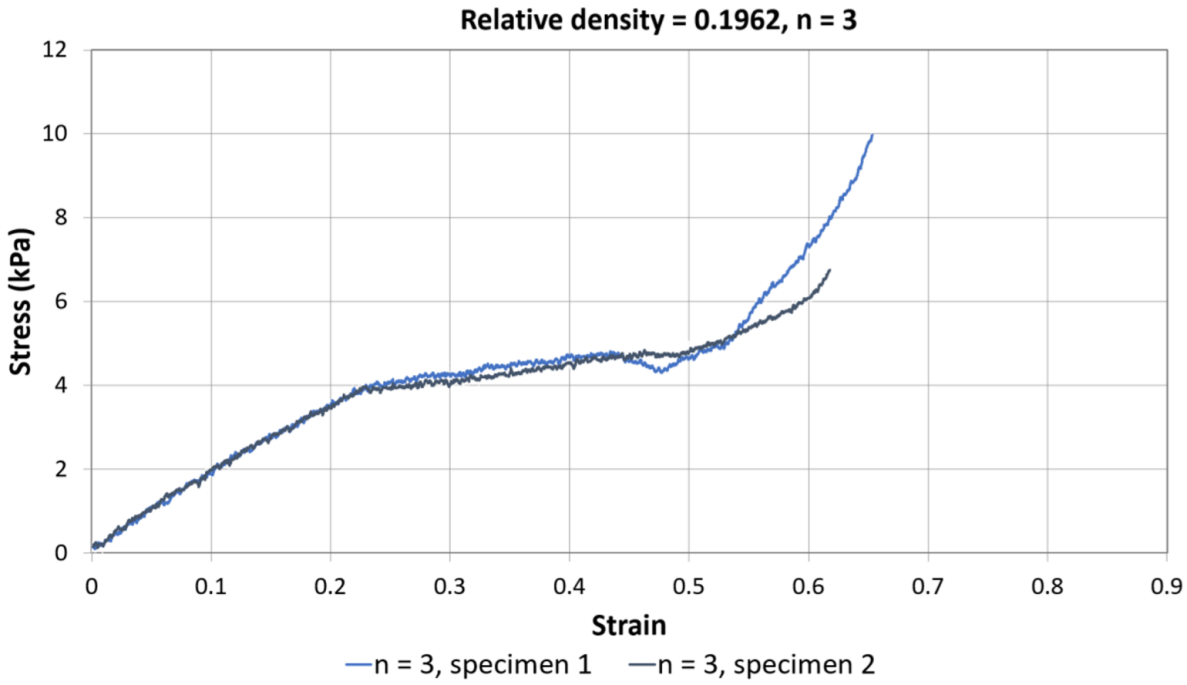

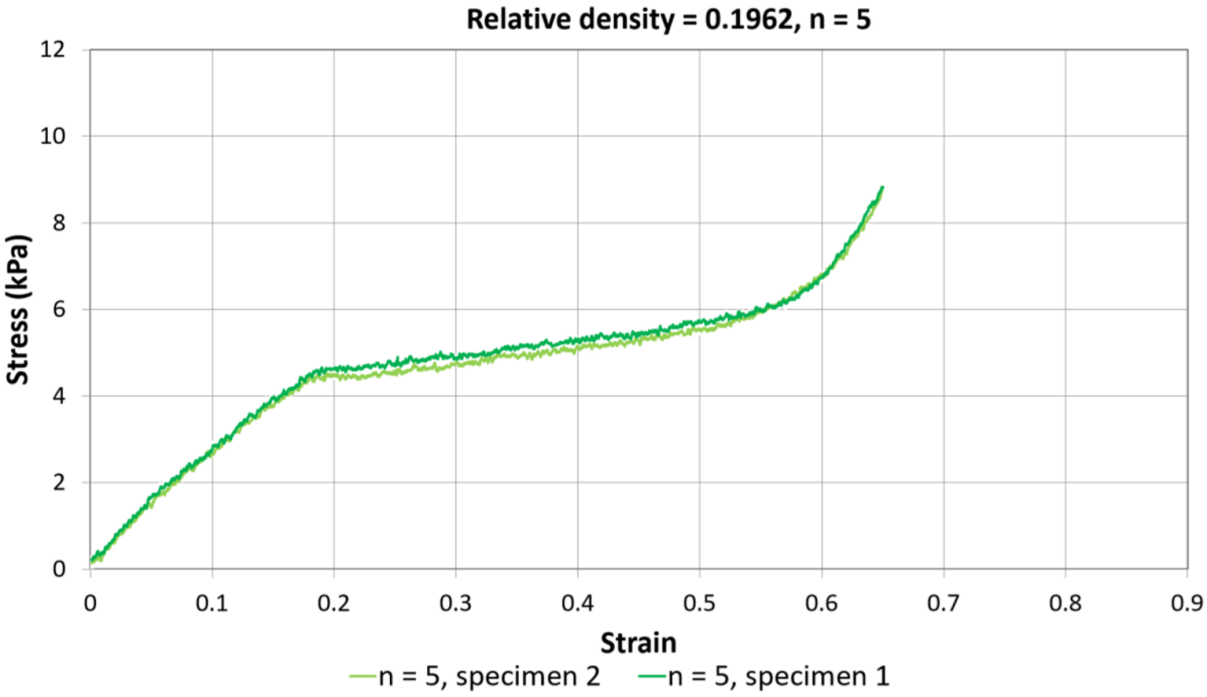
Relative density = 0.1962, n = 5
Stress (kPa)
Strain
n = 5, specimen 2
n = 5, specimen 1

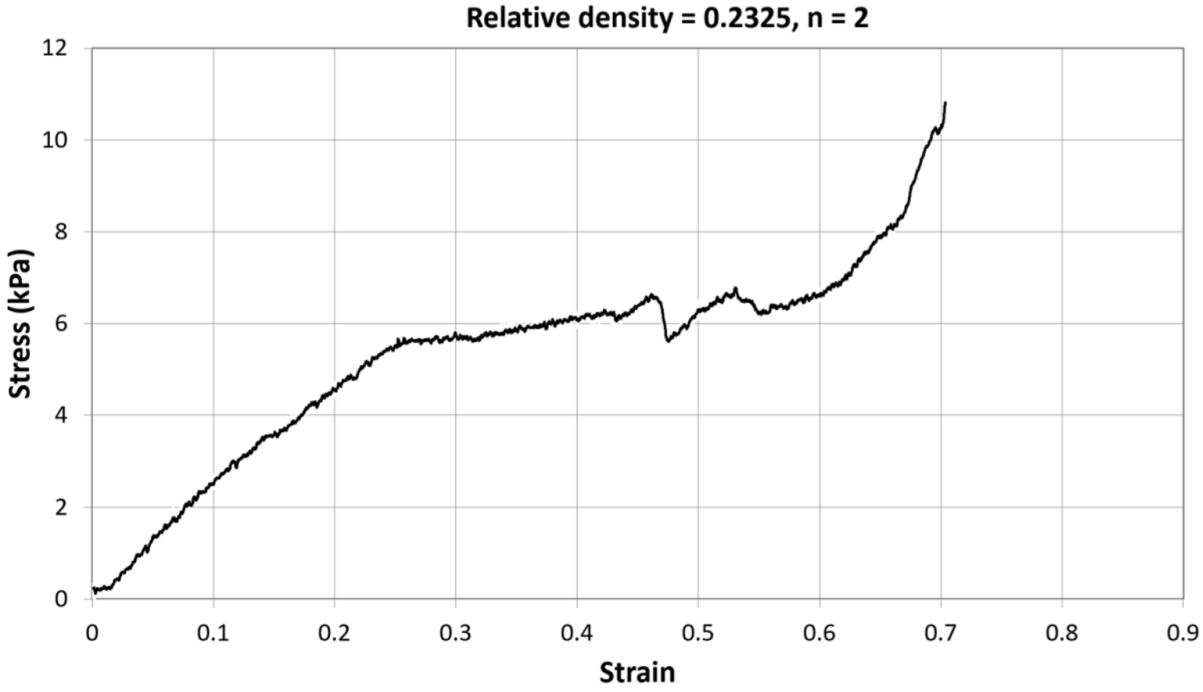
Relative density = 0.2325, n = 2
Stress (kPa)
Strain

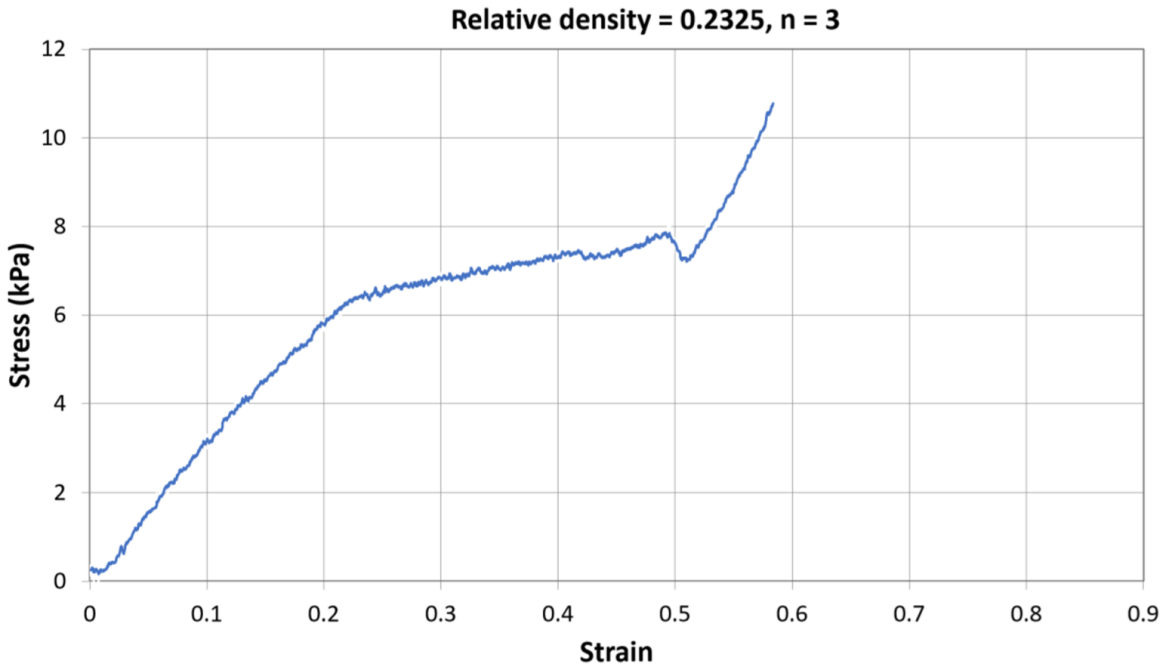
Relative density = 0.2325, n = 3
Stress (kPa)
Strain
0
2
4
6
8
10
12
0
0.1
0.2
0.3
0.4
0.5
0.6
0.7
0.8
0.9

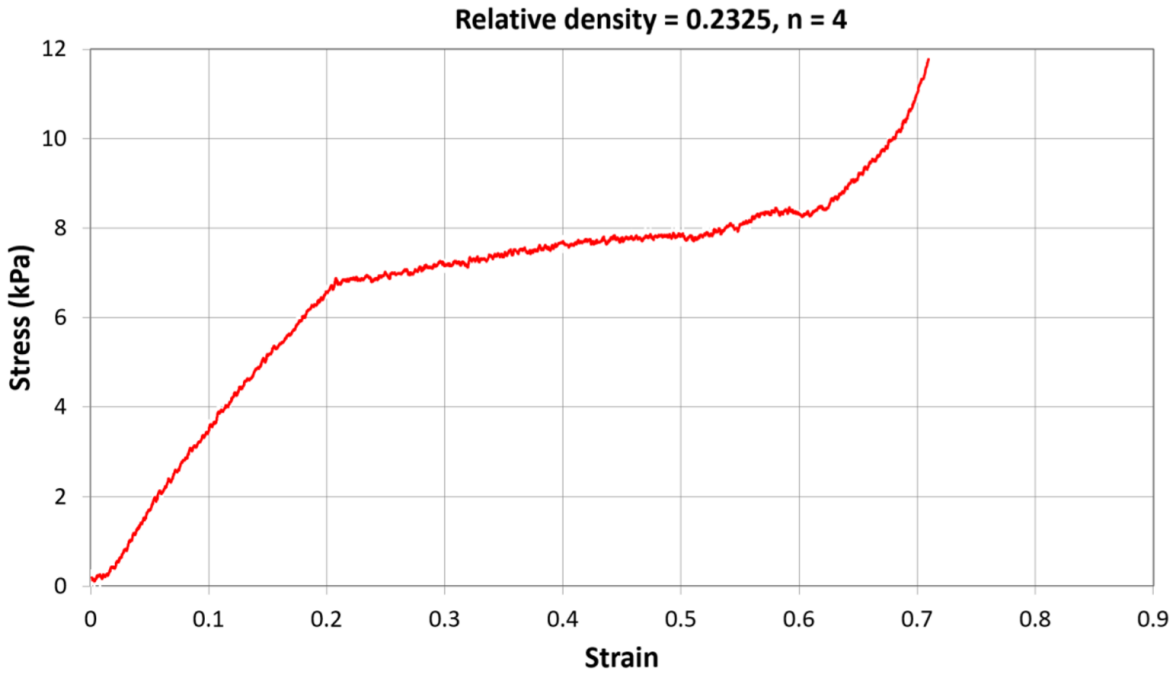
Relative density = 0.2325, n = 4
Stress (kPa)
Strain
0
2
4
6
8
10
12
0
0.1
0.2
0.3
0.4
0.5
0.6
0.7
0.8
0.9

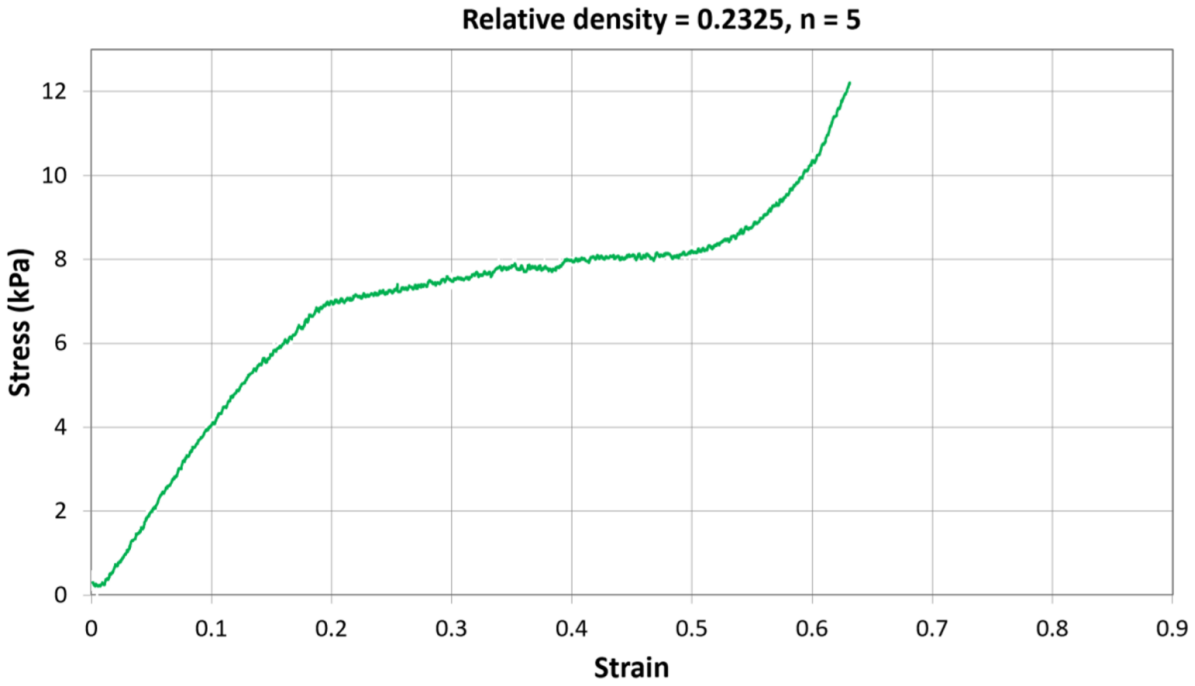
Relative density = 0.2325, n = 5
Stress (kPa)
Strain
0
2
4
6
8
10
12
0
0.1
0.2
0.3
0.4
0.5
0.6
0.7
0.8
0.9

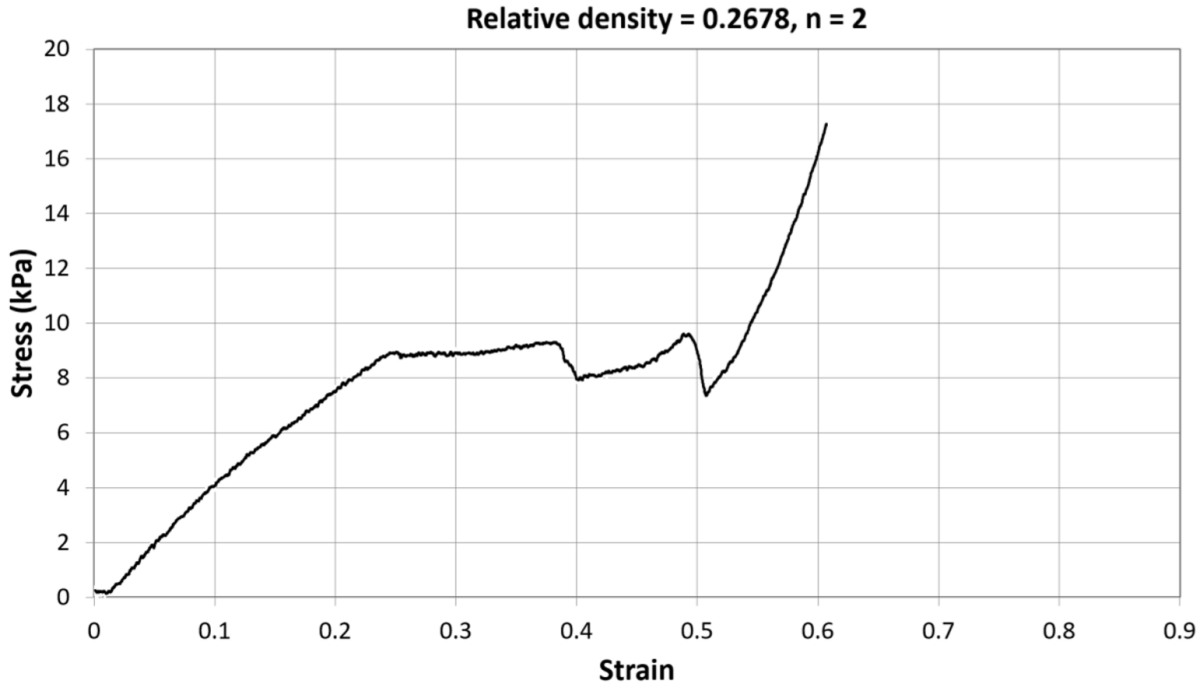
Relative density = 0.2678, n = 2
Stress (kPa)
Strain
0
2
4
6
8
10
12
14
16
18
20
0
0.1
0.2
0.3
0.4
0.5
0.6
0.7
0.8
0.9

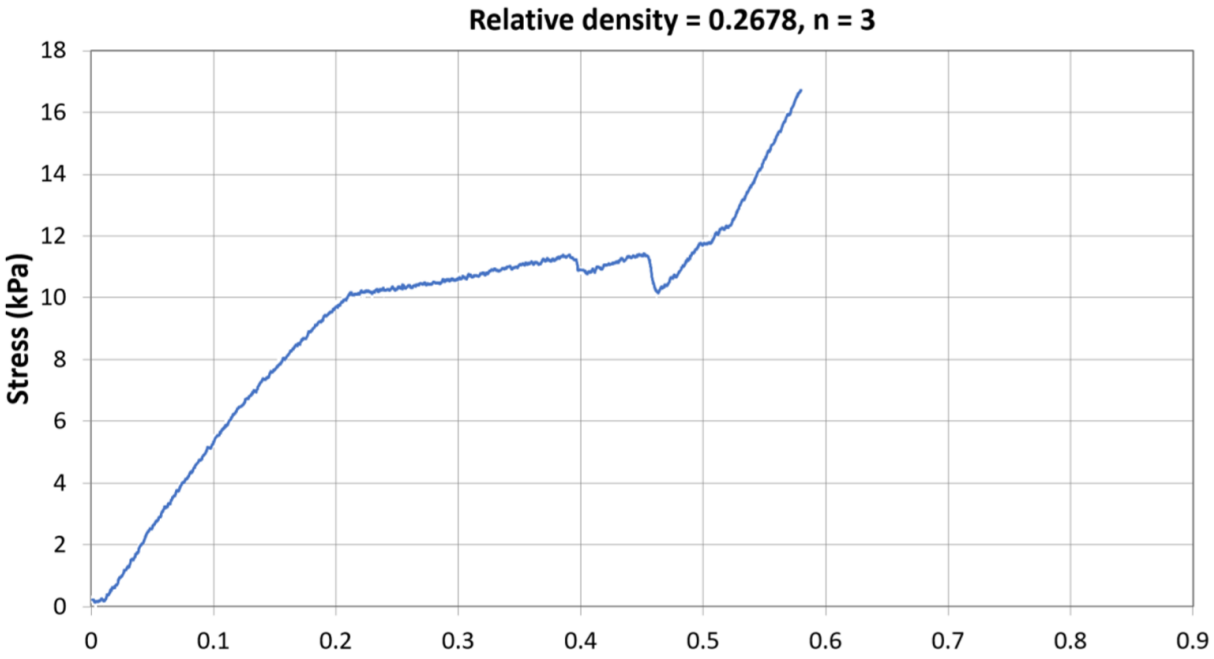
Relative density = 0.2678, n = 3
Stress (kPa)
0
2
4
6
8
10
12
14
16
18
0
0.1
0.2
0.3
0.4
0.5
0.6
0.7
0.8
0.9

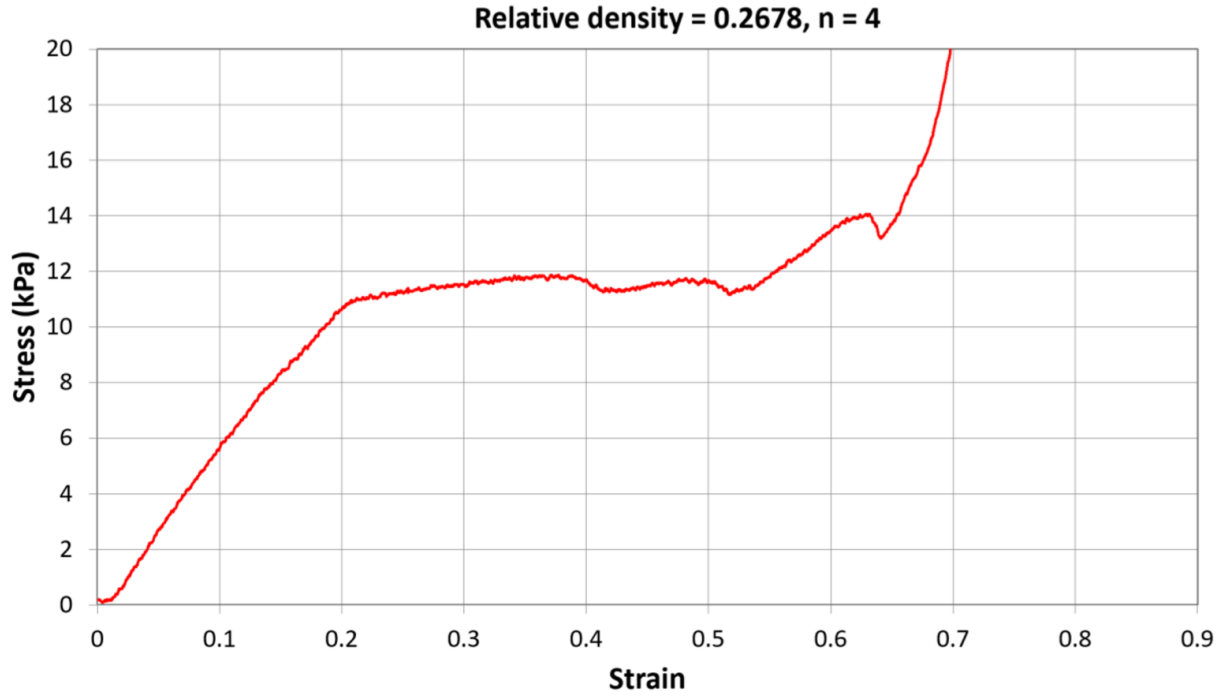
Relative density = 0.2678, n = 4
Stress (kPa)
0
2
4
6
8
10
12
14
16
18
20
0
0.1
0.2
0.3
0.4
0.5
0.6
0.7
0.8
0.9
Strain

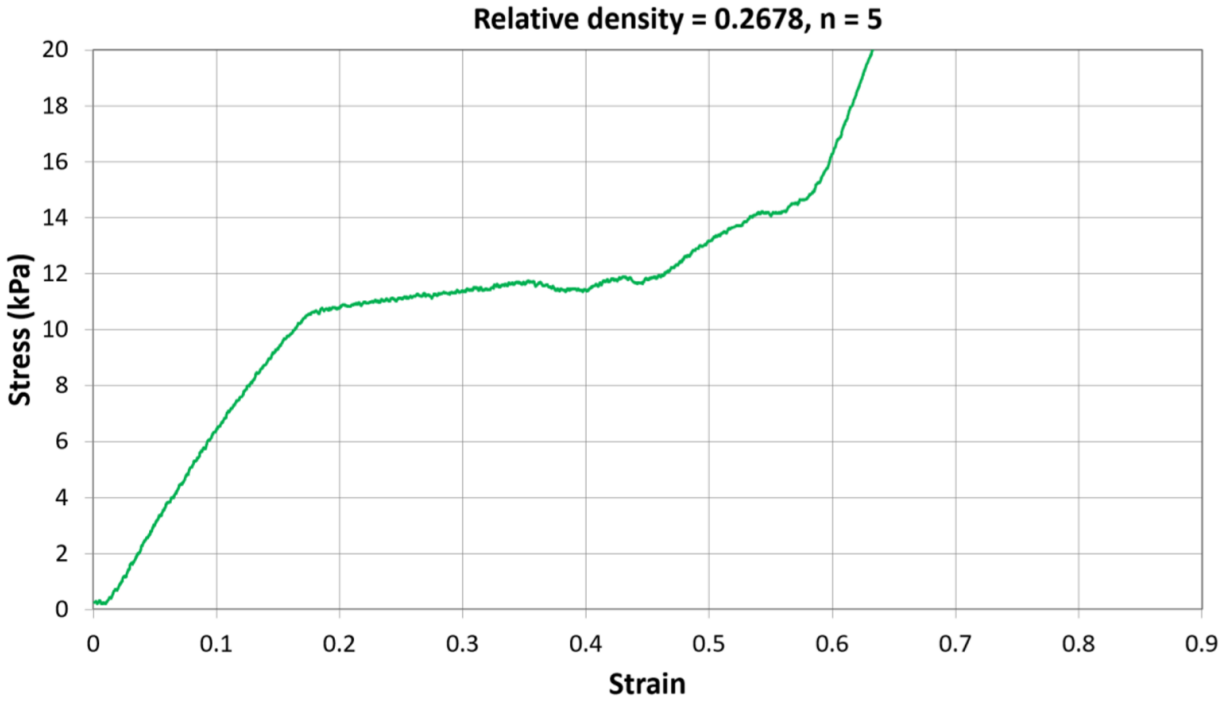
Relative density = 0.2678, n = 5
Stress (kPa)
Strain
0
2
4
6
8
10
12
14
16
18
20
0
0.1
0.2
0.3
0.4
0.5
0.6
0.7
0.8
0.9

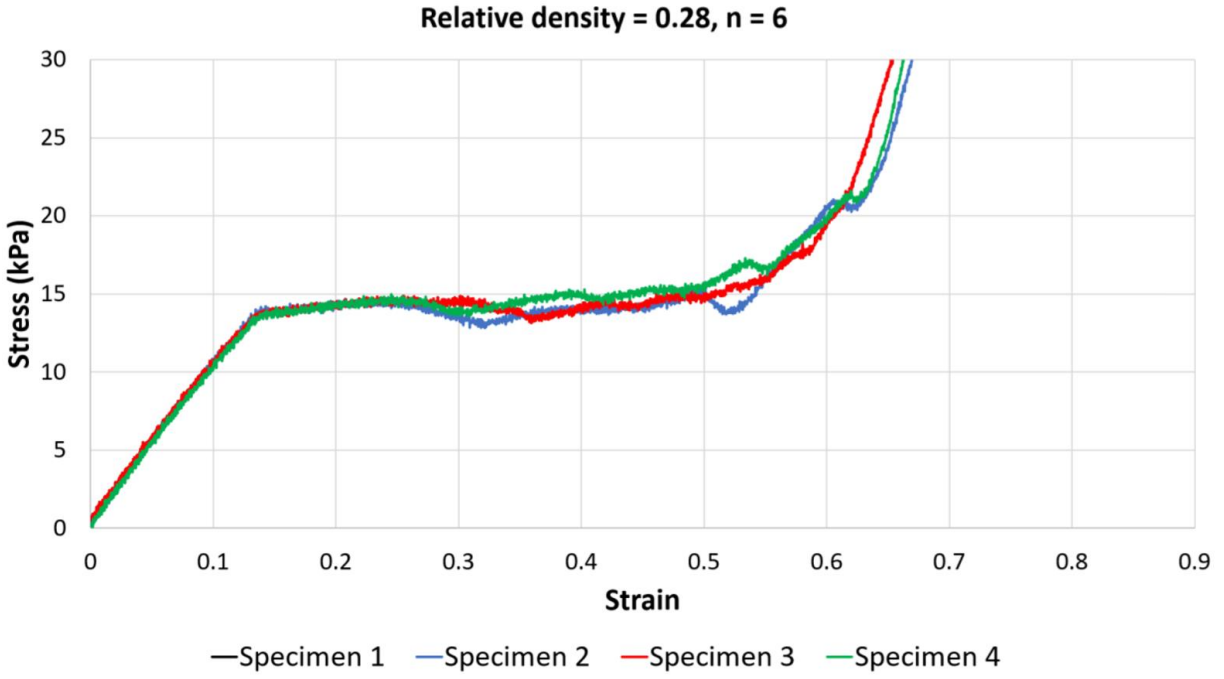
Relative density = 0.28, n = 6
Stress (kPa)
Strain
0
5
10
15
20
25
30
0
0.1
0.2
0.3
0.4
0.5
0.6
0.7
0.8
0.9
Specimen 1
Specimen 2
Specimen 3
Specimen 4

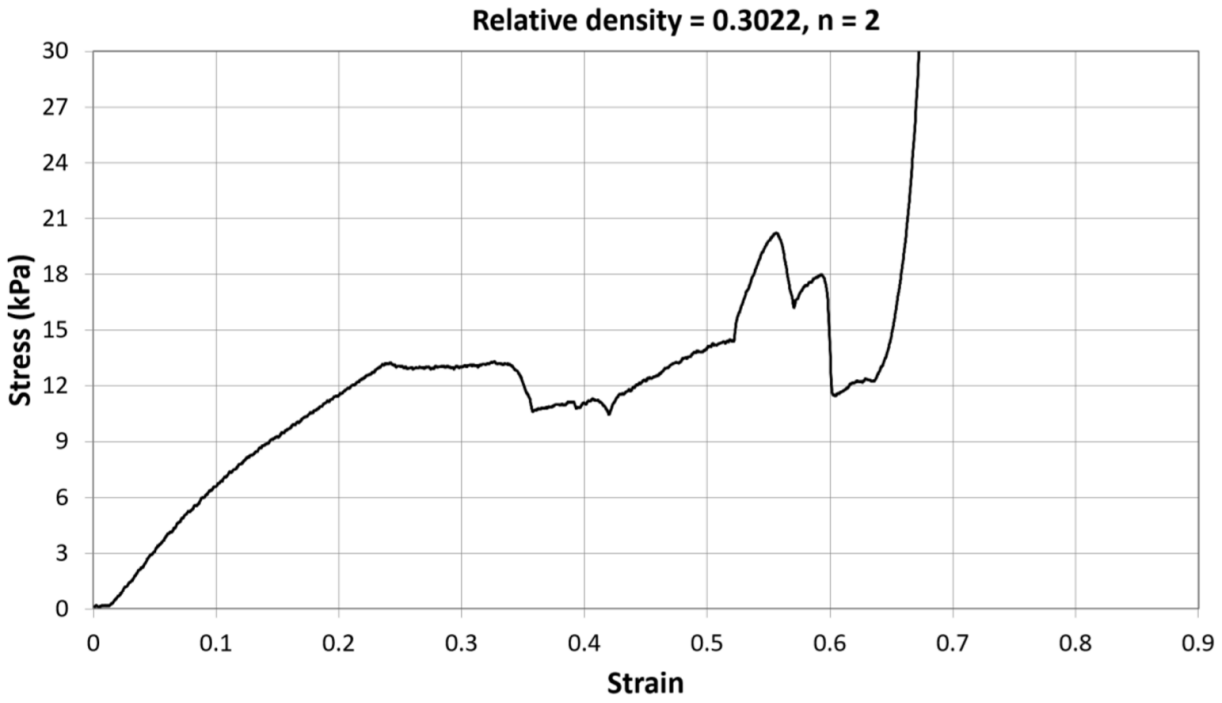
Relative density = 0.3022, n = 2
Stress (kPa)
Strain
0
3
6
9
12
15
18
21
24
27
30
0
0.1
0.2
0.3
0.4
0.5
0.6
0.7
0.8
0.9

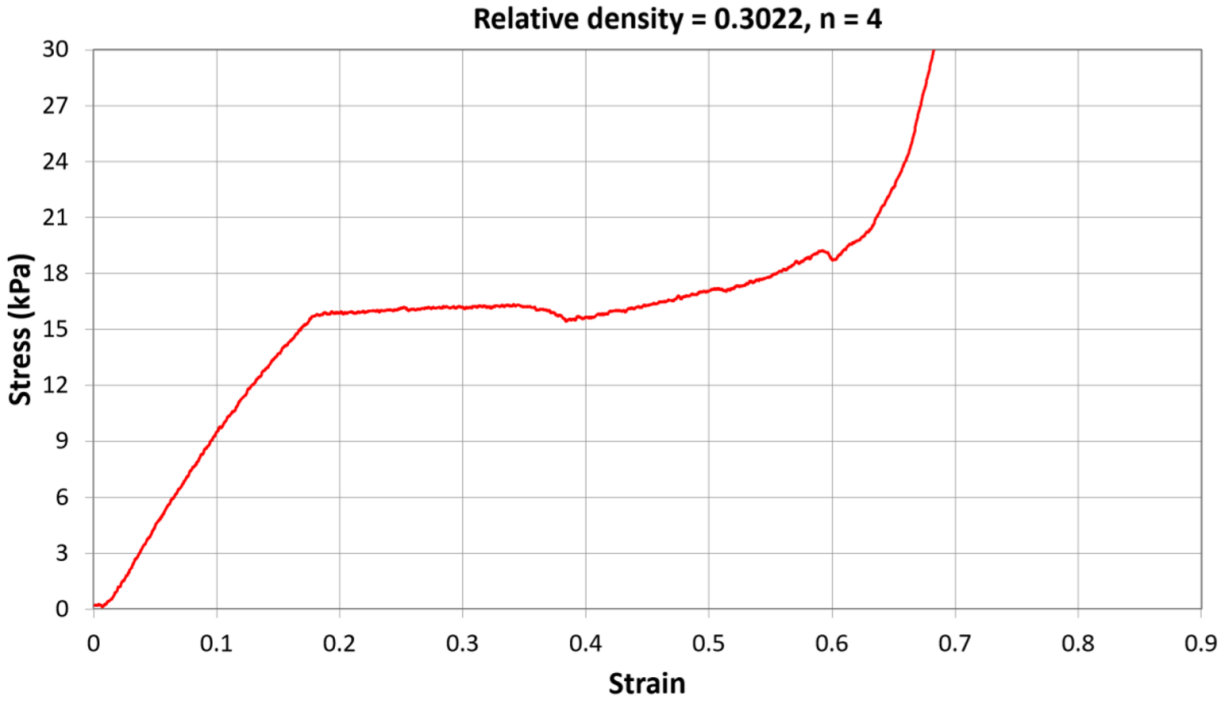
Relative density = 0.3022, n = 4
Stress (kPa)
Strain
0
3
6
9
12
15
18
21
24
27
30
0
0.1
0.2
0.3
0.4
0.5
0.6
0.7
0.8
0.9

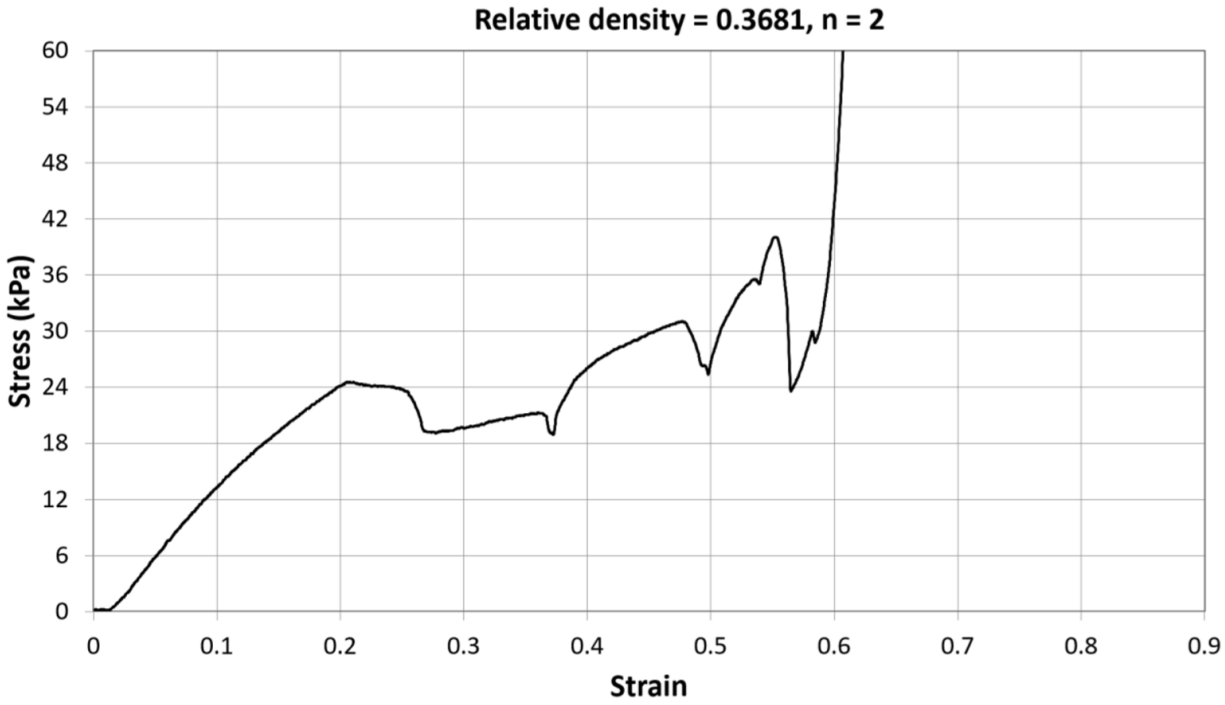
Relative density = 0.3681, n = 2
Stress (kPa)
60
54
48
42
36
30
24
18
12
6
0
0
0.1
0.2
0.3
0.4
0.5
0.6
0.7
0.8
0.9
Strain

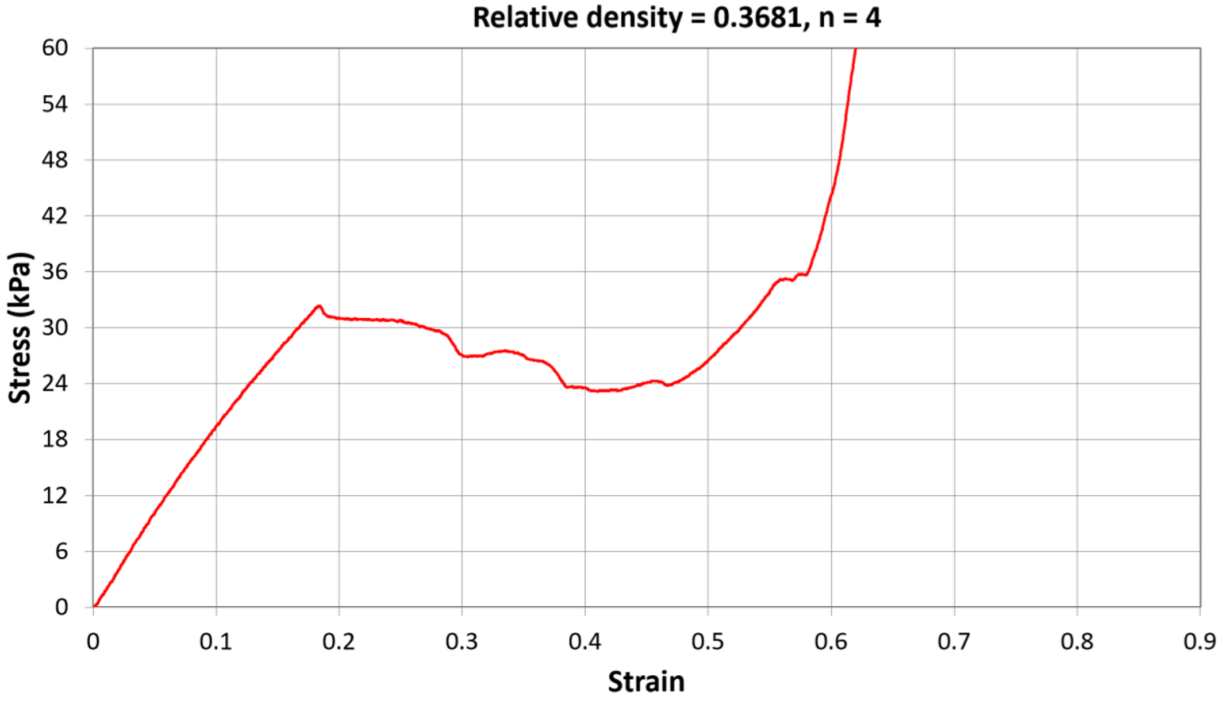
Relative density = 0.3681, n = 4
Stress (kPa)
60
54
48
42
36
30
24
18
12
6
0
0
0.1
0.2
0.3
0.4
0.5
0.6
0.7
0.8
0.9
Strain

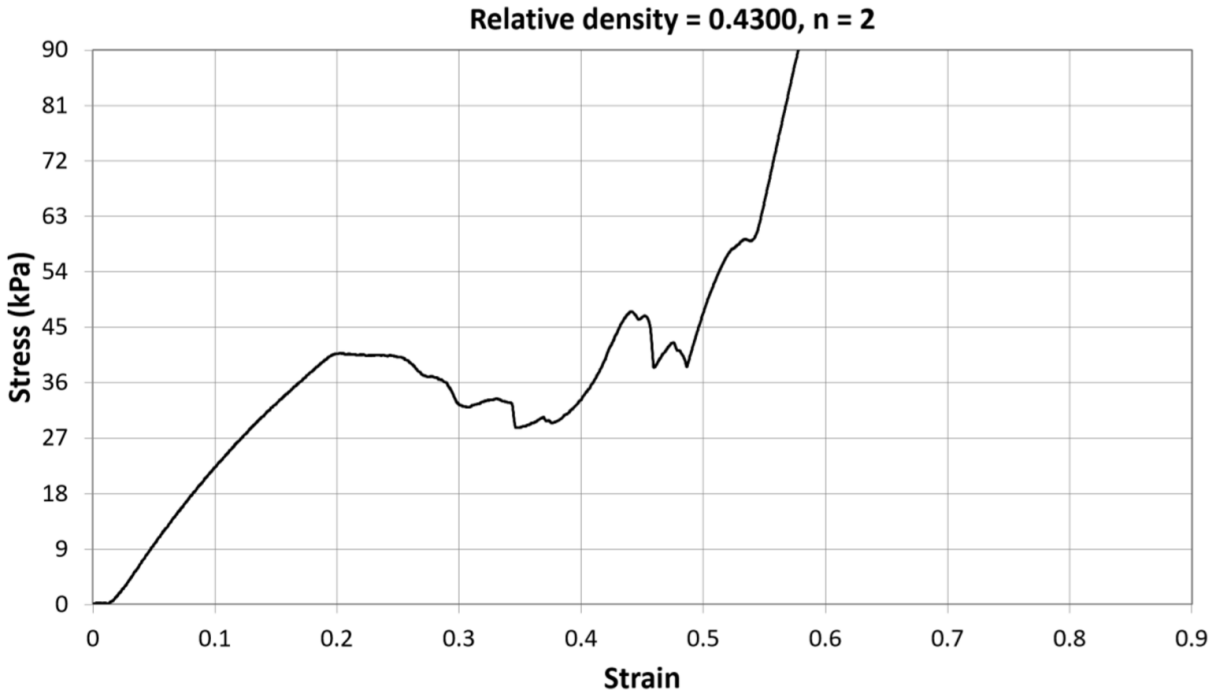
Relative density = 0.4300, n = 2
Stress (kPa)
90
81
72
63
54
45
36
27
18
9
0
0
0.1
0.2
0.3
0.4
0.5
0.6
0.7
0.8
0.9
Strain

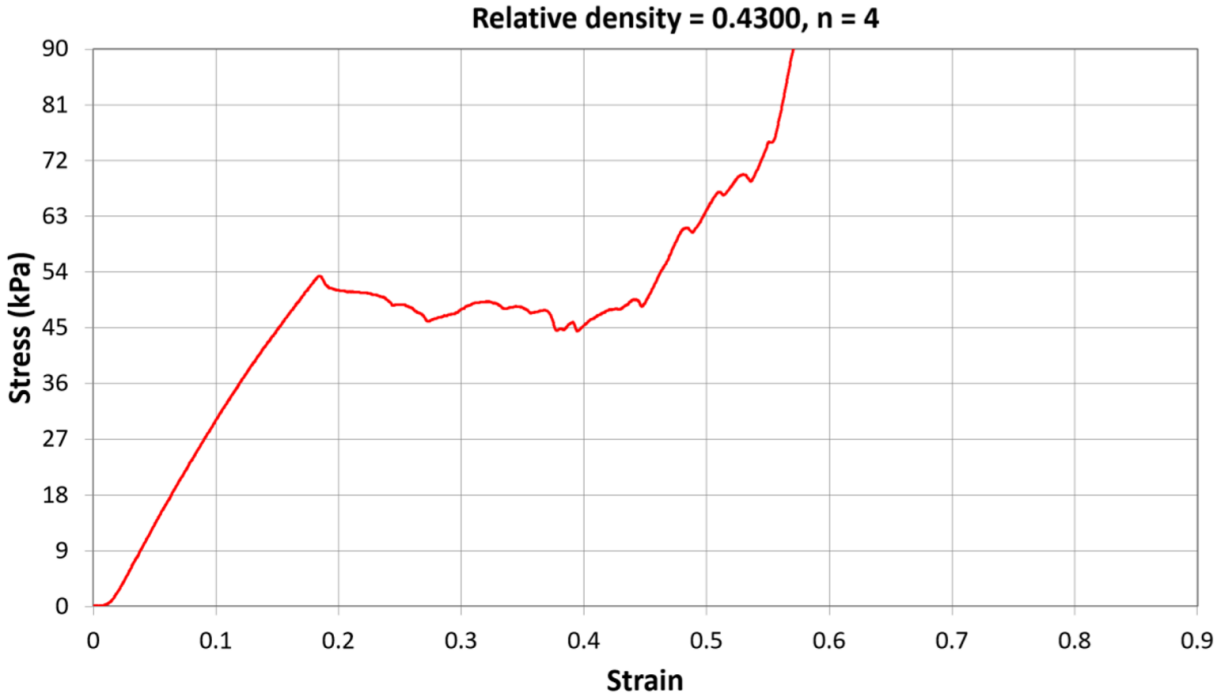
Relative density = 0.4300, n = 4
Stress (kPa)
90
81
72
63
54
45
36
27
18
9
0
0
0.1
0.2
0.3
0.4
0.5
0.6
0.7
0.8
0.9
Strain

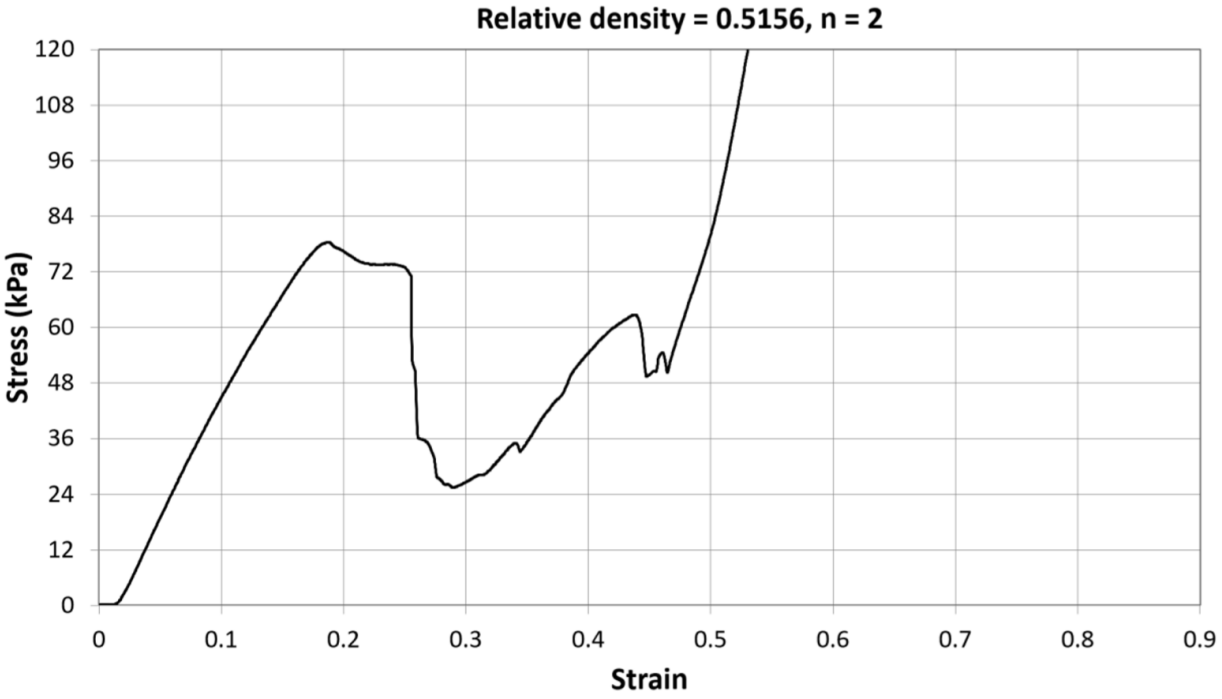
Relative density = 0.5156, n = 2
Stress (kPa)
120
108
96
84
72
60
48
36
24
12
0
0
0.1
0.2
0.3
0.4
0.5
0.6
0.7
0.8
0.9
Strain

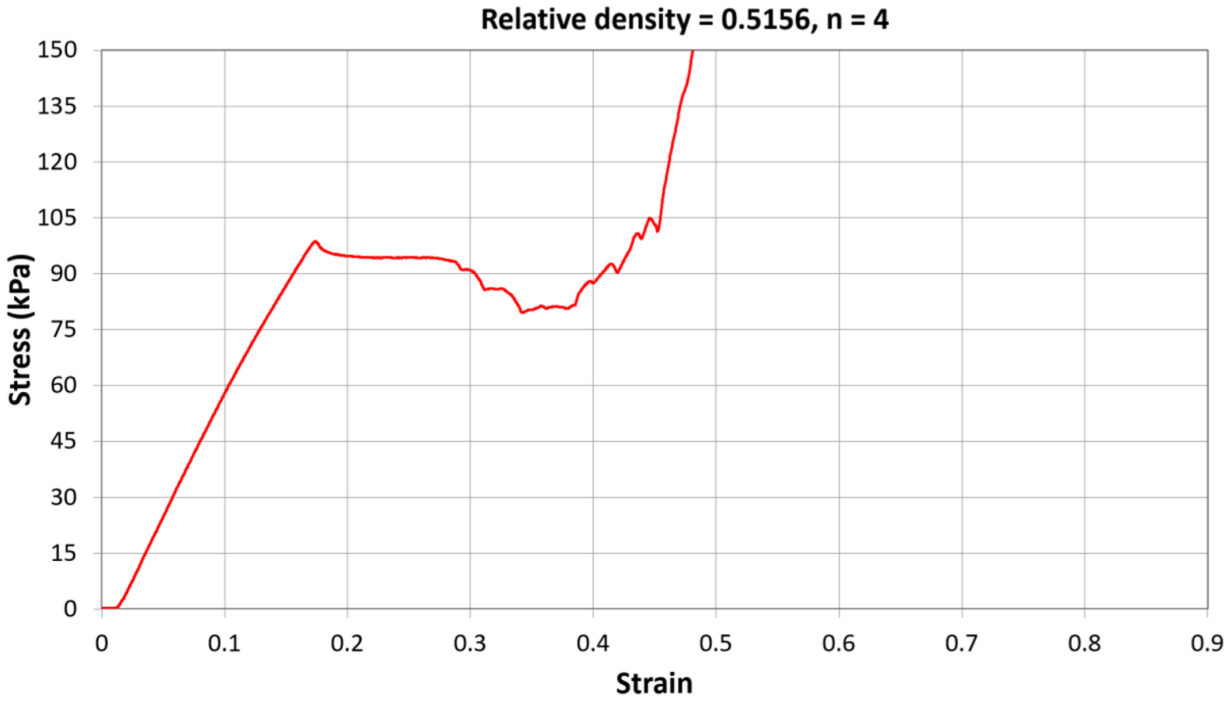
Relative density = 0.5156, n = 4
Stress (kPa)
150
135
120
105
90
75
60
45
30
15
0
0
0.1
0.2
0.3
0.4
0.5
0.6
0.7
0.8
0.9
Strain

Static compression test results (Polyethylene 1.7 pcf, 2-inch thickness, 50 mm by 50 mm)

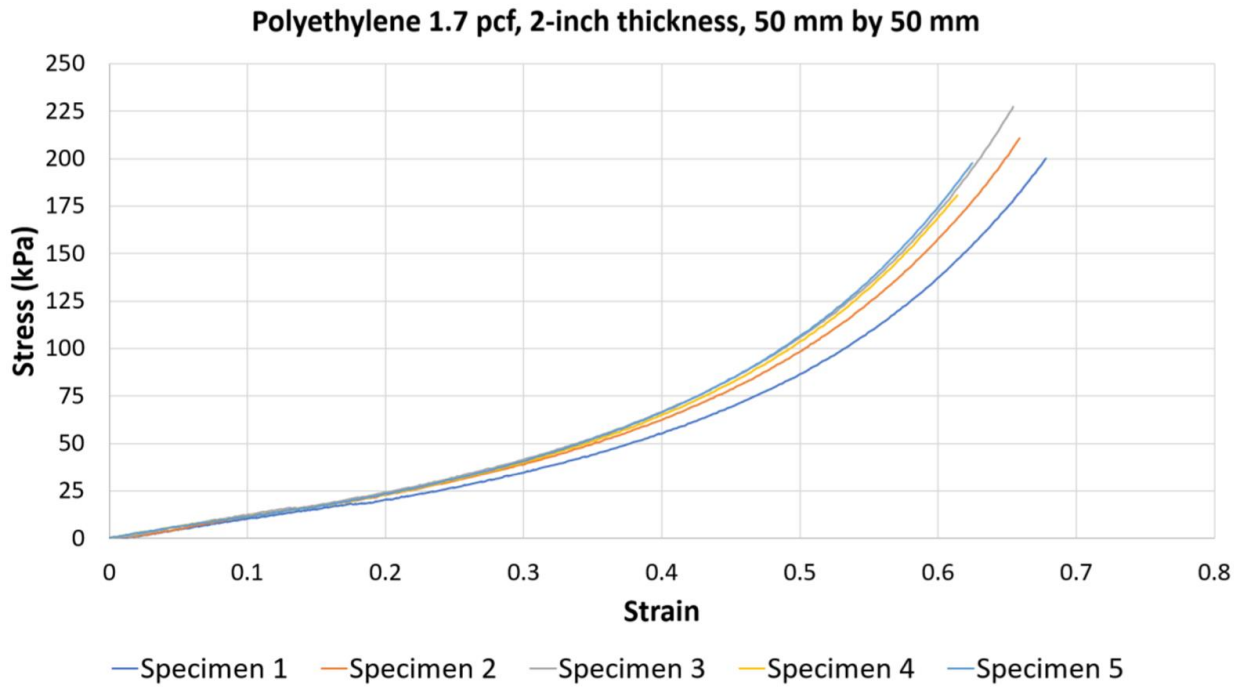

Curve fitting of 3D printed hexagonal array's compressive stress-strain curves with predictive model (Section 4.4)

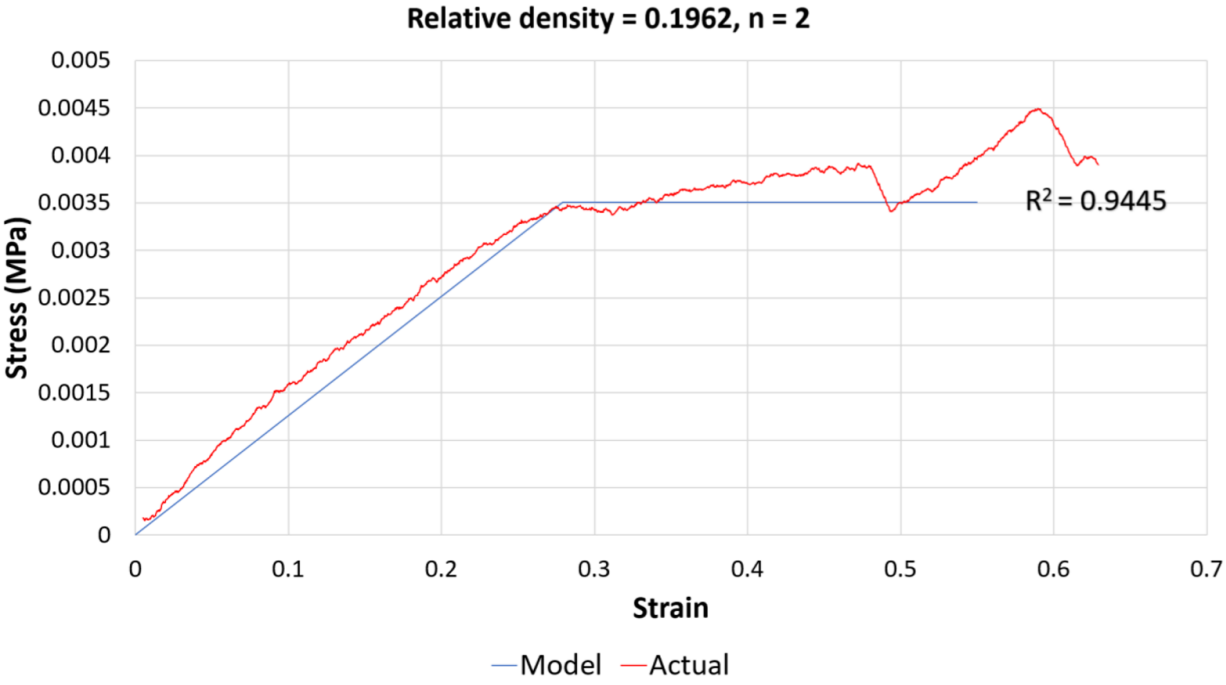

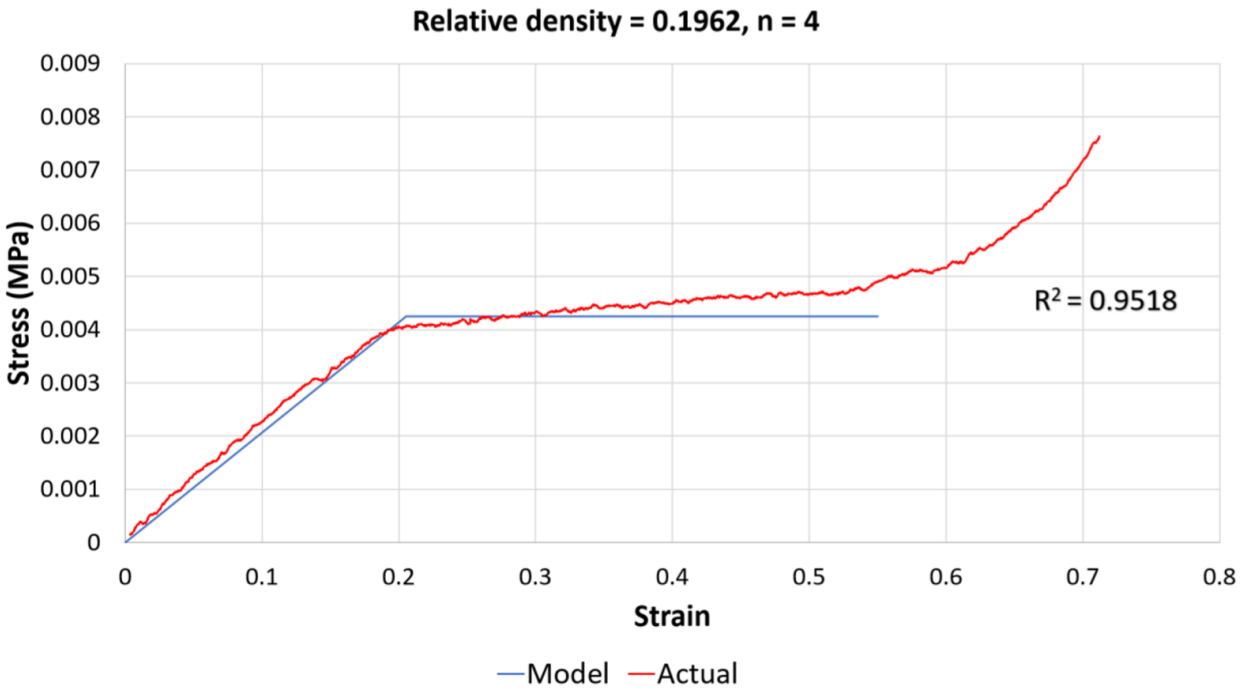
Relative density = 0.1962, n = 4
Stress (MPa)
0.009
0.008
0.007
0.006
0.005
0.004
0.003
0.002
0.001
0
0
0.1
0.2
0.3
0.4
0.5
0.6
0.7
0.8
Strain
R² = 0.9518
Model
Actual

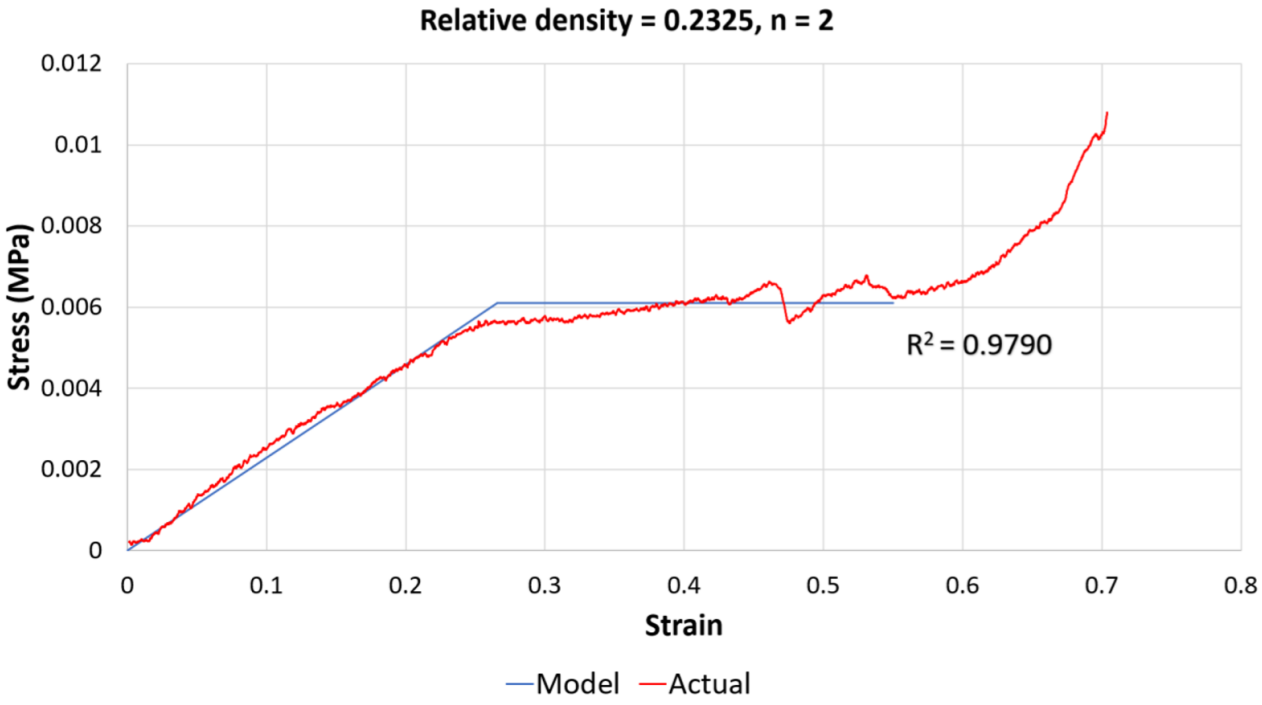
Relative density = 0.2325, n = 2
Stress (MPa)
0.012
0.01
0.008
0.006
0.004
0.002
0
0
0.1
0.2
0.3
0.4
0.5
0.6
0.7
0.8
Strain
R² = 0.9790
Model
Actual

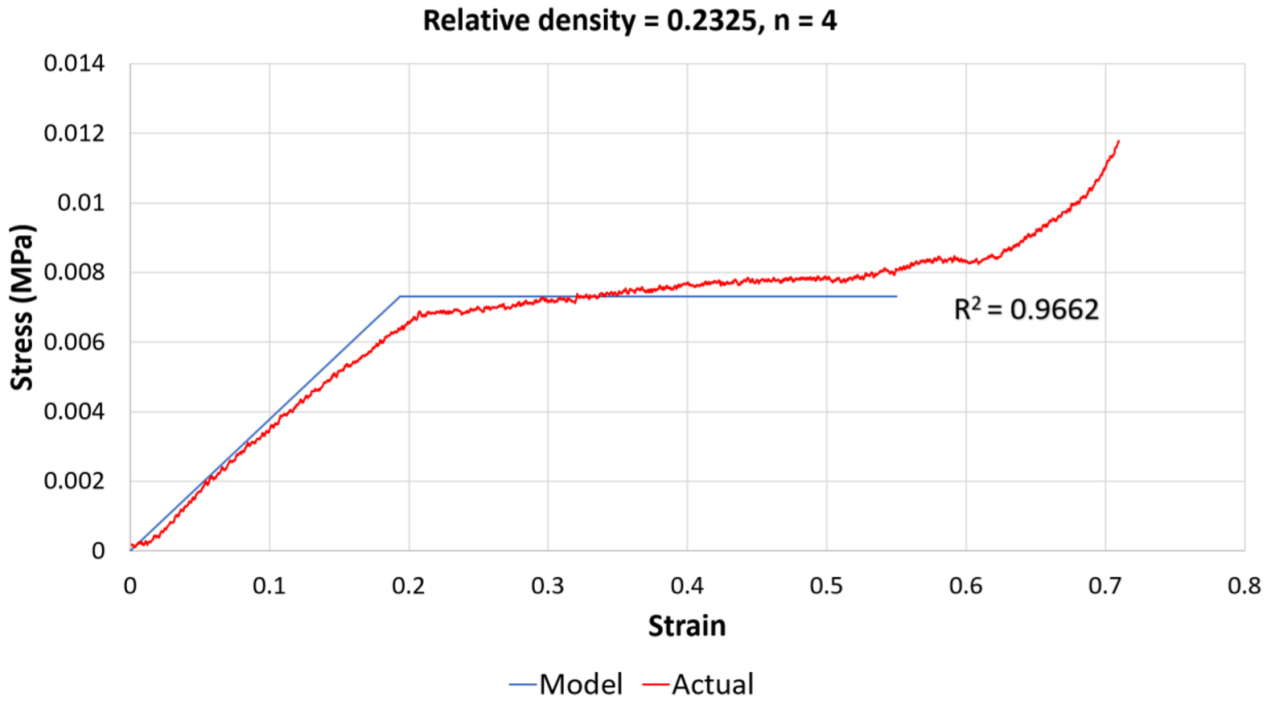
Relative density = 0.2325, n = 4
Stress (MPa)
0.014
0.012
0.01
0.008
0.006
0.004
0.002
0
0
0.1
0.2
0.3
0.4
0.5
0.6
0.7
0.8
Strain
R² = 0.9662
Model
Actual

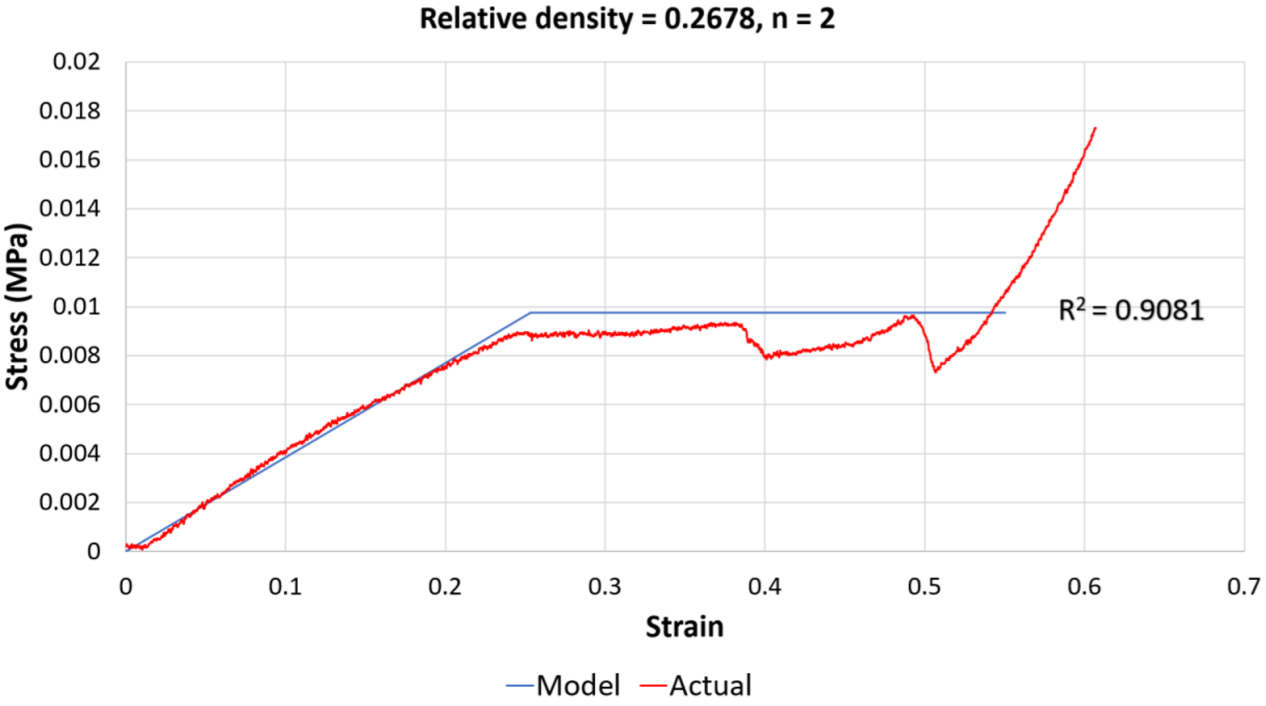
Relative density = 0.2678, n = 2
Stress (MPa)
0.02
0.018
0.016
0.014
0.012
0.01
0.008
0.006
0.004
0.002
0
0
0.1
0.2
0.3
0.4
0.5
0.6
0.7
Strain
R² = 0.9081
Model
Actual

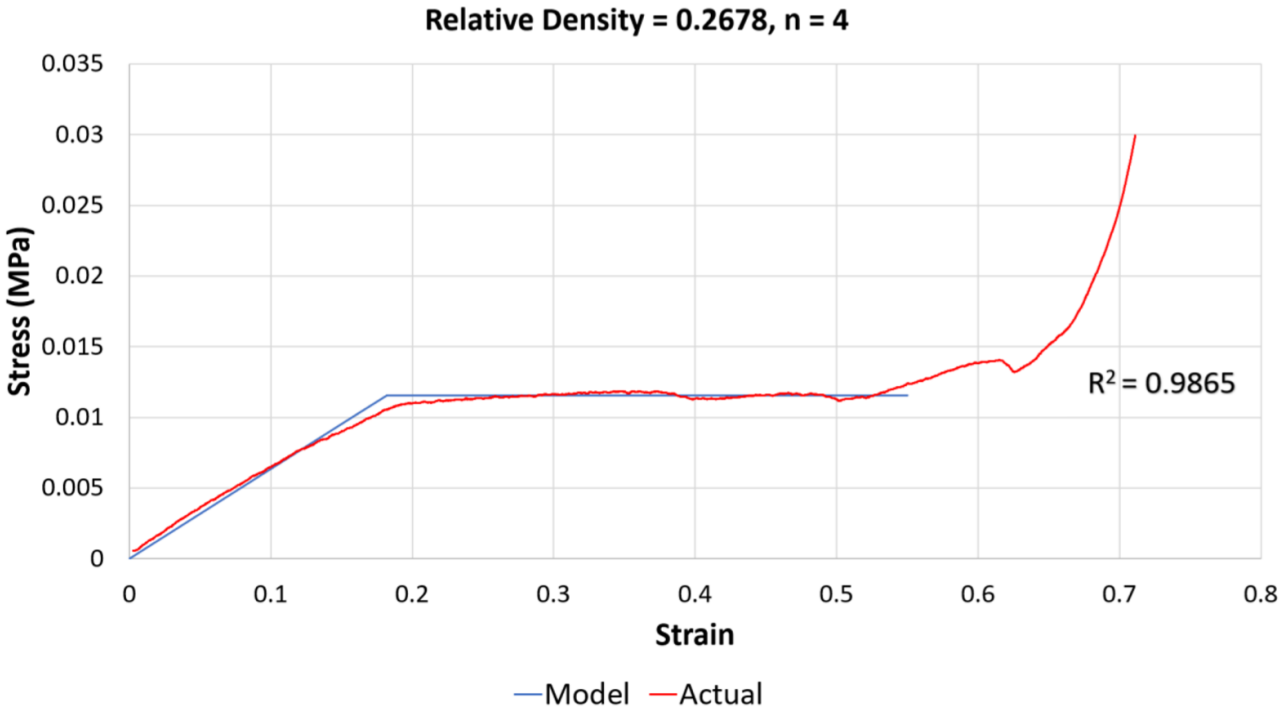
Relative Density = 0.2678, n = 4
Stress (MPa)
0.035
0.03
0.025
0.02
0.015
0.01
0.005
0
0
0.1
0.2
0.3
0.4
0.5
0.6
0.7
0.8
Strain
R² = 0.9865
Model
Actual

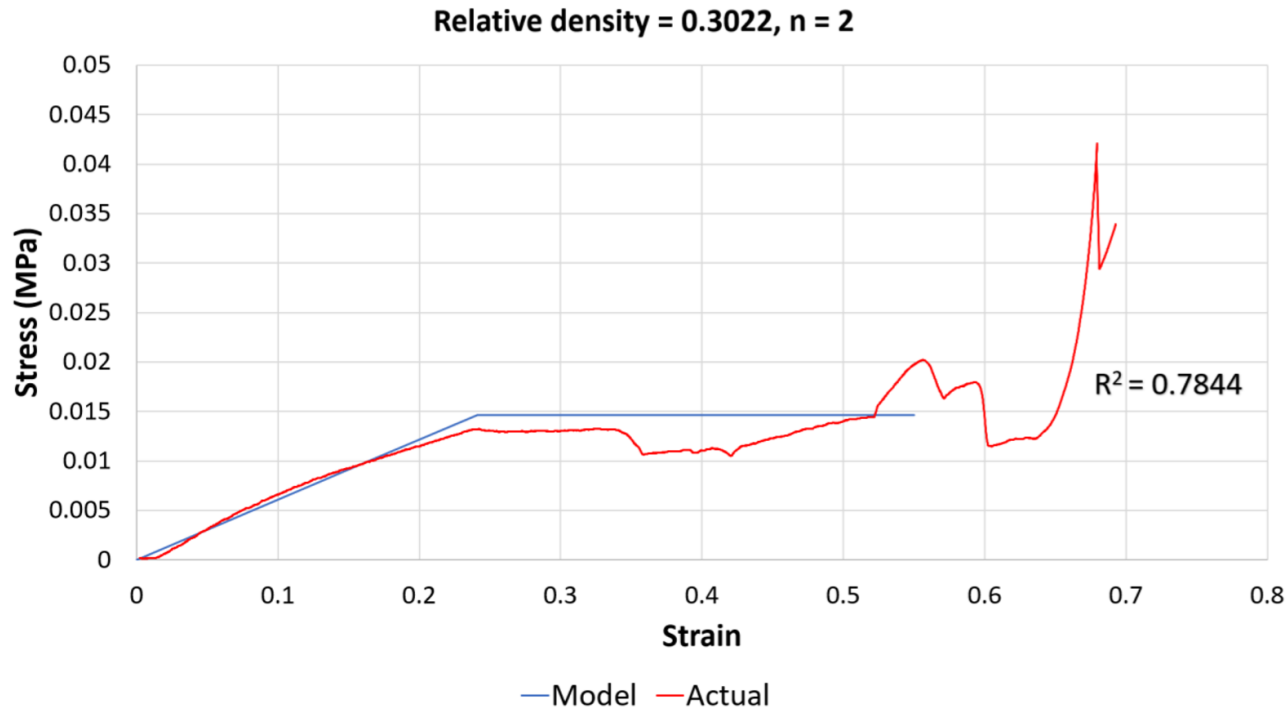
Relative density = 0.3022, n = 2
Stress (MPa)
0.05
0.045
0.04
0.035
0.03
0.025
0.02
0.015
0.01
0.005
0
0
0.1
0.2
0.3
0.4
0.5
0.6
0.7
0.8
Strain
R² = 0.7844
Model
Actual

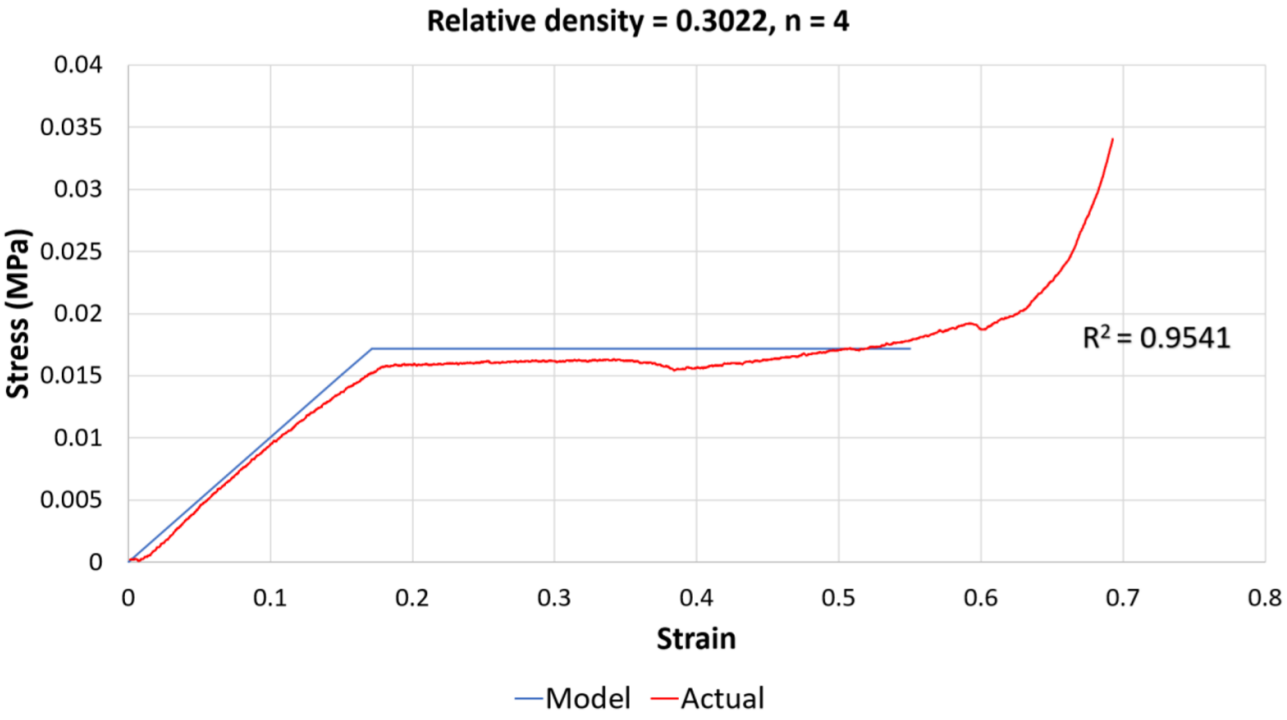
Relative density = 0.3022, n = 4
0.04
0.035
0.03
0.025
0.02
0.015
0.01
0.005
0
Stress (MPa)
0
0.1
0.2
0.3
0.4
0.5
0.6
0.7
0.8
Strain
R² = 0.9541
Model
Actual

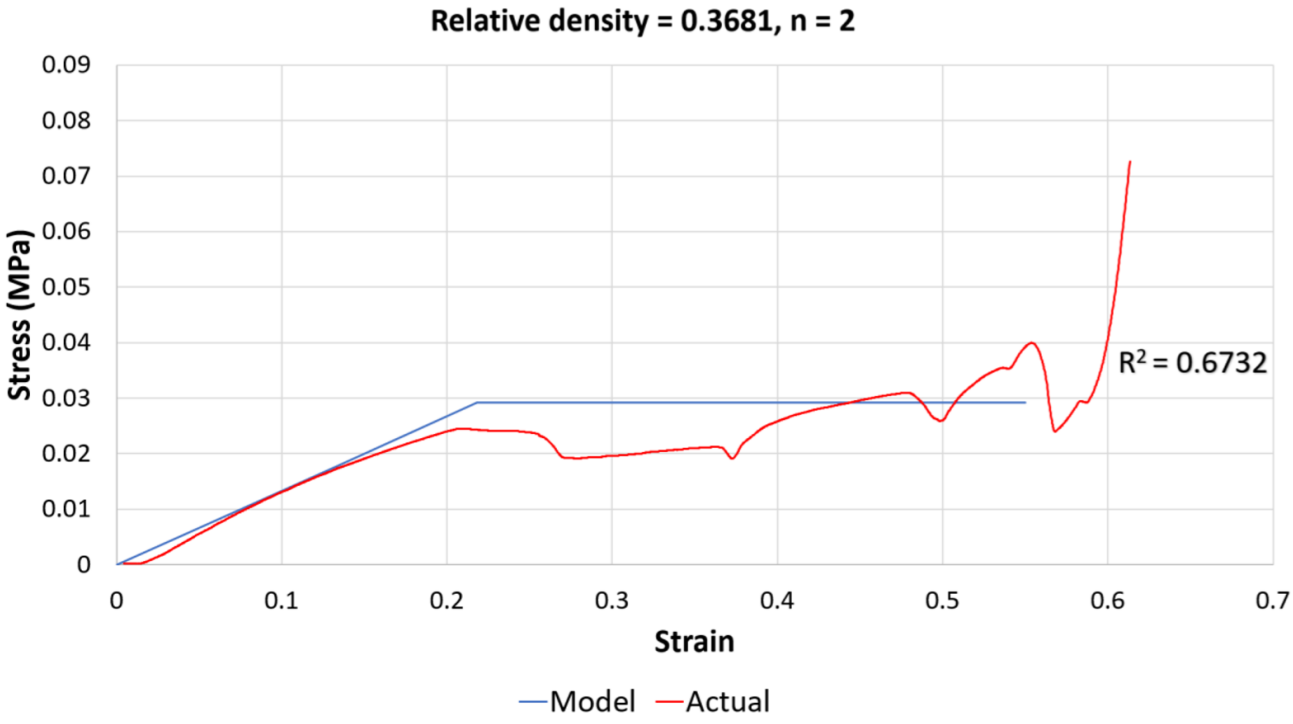
Relative density = 0.3681, n = 2
0.09
0.08
0.07
0.06
0.05
0.04
0.03
0.02
0.01
0
Stress (MPa)
0
0.1
0.2
0.3
0.4
0.5
0.6
0.7
Strain
R² = 0.6732
Model
Actual

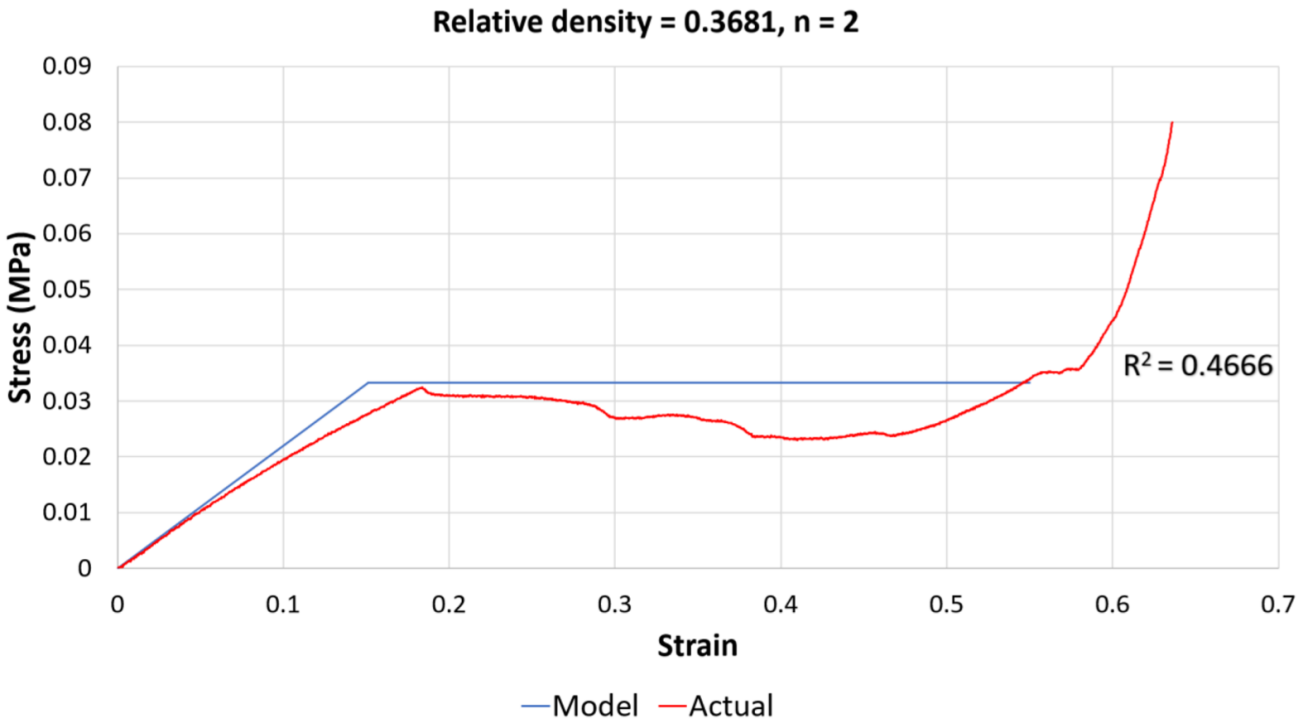
Relative density = 0.3681, n = 2
Stress (MPa)
0.09
0.08
0.07
0.06
0.05
0.04
0.03
0.02
0.01
0
0
0.1
0.2
0.3
0.4
0.5
0.6
0.7
Strain
R² = 0.4666
Model
Actual

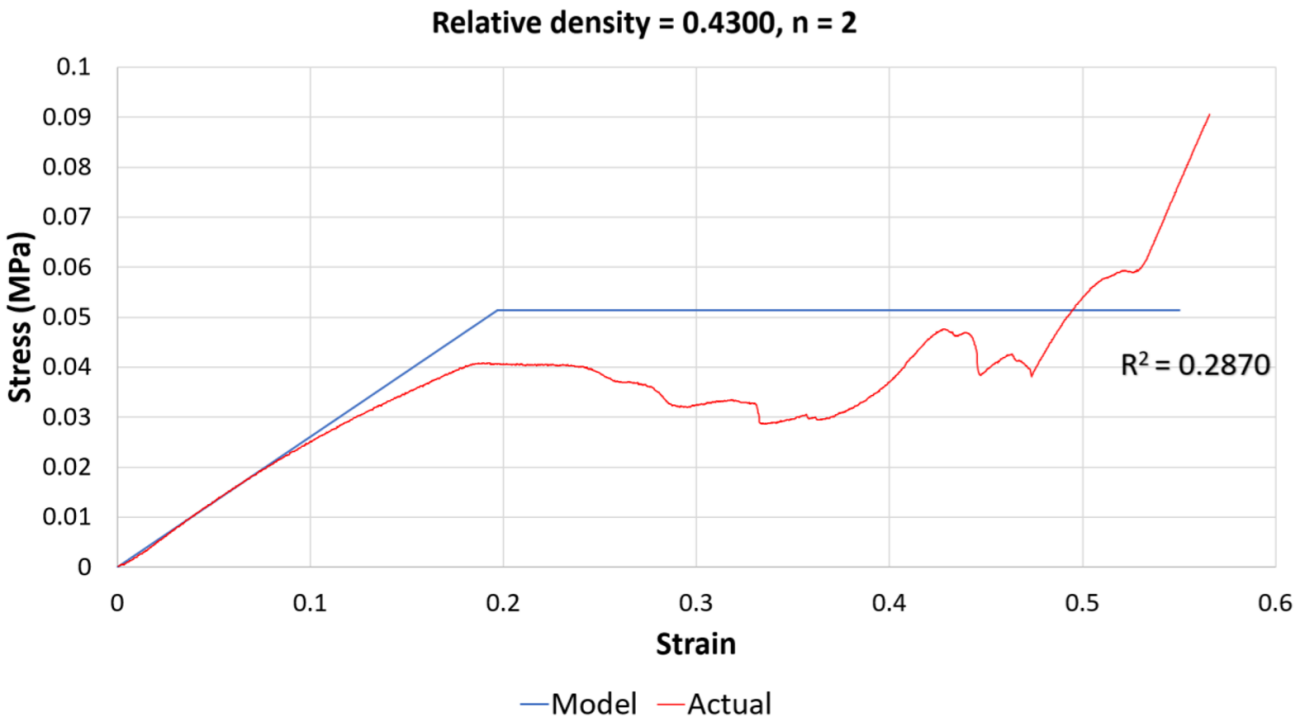
Relative density = 0.4300, n = 2
Stress (MPa)
0.1
0.09
0.08
0.07
0.06
0.05
0.04
0.03
0.02
0.01
0
0
0.1
0.2
0.3
0.4
0.5
0.6
Strain
R² = 0.2870
Model
Actual

Dynamic compression test results

Table C-1: PE foam, 90 mm by 100 mm by 2 inches, 1.7 pcf, 15 cm drop height

Specimen	V_{in} (ms^{-1})	V_{out} (ms^{-1})	timegate (msec)	a (ms^{-2})	G =a/9.8
1	1.6407	1.6326	15.48	211.453	21.58
2	1.6483	1.6467	15.41	213.822	21.82
3	1.7729	1.7685	14.33	247.132	25.22
4	1.6189	1.6178	15.69	206.291	21.05
5	1.7782	1.7774	14.28	248.992	25.41

Table C-2:PE foam, 90 mm by 100 mm by 2 inches, 1.7 pcf, 30 cm drop height

Specimen	V_{in} (ms^{-1})	V_{out} (ms^{-1})	timegate (msec)	a (ms^{-2})	G =a/9.8
1	2.302	2.2988	11.03	417.117	42.56
2	2.3132	2.3078	10.98	420.856	42.94
3	2.3109	2.2568	10.99	415.623	42.41
4	2.2803	2.279	11.14	409.273	41.76
5	2.3704	2.3119	10.72	436.782	44.57

Table C-3: PE foam, 90 mm by 100 mm by 2 inches, 1.7 pcf, 45 cm drop height

Specimen	V_{in} (ms^{-1})	V_{out} (ms^{-1})	timegate (msec)	a (ms^{-2})	G =a/9.8
1	2.2961	2.2907	11.06	414.720	42.32
2	2.2803	2.2755	11.14	408.959	41.73
3	2.3032	2.3023	11.03	417.543	42.61
4	2.2869	2.2861	11.11	411.611	42.00
5	2.2851	2.198	11.12	403.157	41.14

Table C-4: PE foam, 90 mm by 100 mm by 2 inches, 1.7 pcf, 60 cm drop height

Specimen	V_{in} (ms^{-1})	V_{out} (ms^{-1})	timegate (msec)	a (ms^{-2})	G =a/9.8
1	2.882	2.8775	8.81	653.746	66.71
2	2.8808	2.8781	8.82	652.937	66.63
3	2.8638	2.8627	8.87	645.603	65.88
4	2.8851	2.8836	8.8	655.534	66.89
5	2.8962	2.8947	8.77	660.308	67.38

Table C-5: Hexagonal array, 100 mm by 75 mm by 57.74 mm, relative density = 0.28, n = 6, 12.6 cm drop height

Specimen	V_{in} (ms^{-1})	V_{out} (ms^{-1})	timegate (msec)	a (ms^{-2})	G =a/9.8
1	1.6757	0	15.16	110.534	11.28
2	1.4819	0	17.14	86.459	8.82
3	1.4649	0	17.34	84.481	8.62
4	1.4689	0	17.29	84.957	8.67
5	1.4817	0	17.14	86.447	8.82